CENTRO DE INVESTIGACIÓN Y DE ESTUDIOS AVANZADOS DEL INSTITUTO POLITÉCNICO NACIONAL

Unidad Saltillo

PROGRAMA DE DOCTORADO EN NANOCIENCIAS Y NANOTECNOLOGÍA

"Electrocatalysis of nanostructured Pt-$NiTiO_3$ and Pt-$CoTiO_3$ supported on Vulcan, rGO and rGO functionalized with organometallic compounds for the ORR"

A dissertation submitted in partial fulfillment of the requirements for de degree of:

Doctor en Ciencias

In:

Nanociencias y Nanotecnología

By:

M. C. Anayantzin Hernández Ramírez

Thesis advisors:

Dr. Francisco Javier Rodríguez Varela

Dra. María Esther Sánchez Castro

Ramos Arizpe, Coahuila. February 2019

CENTRO DE INVESTIGACIÓN Y DE ESTUDIOS AVANZADOS DEL INSTITUTO POLITÉCNICO NACIONAL

Unidad Saltillo

PROGRAMA DE DOCTORADO EN NANOCIENCIAS Y NANOTECNOLOGÍA

“Estudio de la RRO en nanocatalizadores de Pt-$NiTiO_3$ y Pt-$CoTiO_3$ soportados en Vulcan, rGO y rGO funcionalizado con compuestos organometálicos de cromo"

Tesis que presenta:

M. C. Anayantzin Hernández Ramírez

Para obtener el grado de:

Doctor en Ciencias en Nanociencias y Nanotecnología

Directores de tesis:

Dr. Francisco Javier Rodríguez Varela

Dra. María Esther Sánchez Castro

Ramos Arizpe, Coahuila. Febrero 2019

CONTENT

Acknowledgements.

The author thanks the Mexican Council for Science and Technology (CONACyT) for financial support through grant 380306.

Abstract

The Oxygen Reduction Reaction (ORR) was studied in alkaline conditions on the Pt-$NiTiO_3$ and Pt-$CoTiO_3$ catalysts, which were dispersed on different carbon supports: i) Vulcan XC-72 (C), ii) reduced graphene oxide (rGO) and iii) rGO functionalized with two chromium organometallic compounds ($Cr(CO)_6$ and [(η^6-(C_6H_6)$Cr(CO)_3$]).

Chapter VI showed that the mass and specific activities of Pt-$NiTiO_3$/C and Pt-$CoTiO_3$/C are higher at some overpotentials (mass activity at ca. 0.91 and 0.86 V/RHE and below for Pt-$NiTiO_3$/C and Pt-$CoTiO_3$/C, respectively, and specific activity at 0.94 V/RHE and below for both catalysts) than those of Pt/C. Moreover, the tolerance tests at 0.1 M CH_3OH and C_2H_5OH showed an enhanced behavior of Pt-$CoTiO_3$/C, compared to Pt/C and Pt-$NiTiO_3$/C in terms of significantly lower alcohol oxidation current densities.

In Chapter VII, Pt-$CoTiO_3$/rGO was the most active catalyst in terms of specific activity, a 1.5-fold enhancement over Pt/rGO. Furthermore, the tolerance tests indicated that Pt-$CoTiO_3$/rGO exhibits high ORR performance and lower methanol oxidation reaction (MOR) activity compared to Pt/rGO.

Chapter VIII covered one of the first attempts to functionalize rGO with Cr organometallic compounds. Different stoichiometric amounts of $Cr(CO)_6$ gave mono and bis-hexahapto complexes (rGO-Cr_{tric} and rGO_2Cr) as a result of the displacement of the carbonyl groups. In the reaction of rGO with (η^6-C_6H_6)$Cr(CO)_3$, the arene ligand was retained and the three carbonyl groups disappeared, forming the rGO-Cr_{bz} complex. During the evaluation of catalytic activity for the ORR, Pt-$CoTiO_3$/rGO-Cr_{bz} showed superior specific activity (compared to Pt-$CoTiO_3$/rGO-Cr_{tric}, Pt-$CoTiO_3$/rGO_2Cr and Pt-$CoTiO_3$/rGO), indicating that the enhancement in the performance for the ORR is promoted by the organometallic functionalization of rGO. Furthermore, the ORR performance of the catalysts in the presence of methanol and ethanol showed that Pt-$CoTiO_3$/rGO-Cr_{bz} has slightly higher methanol tolerance, suggesting some degree of selectivity towards the ORR.

Resumen

Se estudia la Reacción de Reducción de Oxígeno (RRO) en los catalizadores de Pt-$NiTiO_3$ y Pt-$CoTiO_3$ en condiciones alcalinas. Los catalizadores fueron dispersados en diferentes soportes de carbón: i) Vulcan XC-72 (C), ii) óxido de grafeno reducido (rGO) y iii) rGO funcionalizado con dos compuestos organometálicos de cromo ($Cr(CO)_6$ y [(η^6-C_6H_6)$Cr(CO)_3$]).

El Capítulo VI muestra que en términos de actividad másica y específica los catalizadores que contienen metaltitanatos (Pt-$NiTiO_3$/C y Pt-$CoTiO_3$/C) presentan mayor actividad catalítica (a algunos sobrepotenciales) en comparación con la de Pt/C. Las pruebas de tolerancia (RRO en presencia de CH_3OH y C_2H_5OH 0.1 M) mostraron que el uso de $CoTiO_3$ como co-catalizador incrementa notablemente la tolerancia y la selectividad del Pt, ya que las densidades de corriente de oxidación de ambos alcoholes son significativamente más bajas, en comparación con Pt/C y Pt-$NiTiO_3$/C.

Los resultados del Capítulo VII mostraron que el catalizador Pt-$CoTiO_3$/rGO posee una actividad específica 1.5 veces superior a la de Pt/rGO y una menor actividad para la reacción de oxidación de metanol (ROM).

El Capítulo VIII presenta los resultados de la funcionalización de rGO con compuestos organometalicos. Se encontró que la variación de las cantidades estequiométricas de $Cr(CO)_6$ resultan en la formación de compuestos mono o bis-hexahapto coordinados (rGO-Cr_{tric} y rGO_2Cr) y en la reacción del rGO con (η^6-C_6H_6)$Cr(CO)_3$ el ligante areno se retiene y los grupos carbonilo son desplazados formando el complejo rGO-Cr_{bz}. Se llevó a cabo la evaluación de la actividad catalítica de Pt-$CoTiO_3$/rGO-Cr_{tric}, Pt-$CoTiO_3$/rGO_2Cr y Pt-$CoTiO_3$/rGO-Cr_{bz}. El catalizador Pt-$CoTiO_3$/rGO-Cr_{bz} mostró mayor actividad específica (en comparación con Pt-$CoTiO_3$/rGO-Cr_{tric}, Pt-$CoTiO_3$/rGO_2Cr y Pt-$CoTiO_3$/rGO), la cual es promovida por la funcionalización organometálica del rGO. Además, las pruebas de tolerancia mostraron que este catalizador posee mayor tolerancia y selectividad hacia la RRO en presencia de metanol.

Abbreviations

a	Lattice parameter (nm)
ADAFCs	Alkaline Direct Alcohol Fuel Cells
AEMFCs	Alkaline Exchange Membrane Fuel Cells
A_{Pt}	Pt real surface area (cm^2)
at. %	Atomic percentage
a.u.	Arbitrary units
b	Tafel slope ($mV\ dec^{-1}$)
BE	Binding Energy (eV)
C	Carbon black (Vulcan XC-72)
Cr-bz	Benzene chromium tricarbonyl, $[(\eta^6\text{-}C_6H_6)Cr(CO)_3]$
Cr-hexa	Chromium hexacarbonyl, $Cr(CO)_6$
CV	Cyclic Voltammetry
D	Crystallite size (nm)
d	Interplanar distance (nm)
E	Potential (V)
$E°_a$	Standard Anodic Potential (V)
$E°_c$	Standard Cathodic Potential (V)
$E°_{cell}$	Cell Standard Potential (V)
ECSA	Electrochemical Surface Area ($m^2\ g^{-1}$)
E_{onset}	Onset potential (mV)
EOR	Ethanol Oxidation Reaction
FFT	Fourier Fast Transform
FTIR	Fourier Transform Infrared Spectroscopy
GO	Graphene Oxide
H_{des}	Hydrogen Desorption Region
hop	High overpotentials ($mV\ dec^{-1}$)
HOR	Hydrogen Oxidation Reaction
HR-TEM	High Resolution Transmission Electron Microscopy
iFFT	Inverse Fourier Fast Transform

IHP	Inner Helmholtz plane
i_m	Mass activity (A mg^{-1}_{Pt})
i_s	Specific activity (μA cm^{-2}_{Pt})
j	Current density (mA cm^{-2})
JCPDS	Joint Committee on Powder Diffraction Standards
j_d	Diffusion-limited current density (mA cm^{-2})
j_k	Kinetic current density (mA cm^{-2})
lop	Low overpotentials (mV dec^{-1})
L_{Pt}	Pt loading (g)
$MTiO_3$	Metaltitanates ($NiTiO_3$, $CoTiO_3$)
MOR	Methanol Oxidation Reaction
n	Transferred electron number
OHP	Outer Helmholtz plane
ORR	Oxygen reduction reaction
PEMFCs	Proton Exchange Membrane Fuel Cells
Pt/C	Platinum catalyst supported on Vulcan XC-72
Pt-$CoTiO_3$/C	Platinum-Cobalt titanate catalyst supported on Vulcan XC-72
Pt-$NiTiO_3$/C	Platinum-Nickel titanate catalyst supported on Vulcan XC-72
Pt/rGO	Platinum catalyst supported on Reduced Graphene Oxide
Pt-$CoTiO_3$/rGO	Platinum-Cobalt titanate catalyst supported on Reduced Graphene Oxide
Pt-$NiTiO_3$/rGO	Platinum-Nickel titanate catalyst supported on Reduced Graphene Oxide
Pt-$CoTiO_3$/rGO$_2$Cr	Platinum-Cobalt titanate catalyst supported on RGO_2Cr
Pt-$CoTiO_3$/rGO-Cr_{tric}	Platinum-Cobalt titanate catalyst supported on RGO-Cr_{tric}

Pt-$CoTiO_3$/rGO-Cr_{bz}	Platinum-Cobalt titanate catalyst supported on RGO-Cr_{bz}
Q_H	Coulombic charge in the H_{des} region (μC)
Q_{ref}	Theoretical charge needed for the oxidation of a monolayer of hydrogen on smooth Pt (μC cm^{-2})
RDE	Rotating Disk Electrode
RHE	Reversible Hydrogen Electrode
rGO	Reduced Graphene Oxide
rGO$_2$Cr	RGO functionalized with 0.04 mmol of Cr-hexa
rGO-Cr_{tric}	RGO functionalized with 0.22 mmol of Cr-hexa
rGO-Cr_{bz}	RGO functionalized with Cr-bz
rpm	Revolutions per minute
SAED	Selected Area Electron Diffraction
SEM/EDS	Scanning Electron Microscopy/Energy Dispersive X-Ray Spectroscopy
SHE	Standard Hydrogen Electrode
TEM	Transmission Electron Microscopy
wt.%	Weight percentage
XPS	X-Ray Photelectron Spectroscopy
XRD	X-Ray Diffraction

Chapter I

Introduction

Nowadays, the vast majority (90%) of energy use for human activities is obtained from the chemical energy stored in fossil fuels. However, the combustion of fossil fuels pollutes the air causing global warming, ozone layer depletion, biosphere and geosphere destruction and ecological devastation. Around 80% of CO_2 emissions worldwide are originated from the energy sector. Consequently, producing energy from fossil fuels has been considered a harmful industry both in terms of air pollution and environmental impact.[1-3] Thus, for a sustainable future, novel clean energy technologies are required to avoid climate change and to reduce the dependency of fossil fuels as the predominant primary energy source.[4,5]

On this context, fuel cell technologies appear advantageous from both energy and environmental points of view. Fuel cells are electrochemical devices which convert the chemical energy of a fuel into electrical energy through electrochemical reactions.[6,7] Proton Exchange Membrane and Anion Exchange Membrane Fuel Cells (PEMFCs and AEMFCs, respectively) are the most intensively studied. However, it has been acknowledged that gaseous hydrogen has several restrictions, including its storage. For this reason, liquid hydrogen-rich alcohol fuels with higher energy density than hydrogen, such as methanol and ethanol, have become an attractive alternative for its use in fuel cells.[8,9]

On this context, Alkaline Direct Alcohol Fuel Cells (ADAFCs), which employ an anion-exchange membrane have emerged as one of the prospective power

sources. ADAFCs offer several advantages, including the increased performance as a result of fast electrochemical kinetics (at both anode and cathode) compared to those in acidic conditions.[10]

On the other hand, nano-sized Pt catalysts are the most active materials for catalyzing both the oxidation of fuel at the anode and the oxygen reduction reaction (ORR) at the cathode.[11,12] The ORR is the major challenge in fuel cells mainly due to its sluggish kinetics[13,14] and for the improvement of the reaction it has been proposed the use of different catalysts configurations, such as Pt-Metal alloys and Pt-Metal oxides composites.[15]

Additionally, it should be mentioned that the support also plays an important role in the performance of the catalyst. Supports with high specific area, such as reduced graphene oxide (rGO), have demonstrated to have an important contribution to increase the catalytic activity of Pt catalysts for the ORR. This is mainly due to the high electric conductivity of rGO and the reactive surface provided by the oxygenated-functional groups, which anchor metal nanoparticles serving as reaction points for the electrocatalysis.[16] Recently, the organometallic functionalization of the rGO has emerged as a new type of covalent modification. This novel approach is interesting since the surface modification does not introduce significant perturbations of the structural integrity of the sp^2-hybridized carbon atoms.[17]

On this context, this PhD thesis focuses on the development of carbon supported Pt-metaltitanates ($MTiO_3$, M = Ni, Co) catalysts which are evaluated as cathodes for the ORR in alkaline media. In a first part, Vulcan XC-72 (C) has been selected as the support of the Pt-$NiTiO_3$ and Pt-$CoTiO_3$ catalysts because of its wide application in low temperature fuel cells, so our findings can be easily extended to other support systems. The microwave-assisted

polyol method was used to synthesize the catalysts in order to obtain nanoparticles with a homogeneous dispersion in a shorter time compared to that of the conventional polyol technique. In the second part, the Pt-$NiTiO_3$ and Pt-$CoTiO_3$ catalysts were supported on rGO. It is of particular interest the use of the rGO as an effective strategy to achieve enhanced the electrocatalytic activity for the ORR.

The last chapter is devoted to the organometallic functionalization of the rGO with two chromium organometallic compounds: $Cr(CO)_6$ and [η^6-$(C_6H_6)Cr(CO)_3$]. The surface modification is expected to result in hexahapto (η^6) complexation of the rGO with the chromium atoms. Subsequently, the functionalized rGO materials were used as support of Pt-$CoTiO_3$. The goal is to use this novel approach of carbon functionalization for the improvement of the ORR catalytic activity of the Pt-$CoTiO_3$ catalyst in alkaline media.

References.

[1] J. B. Goodenough. Electrochemical energy storage in a sustainable modern society. Energy & Environmental Science. 7 (2014) 14.

[2] D. Hart. Sustainable energy conversion: fuel cells – the competitive option?. Journal of Power Sources. 86 (2000) 23.

[3] E. Serrano, G. Rus, J. García-Martínez. Nanotechnology for sustainable energy. Renewable and Sustainable Energy Reviews. 13 (2009) 2373.

[4] D. Stolten. Hydrogen and Fuel Cells. Fundamentals, technologies and applications. Wiley ICH. Germany, 2010.

[5] R. M. Dell, and D. A. J. Rand. Energy storage – a key technology for global energy sustainability. Journal of Power Sources. 100 (2001) 2.

[6] U. Lucia. Overview on fuel cells. Renewable and Sustainable Energy Reviews. 30 (2014) 164.

[7] E. H. Yu, and K. Scott. Development of direct methanol alkaline fuel cells using anion exchange membranes. Journal of Power Sources. 137 (2004) 248

[8] T. S. Zhao, Y. S. Li, and S. Y. Shen. Anion-exchange membrane direct ethanol fuel cells: Status and perspective. Frontiers of Energy and Power Engineering in China. 4 (2010) 443.

[9] E. Antolini, and E. R. González. Alkaline direct alcohol fuel cells. Journal of Power Sources. 195 (2010) 3441.

[10] Q. Li. Nanomaterials for Sustainable Energy. Springer. Switzerland, 2016.

[11] J .L. Gavartin, M. Sarwar, D. C. Papageorgopoulos, D. Gunn, S. García, A. Perlov, A. Krystala, D. L. Ormsby, D. Thompsett, G. G. Wood, A. Andersen, and S. French. Exploring fuel cell cathodes materials: A high throughput calculation approach. ECS Transactions. 25 (2009) 1335.

[12] M. J. Eslamibidgoli, J. Huang, T. Kadyk, A. Malek, and M. Eikerling. How teory and simulation can drive fuel cell electrocatalysis. Nano Energy. 29 (2016) 334.

[13] O. T. Holton, and J. W. Stevenson. The role of platinum in proton exchange membrane fuel cells. Platinum Metals Review. 57 (2013) 259.

[14] P. Sotelo-Mazón, R. G. González-Huerta, J. G. Cabañas-Moreno, and O. Solorza-Feria. Mechanically milled Ru_xFe_y electrocatalyst for oxygen reduction in acid media. International Journal of Electrochemical Science. 2 (2007) 523.

[15] L. Su, W. Jia, C. M. Li, and Y. Lei. Mechanisms for enhanced performance on platinum-based electrocatalysts in proton exchange membrane fuel cells. Chemistry & Sustainability Energy & Materials. 7 (2014) 361.

[16] W. Niu, D. Wang, G. Yang, J. Sun, M. Wu, Y. Yoneyman, and N. Tsubaki. Pt nanoparticles loaded on reduced graphene oxide as an effective catalyst for the direct oxidation of 5-hydroxymethylfurfural (HMF) to produce 2,5-furandicarboxylic acid (FDCA) under mild conditions. Bulletin of the Chemical Society of Japan. 87 (2014) 1124.

[17] E. Bekyarova, S. Sarkar, S. Niyogi, M. E. Itkis, and R. C. Haddon. Advances in the chemical modification of epitaxial graphene. Journal of Physics D. Applied Physics. 45 (2012) 154009.

Chapter II

Background

2.1 Fuel cells: Fundamental aspects.

Fuel cells (FCs) are electrochemical devices that convert the free energy of chemical reactions into electrical energy with high conversion efficiency (more than twice compared with that of internal combustion engines). Furthermore, since no combustion process occurs during its operation, fuel cells have a low environmental impact.[1-4] The operating principle of fuel cells is similar to that of batteries, i.e., electrochemical reactions are carry out to generate electricity. However, unlike a battery, a fuel cell operates as long as both fuel and oxidant are supplied to the system.[5-7]

Fuel cells are generally classified according to the working temperature (low, medium or high) and to the nature of the electrolyte employed, as seen in Table 2.1.[5,8-10]

Figure 2.1 is a schematic representation of a hydrogen-fueled PEMFC. The fuel is supplied in the anode compartment, where a catalyst promotes the Hydrogen Oxidation Reaction (HOR) releasing protons and electrons (Reaction 2.1). The Proton Exchange Membrane, which is a physical barrier between the electrodes must allow only positively charged ions (H^+) to pass from the anode to the cathode. The electrons are transported by an external circuit generating an electrical current. Simultaneously, the oxidant (usually oxygen from air) is supplied at the cathode, reacting with the electrons and protons to carry out the oxygen reduction reaction (ORR) (Reaction 2.2). The overall reaction is presented in reaction 2.3, in which water is the only reaction product.[11-13]

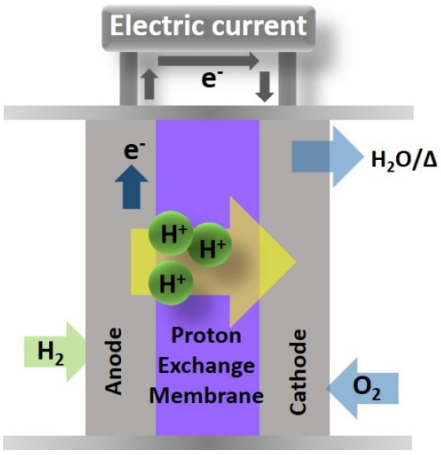

Figure 2.1 Schematic representation of a PEMFC (H_2/O_2).

Hydrogen Oxidation Reaction (HOR) $$H_2 \rightarrow 2H^+ + 2e^-$$ (2.1)

$E°_a$ = 0 V/SHE

Oxygen Reduction Reaction (ORR) $$1/2O_2 + 2H^+ + 2e^- \rightarrow H_2O$$ (2.2)

$E°_c$ = 1.23 V/SHE

Overall reaction $$H_2 + 1/2O_2 \rightarrow H_2O$$ (2.3)

$E°_{cell}$ = 1.23 V/SHE

Table 2.1 Fuel cell types and their main characteristics.

	Fuel cell type	Electrolyte	Transported charge	Operating temperature range
Low temperature	Proton Exchange Membrane (PEMFCs)	Perfluorosulfonic acid polymer such as Nafion®	H^+	30-100°C
	Alkaline (AFCs)	Molten alkali mixture of KOH (mobile or not)	OH^-	50-200°C
Medium temperature	Phosphoric Acid (PAFCs)	Liquid phosphoric acid inmovilized in a SiC matrix.	H^+	160-210°C
High temperature	Molten Carbonate (MCFCs)	Lithium, sodium and/or potassium carbonates, soaked in a $LiAlO_2$ ceramic matrix	CO_3^{2-}	600-800°C
	Solid Oxide (SOFCs)	Oxide ion conductig ceramic as ytria stabilized zirconia (Y_2O_3-ZrO_2)	O^{2-}	600-1000°C

2.2 Anion Exchange Membrane Fuel Cells (AEMFCs).

During the development of PEMFCs, acid membranes have been intensively investigated, mostly due to the discovery of the Nafion®, a perfluorinated polymer with high conductivity and high resistance to acid environment. However, recent and significant advances in the synthesis of chemically stable anion-exchange membranes have open the opportunity for the development of the AEMFCs.[14-18]

The HOR and the ORR proceed through different mechanisms in alkaline and acid environments. Unlike PEMFCs, the ionic current in AEMFCs is due to the conduction of hydroxide ions produced from the ORR (Reaction 2.4). Simultaneously, in the anode side the hydrogen reacts with hydroxyl anions generating water and electrons (Reaction 2.5). The overall reaction is presented in Reaction 2.6.[13,19-21]

Oxygen Reduction Reaction (ORR) $O_2 + 2H_2O + 4e^- \rightarrow 4OH^-$ (2.4)

$E°_c$ = 0.40 V/SHE

Hydrogen Oxidation Reaction (HOR) $2H_2 + 4OH^- \rightarrow 4H_2O + 4e^-$ (2.5)

$E°_a$ = 0.83 V/SHE

Overall reaction $H_2 + 1/2O_2 \rightarrow H_2O$ (2.6)

$E°_{cell}$ = 1.23 V/SHE

AEMFCs have several advantages compared to PEMFCs, including much improved kinetics of electrochemical reactions. Also, AEMFCs are easier to handle as the operating temperature is relatively low (23-70°C) and the less corrosive alkaline environment ensure a longer life-cycle.[22-26]

2.2.3 Alkaline Direct Alcohol Fuel Cells (ADAFCs).

The advantages of hydrogen-fueled AEMFCs including high efficiency, high power density and zero/low emission of pollutants and greenhouse gases have attracted world-wide research. However, there are still significant challenges regarding the production, transportation, storing and handling of gaseous H_2. Research has been done dedicated to overcome the restrictions of hydrogen use, since they represent serious limitations for the implementation of the hydrogen fuel cell technology. [27-32]

The use of low-molecular weight alcohols, such as methanol (CH_3OH) and ethanol (C_2H_5OH), appears advantageous over hydrogen use for several reasons: these alcohols are liquid at ambient temperature and pressure (thereby easy to handle, store, distribute and transport), are of relatively low cost and possess a high theoretical energy density (6.1 and 8.0 kWh kg^{-1}, respectively) comparable to that of gasoline (12 kWh kg^{-1}). Furthermore, ethanol can be easily produced in large quantities from agricultural products or biomass.[33-37] In this regard, ADAFCs have emerged as efficient and promising power sources for mobile, stationary and portable applications.

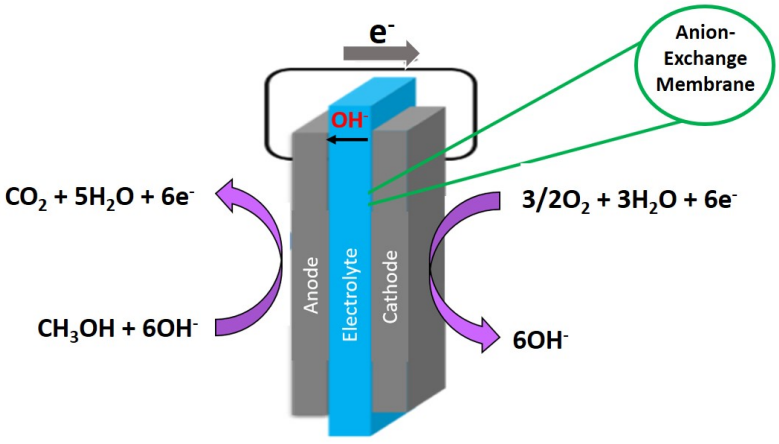

Figure 2.2 Schematic representation of an AEMFC (CH_3OH/O_2).

A schematic diagram of a methanol-fueled AEMFC is shown in Figure 2.2. On the anode, methanol reacts with the hydroxide ions producing carbon dioxide, water and six electrons (Reaction 2.7). While on the cathodic compartment, oxygen reacts with the electrons and water molecules resulting in the formation of hydroxide ions during the ORR (Reaction 2.8). The overall reaction of the methanol-fueled ADAFC is shown in Reaction 2.9. Meanwhile, in an alkaline direct ethanol fuel cell, the electrochemical processes involve the transfer of twelve electrons (Reactions 2.10-2.12). [38-41]

Methanol Oxidation	$CH_3OH + 6OH^- \rightarrow CO_2 + 5H_2O + 6e^-$	(2.7)
Reaction (MOR)	$E°_a$ = -0.81 V/SHE	
Oxygen Reduction	$3/2O_2 + 3H_2O + 6e^- \rightarrow 6OH^-$	(2.8)
Reaction (ORR)	$E°_c$ = 0.40 V/SHE	
Overall reaction	$CH_3OH + 3/2O_2 \rightarrow CO_2 + 2H_2O$	(2.9)
	$E°_{cell}$ = 1.21 V/SHE	

Ethanol Oxidation	$CH_3CH_2OH + 12OH^- \rightarrow 2CO_2 + 9H_2O + 12e^-$	(2.10)
Reaction (EOR)	$E°_a$ = -0.77 V/SHE	
Oxygen Reduction	$3O_2 + 6H_2O + 12e^- \rightarrow 12OH^-$	(2.11)
Reaction (ORR)	$E°_c$ = 0.40 V/SHE	
Overall reaction	$CH_3CH_2OH + 3O_2 \rightarrow 2CO_2 + 3H_2O$	(2.12)
	$E°_{cell}$ = 1.17 V/SHE	

2.3 The ORR in alkaline media on a Pt-catalyst.

According to Sabatier´s principle, for heterogeneous catalysis on a metal surface, the catalyst must absorb species with sufficient strength to allow chemical bonds to break but weakly enough to release the product when the reaction has occurred.[42-45] In order to find an efficient catalyst for fuel cell electrochemical reactions, a correlation between the catalytic activity of pure

metals versus the adsorption energy has been done resulting in the so-called volcano plot.[46]

Figure 2.4 depicts a volcano plot of the oxygen reduction activity as a function of the oxygen adsorption energy. For metals that bond oxygen too strongly (linear decreasing towards more negative adsorption energy), the rate is limited by reaction products to desorb from the surface. On the other hand, the linear increasing toward more positive adsorption energy represents a weak oxygen bonding and the rate is limited by hydroxyl and electron transfer to dissociate O_2.[44,45,47,48] Accordingly, pure Pt has the highest catalytic activity for the ORR among the pure metals, since it lies close to the peak of the volcano plot.[43-44]

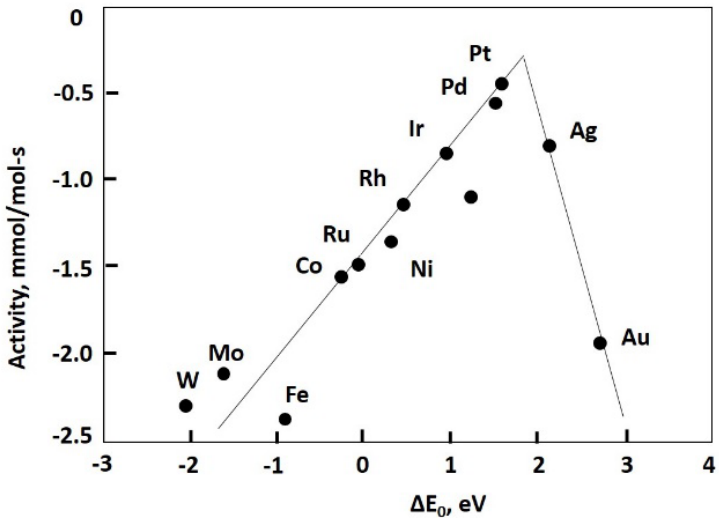

Figure 2.4 Oxygen reduction reaction activity plotted as a function of the oxygen bonding energy.[42,48-50]

The ORR plays a key role in the performance of a fuel cell due to its sluggish kinetics and resulting high overpotential. This might be one of the reasons of the intense research activity in this regard.[51,52] The ORR is kinetically slow for several reasons. One of them is the requirement of a high dissociation energy to break the strong double bond of molecular oxygen.[53,54] In addition, some

theoretical studies indicate that the adsorbed oxygenated species may affect the ORR kinetics by modulating both the reaction energetics and the number of reactive sites.[55,56]

The fundamental understanding of the ORR can be explained in terms of the electrode-electrolyte interface, illustrated in Figure 2.5. The inner Helmholtz plane (IHP) is constituted by specifically adsorbed hydroxyl species, solvent water dipoles (oriented with the oxygen atom towards the electrode surface), and chemisorbed O_2 (inset a). These species populating the IHP covalently interact with the electrode surface. On the other hand, the outer Helmholtz plane (OHP) consists of solvated species interacting with the electrode via long rate electrostatic forces, for example solvated alkali metal ions (inset b). [57-60]

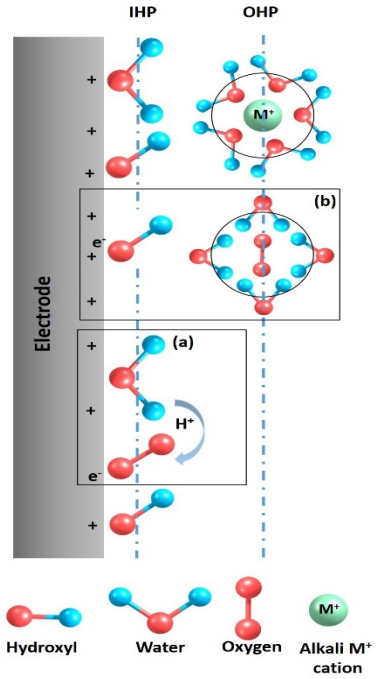

Figure 2.5 Schematic illustration of the double-layer structure during the ORR in alkaline media.[57]

In alkaline conditions, the multi-electron ORR proceeds by a 4e- transfer with a complete reduction to OH^-, or by the $2e^-$ pathway to produce the HO_2^- anion.

Both mechanisms are explained under the electrode-electrolyte interface approach. In the IHP, the electron transfer mechanism involves the chemisorption of molecular O_2 on a Pt-site (O_2*, Reaction 2.13), the O–O bonds are break to give adsorbed oxygen atoms (O*, Reaction 2.14) which react with electrons and water molecules to form OH^- groups following a $4e^-$ transfer pathway. In alkaline media, water molecules not only act as solvent but also serve as the source of ions.

The $4e^-$ pathway can be either a direct or a serial route. The direct pathway involves the transfer of $4e^-$ to adsorbed oxygen atoms to form OH^- without the formation of peroxide intermediates (Reaction 2.15). The serial $4e^-$ pathway involves sequential transfer of electrons to O* to form adsorbed peroxide species, which without desorbing from the surface is involved in another $2e^-$ transfer to form hydroxyl species (Reactions 2.16 - 2.19).

The $4e^-$ mechanism is expected to occur on high performance Pt-based catalysts, since no intermediates, such as HO_2^-, remain adsorbed on the metal active sites after OH^- production.[57]

$$Pt + \mathrm{O_2} \rightarrow Pt - {O_2}^* \quad (2.13)$$

$$Pt - {O_2}^* \rightarrow Pt - 2O^* \quad (2.14)$$

$$Pt - 2O^* + 2H_2\mathrm{O} + 4\mathrm{e}^- \rightarrow \mathrm{Pt} + 4OH^- \quad (2.15)$$

$$Pt - 2O^* + H_2\mathrm{O} + \mathrm{e}^- \rightarrow \mathrm{Pt - OOH} + OH^- \quad (2.16)$$

$$\mathrm{Pt - OOH} + e^- \rightarrow [Pt - OOH]^- \quad (2.17)$$

$$[Pt - OOH]^- + H_2\mathrm{O} + \mathrm{e}^- \rightarrow \mathrm{Pt - OH} + 2OH^- \quad (2.18)$$

$$\mathrm{Pt - OH} + \mathrm{e}^- \rightarrow \mathrm{Pt} + OH^- \quad (2.19)$$

On the other hand, in the OHP, the electron transfer mechanism occurs only at the oxide-covered metal sites. The solvated molecular O_2 weakly interacts with adsorbed hydroxyl species to promote a $2e^-$ reaction pathway giving the HO_2^-

anion as the reaction product (Reaction 2.20), which is subsequently desorbed from the surface (Reaction 2.21). [57-60]

$$Pt - OH + [O_2 \cdot (H_2O)_n]_{aq} + 2e^- \rightarrow \mathrm{Pt - OH} + HO_2{}^{-*} + OH^- + (H_2O)_{n-1} \quad (2.20)$$

$$HO_2{}^{-*} \rightarrow HO_2{}^- aq \quad (2.21)$$

2.4 Pt-based catalysts for the ORR.

As already mentioned, Pt possess the highest catalytic activity for the ORR. However, positioned slightly to the left of the Volcano peak, it strongly adsorbs oxygen intermediate species by about 100 mV.[43,44] Therefore, there is an area of improvement for the design of ORR catalysts. One of the most studied approaches is to use co-catalysts to enhance the performance of Pt.

2.4.1 Pt-Metal alloys.

The catalytic properties of Pt towards the ORR strongly depend on its oxygen adsorption energy, the dissociation energy of the O–O bond and the bonding energy of OH^- on the Pt surface. It has been demonstrated that the electronic structure of Pt (*d*-band vacancy) and Pt–Pt interatomic distance can strongly affect these energies.

On this context, it is generally accepted that alloying Pt with other metals is an efficient strategy to improve its catalytic activity. The interactions between the two metals result in modifications of the electronic structure of Pt, since the electron transfer from the other metal due to differences in their electronegativity causes a shift of its *d*-band center (electronic effect).[61] Furthermore, the alloying causes a lattice contraction, leading to a more favorable Pt–Pt distance for the dissociative adsorption of O_2 (geometric effect). It has been demonstrated that when Pt is alloyed with Cr, Mn, Fe, Co

and Ni, a two- to four-fold improvement in ORR specific activity, compared with a Pt catalyst, can be achieved.[32,48,49,62,63]

2.4.2 Pt-Metal oxides.

Some studies have focused on the catalytic properties of Pt nanoparticles modified by metal oxides. Pt-CeO_2/C,[64-67] Pt-TiO_2/C[68-70] and Pt-WO_3/C[70,71] systems exhibit increased catalytic activity toward the ORR compared with Pt/C. The enhancement in catalytic activity is due to the existence of strong Pt-metal oxide interactions, which are capable to induce changes in the Pt electronic structure.

Furthermore, it has been reported that the incorporation of an oxygen storage co-catalyst into the cathode material (such as CeO_2) increases the local oxygen concentration. The studies propose that cerium oxide acts as a supplier of oxygen to the Pt surface, leading to an enhanced catalytic activity of Pt-CeO_2/C for the ORR and thus a better performance of the fuel cell.[66,72-75]

2.4.3 Metaltitanates as co-catalysts of Pt in fuel cell reactions.

The metaltitanates ($MTiO_3$) containing metals such as Sr[76-78] or Ba[79] are well known functional inorganic materials with applications as electrodes for Solid Oxide Fuel Cells (SOFCs), since they exhibit suitable characteristics for efficient electrode operation: high electronic conductivity, high oxide ion conductivity and high catalytic activity as well as electrochemical stability. Although $NiTiO_3$[80,81] and $CoTiO_3$[82-83] have been widely used as a visible-light photocatalysts for removal of aqueous organic pollutants and for photoelectrochemical water splitting, their applications in fuel cells has been recently studied, especially for $NiTiO_3$.

For example, the $NiTiO_3$ compound has been used as a novel SOFC anode reforming layer to improve the carbon tolerance of commonly used Ni-based electrodes, which is produced from the cracking reaction of hydrocarbon fuels.[84,85]

Li *et al.*[86] reported the electrochemical performance for the ORR in alkaline media of an N-doped catalyst composed of an intermetallic CoTi core and a composite $CoTiO_3$ oxide shell (N-CoTi@$CoTiO_3$/C), which exhibits superior specific activity than that of commercial Pt/C.

Due to the promising properties of metaltitanates, several attempts have been made to try to elucidate the role of $NiTiO_3$ in catalytic reactions. A work performed by Ruiz-Preciado *et al.*[87] discusses the electrochemical response of a $NiTiO_3$ anode for the methanol oxidation reaction (MOR) in alkaline conditions. The authors conclude that the reaction takes place at Ni^{3+} sites after the oxidation of $Ni(OH)_2$ to NiO(OH). Conversely, Chellasamy *et al.*[88] propose that the MOR on the $NiTiO_3$ surface occurs with the formation of an oxide layer of $NiTiO_{3-x}(OH)_x$ on the surface of the electrode containing Ni^{2+}, Ti^{3+} and Ti^{4+} cations and the chemisorbed OH^- species act as reaction sites. The Ti^{3+}/Ti^{4+} ions bridged with oxygen species are involved in the oxidation reaction and are transferred to the electrode. Methanol initially gets adsorbed in the titanium site, at the same time the alcoholic proton transfers to a basic site (Ni-site). Subsequently the methoxy group might become oxidatively decomposed by concomitant proton abstraction from the methyl moiety and the electron transferred to the reduced metal at Ti-sites, forming a strongly adsorbed carbon monoxide species. This adsorbed CO is removed from the electrocatalyst surface by reacting with surface oxygen that subsequently transfers electron to the Ti-sites and releases CO_2.

Recently, the use of $NiTiO_3$ as co-catalyst to Pt has been also studied, given emphasis of their improved performance (compared to Pt/C) in anode and cathode fuel cells reactions.[89-91] Velumani *et al.*[89] reported that the enhancement of the catalytic activity for the MOR is promoted by the addition of the $NiTiO_3$ compound as co-catalyst to Pt due to a strong synergistic interaction. The peak current density of the MOR reaches 98 mA cm^{-2} (at 0.15 V/SHE) in alkaline conditions, which is higher than that of Pt/C (47.3 mA cm^{-2}, at 0.05 V/SHE). The hydrogenation of methanol molecules occurs on Pt by interacting with hydroxide species formed intermediate CO species, which are adsorbed on Pt sites. The authors propose that in anodic reactions, $NiTiO_3$ has the ability to absorb OH^- ions (active oxygen) from the aqueous electrolyte (Reaction 2.22) and supply them to Pt sites to oxidize the CO molecules at low overpotentials (Reaction 2.23).

$$NiTiO_3 + H_2O \rightarrow NiTiO_{3-x}(OH) + H^+ + e^- \quad (2.22)$$

$$Pt - CO_{ads} + NiTiO_{3-x}(OH) \rightarrow Pt + NiTiO_{3-x} + CO_2 + H^+ + e^- \quad (2.23)$$

Later, the same group has proposed an anode electrocatalyst based on Pt-Ru-$NiTiO_3$/C for the MOR in acid media.[90] The enhanced electrocatalytic performance of Pt-Ru-$NiTiO_3$/C is attributed to the mixed synergetic effect of Ru and $NiTiO_3$, which promotes the formation of oxygenated species and their supply to Pt, to remove the CO_{ads} from the catalytic sites. This is supported by the shifting in onset potential to more negative values (0.22 V/SHE), compared with Pt-Ru/C and Pt-$NiTiO_3$/C (0.28 and 0.36 V/SHE). Also, the peak current density in the forward scan on Pt-Ru-$NiTiO_3$/C reaches 74 mA cm^{-2} at 0.85 V, while Pt-Ru/C and Pt-$NiTiO_3$/C deliver 25.2 mA cm^{-2} at 0.82 V/SHE and 54.5 mA cm^{-2} at 0.8 V/SHE, respectively.

2.5 Carbon structures as support for fuel cells catalysts.

Carbonaceous materials including activated carbon, carbon black and graphitized carbon, have been used over the past decades as supports for fuel cell catalysts. The physical and chemical properties of these materials such as their surface chemistry, allow to anchor and disperse catalytic nanoparticles which have the function of electrochemical active sites.[91]

In particular, it has been demonstrated that the textural and surface chemical properties of the support influence the electrochemical activity of Pt catalysts (Pt/C), having an effect on its particle size, morphology, size distribution, dispersion and stability. In addition, since the catalyst is attached to the support, the bond interactions can potentially influence the catalytic activity of the catalyst by modifying its electronic structure. Thus, the choice of a support with adequate properties may improve the metal-carbon interactions, increasing the durability of the catalyst.[92-94]

On this context, fuel cells require a carbon support with the following specific characteristics: 1) high specific surface area, to achieve high nanoparticles dispersion, since the catalytic activity of a catalyst increases as a function of the reaction surface area; 2) suitable pore structure for the adequate diffusion of reactant and by-products, specifically a mesoporous structure is preferred; 3) high electrical conductivity so that electrons can be transferred easily; and 4) corrosion resistance, because the support corrosion might affect the performance and stability of the Pt-catalyst especially in the cathode, since the ORR occurs at potentials closer to those where oxidation of carbon can also occur. On this issue, when carbon is oxidized, the Pt-support interaction may be weakened causing the catalyst degradation, mainly by the dissolution of Pt and the agglomeration of metallic particles into large clusters.[95-97]

2.5.1 Carbon black: Vulcan XC-72.

Carbon blacks are obtained from the pyrolysis of hydrocarbons such as natural gas or oil fractions from the processing of petroleum.[98] Vulcan XC-72 is a microporous (diameters of less 4 nm) carbon black frequently used as electrocatalysts support in low-temperature fuel cells because of its reasonable balance among electronic conductivity, surface area, high availability and low cost.[93,98] It has a specific surface area of around 250 m^2 g^{-1} and is composed by aggregates (average diameter of 250 nm) of spherical particles with a size range of 30 to 60 nm.[91,98,99]

2.5.2 Reduced Graphene Oxide (rGO).

Graphene as a unique two-dimensional and single-atom thick structure with sp^2-hybridized carbon atoms arranged in an hexagonal network. It has been demonstrated that single-layer graphene possesses a unique combination of electrical, mechanical, optical and thermal properties.[100,101] In 2004, the first graphene monolayer sheets have been obtained by exfoliating the three-dimensional graphite using a technique called micro-mechanical cleavage.[100,102]

However, the most commonly method to obtain graphene nanosheets is the Hummers method, which consists in oxidizing the natural graphite to graphene oxide (GO) using $KMnO_4$ and $NaNO_3$ in concentrated H_2SO_4. It has a similar layered structure of graphite, but the carbon plane in graphite oxide is heavily decorated by oxygen functional groups. These oxidized layers are exfoliated in water under ultrasonic treatment obtaining one or few layers of carbon atoms, which can be (partially) reduced to graphene like-sheets (rGO) by removing the oxygenated species using strong reducing agents such as hydrazine or $NaBH_4$ recovering the conjugated structure (Figure 2.6 is a schematic representation of the graphene structures obtained with the methodologies described here).[102-105]

Due to the unique characteristics of graphene-based materials, it has been quite interesting to investigate their performance as fuel cell catalysts support. It has been demonstrated that the lattice defects (vacancies, holes) and surface functional groups (carbonyls, epoxides, hydroxyls, etc.) in the rGO structure act as nucleation centers that limit the growth of Pt-nanoparticles.[100,107] In addition, because of the strong metal-support interaction (the partially filled π-orbitals of the sp^2-hybridization of C=C bonds interacting with the Pt *d*-orbital) the stability of the catalysts can be improved by dispersing them on the high specific surface area RGO (theoretical value of ~2600 $m^2 g^{-1}$).[100,107,108] He *et al.*[109] have demonstrated that the stability and the catalytic activity for the ORR of a Pt/RGO catalyst can be greatly improved by preserving a proper amount of oxygenated groups on the rGO surface.

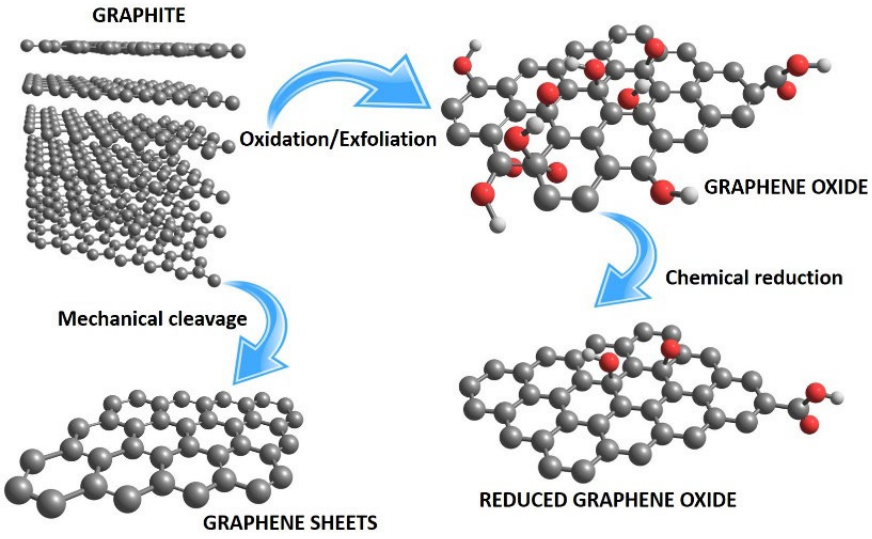

Figure 2.6 Schematic representation of the structures of graphite, GO, rGO and graphene sheets.[106]

The current research has focused on demonstrating the potential advantages of the graphene-based materials over the commonly used carbon blacks supports. Kou *et al.*[110] have compared the stability and electrochemical activity

for the ORR of Pt-nanoparticles supported on graphene sheets (GS) and carbon blacks (20 % Pt supported on Vulcan XC-72, E-TEK). Pt/GS showed not only high specific surface area and enhanced activity for the ORR, but also excellent stability after 500 voltammetry cycles.

Ha *et al.*[111] have synthesized a Pt/rGO catalyst using $NaBH_4$ to reduce H_2PtCl_6 in a GO suspension forming a GO-H_2PtCl_6 composite. Pt/rGO catalyst was obtained via the chemical reduction of GO and Pt using ethylene glycol and $NaBH_4$ as reducing agents. TEM analysis showed that Pt-nanoparticles with a diameter of about 3 nm were uniformly dispersed on the rGO surface. In electrochemical measurements, the Pt/rGO catalyst exhibited enhanced catalytic activity for the ORR than commercial Pt/C. Using a similar experimental technique, Pt/rGO has been prepared by Xin *et al.*[112] showing better catalytic activity for the ORR than Pt/C (C = Vulcan XC-72, synthesized by the same procedure).

2.6 Functionalization of carbon supports.

The ability to control the surface properties of carbon nanostructures, i.e., surface modification, has been very helpful in improving the performance of fuel cell catalyst. Essentially, covalent and non-covalent modification methods have been used to functionalize the surface of carbonaceous materials. Covalent surface modification involves a permanent modification of the carbon surface by creating bonds between the carbon atoms and functional groups. Non-covalent functionalization is based only on electrostatic interactions, Van der Waals forces, hydrogen bonding and other type of attractive forces.[113,114] For example, the non-covalent association of carbon nanotubes with polymers such as poly(vinyl pyrrolidone) and poly(styrene sulfonate) disrupt their intrinsic hydrophobic interface allowing their solubility in water. Additionally, the reactive groups of the polymers can interact with specific molecules.[115,116]

Covalent surface oxidation is probably the most widely used chemical modification of carbon. Chemical agents such as HNO_3, H_2SO_4, citric acid, acetic acid, $KMnO_4$, $K_2Cr_2O_7$, KOH and H_2O_2 are capable of introducing oxygen functionalities (hydroxyl, carboxyl and carbonyl groups). These oxygenated functional groups serve as metal-anchoring sites. This way, Pt nanoparticles dispersion is improved and thereby a high electrochemical activity is obtained.[113,117]

The first attempt to clarify the influence of surface functional groups on the catalytic behavior of carbon-supported catalysts has been made by Derbyshire *et al.*[118] Later, Prado-Burguette *et al.*[119] have reported their studies of the effect of surface oxygenated groups on the dispersion of Pt-nanoparticles. They used several carbon black supports with different content of oxygen surface groups created by an oxidation treatment with H_2O_2. It was observed that the presence of more oxygenated groups improve the hydrophilic character of the carbon surface, thus enhancing the dispersion.

Despite the fact that a wide variety of compounds have been used to modify the surface properties of the carbon nanostructures, it has been demonstrated that the carbon surface functionalization with aggressive agents, for example covalent surface oxidation, can modify the intrinsic graphitized lattice of graphene-based materials due to the transformation of sp^2-hybridization to a distorted sp^3-geometry.[120]

2.6.1 Organometallic functionalization of carbon nanostructures.

The organometallic chemistry, a subfield of coordination chemistry, involves the synthesis, structure and reactivity of complexes that contain direct metal-carbon (M–C) bonds. This interdisciplinary area lies between organic and

inorganic chemistry, studying the interaction of inorganic metal species with carbon atoms from an organic molecule (ligand). [121]

In organometallic chemistry, the metal–ligand interactions determine the reactivity of the complex (i.e. the lability to react with other molecules) since the metallic atom as well as the type of ligand add a specific functionality.[122] Transition metals can bond to multiple carbon atoms by a single metallic ligand. The coordination of a ligand to a metal center by carbon atom is known as hapticity (η^n, n = number of carbon atoms coordinated). In consequence, the specific and variable architectures provided by the coordination geometry results in important changes at molecular level.[123]

Arenes are probably the most interesting classes of π-ligands in organometallic chemistry. Owing to their ability to provide up to six sites for metal coordination ($\eta^1 – \eta^6$) a wide range of metal-arene complexes are known, many of which are crucial intermediaries in homogeneous catalysis. Also, it is known that the transition metals change the reactivity of the complexed arenes, including C-H bond activation and the susceptibility towards nucleophilic reactions. Thus, transition metal complexes with arene ligands represent an important group of the organometallic compounds.[124-126]

Recently, coordination complexes of transition metals with graphitic materials are of interest from the standpoint of their technological applications, mainly as conjugated organometallic catalysts (including energy storage and conversion) and as electronic and magnetic materials.[127,128]
One of the first organometallic reactions of carbon nanostructures has been reported by Ajayan *et al.*[129] where a reaction of carbon nanotubes with sec-butyllithium was carried out. The reaction derivatives were used as initiators of anionic polymerization for the *in situ* preparation of polystyrene-grafted

nanotubes. After such publication, several groups used the strategy to graft various polymers to the surface of carbon nanotubes.[130-132] However, there are only a very limited number of reports on organometallic complexation reactions of carbon nanostructures with transition metals.

Despite being discovered more than 100 years ago by Ludwing Mond, transition metal carbonyls can still be considered as one of the most interesting classes of organometallic compounds due to their particular features: 1) facile displacement of their CO ligands by a wide variety of ligands with σ-donor and π-acceptor character (olefinic and aromatic compounds), 2) reduction of metal carbonyls affording anionic carbonyl metallates with increasing M-CO bond stability, and 3) reaction with nucleophiles occurs at the C atom of the CO ligand, extending the scope of the chemistry of transition metal carbene complexes.[133-135]

On this matter, Haddon *et al.*[127,130,136,137] have studied the surface modification of several carbon nanomaterials such as exfoliated and epitaxial graphene, highly-oriented pyrolytic graphite (HOPG) and single-walled carbon nanotubes (SWCNT) with organometallic chromium compounds of the $(Cr(CO)_6$ and $[(\eta^6\text{-}C_6H_6)Cr(CO)_3]$ type. They proposed the organometallic functionalization of carbon nanostructures with transition metal carbonyls as a promising method for introducing chemical functionalities onto a graphitic system with minimal or none disruptions of the structural integrity of the sp^2-hybridized carbon atoms.

In those reports has been observed that carbonyl ligands of the organometallic precursor were displaced and chromium atoms coordinate to the graphitic system giving organometallic complexes of formula $[(\eta^6\text{-arene})Cr(CO)_3]$, $[(\eta^6\text{-arene})Cr(benzene)]$ and $[(\eta^6\text{-arene})_2Cr]$. These complexation reactions are possible through the overlapping of the occupied π-orbitals of the graphitic

lattice with the vacant d_{π}-orbitals of the transition metal, resulting in the hexahapto (η^6) coordination of the metal atom to an individual benzene ring of the aromatic system. The functionalization process was classified as a covalent chemisorption interaction, in which the formation of an organometallic hexahapto (η^6)-metal fragment preserves the graphitic structure (constructive rehybridization).

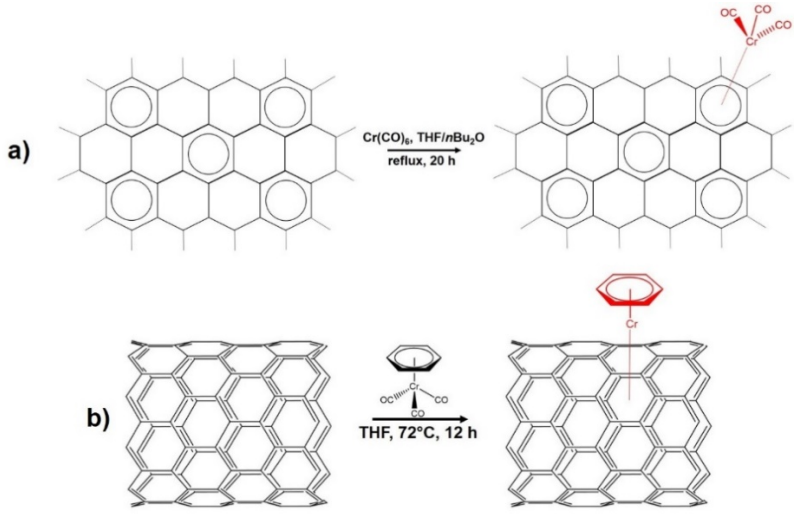

Figure 2.7 Representative reactions of carbon nanostructures with a) $Cr(CO)_6$ and b) $[(\eta^6\text{-}C_6H_6)Cr(CO)_3]$.[137]

These researches have been the guideline to the applicability of the organometallic chemistry in fuel cell technology expanding the scope of carbon nanostructures. Very recently, Siller-Ceniceros *et al.*[138] have reported the functionalization of Vulcan XC-72 with an organometallic compound, $[(\eta^6\text{-}C_6H_5OCH_2CH_2)RuCl_2]_2$, named as $C_{Ru\text{-}dim}$. The physicochemical characterization indicated that the graphitized lattice of Vulcan has not been distorted during the functionalization process. Subsequently, $C_{Ru\text{-}dim}$ was used as Pt-nanoparticles support. The authors found that the organometallic functionalities promoted a high dispersion of Pt-nanoparticles. Furthermore, the formation of a Pt-Ru alloy improved the catalytic performance of the $Pt/C_{Ru\text{-}dim}$ catalyst for the MOR in acid media.

2.7 References.

[1] F. Barbir. PEM Fuel Cells in Fuel Cell Technology. Engineering Materials and Processes. Springer, London. 2006

[2] S. Basu. Recent Trends in Fuel Cell Science and Technology. Springer, New. York. 2007.

[3] R. M. Ormerod. Solid oxide fuel cells. Chemical Society Reviews. 32 (2003) 17.

[4] P. P. Edwards, V. L. Kuznetsov, W. I. F. David, and N. P. Brandon. Hydrogen and fuel cells: Towards a sustainable energy future. Energy Policy. 36 (2008) 4356.

[5] A. B. Stambouli, and E. Traversa. Fuel cells, an alternative to standard sources of energy. Renewable & Sustainable Energy Reviews. 6 (2002) 297.

[6] M. Winter. What are batteries, fuel cells and supercapacitors?. Chemical Reviews. 104 (2004) 4245.

[7] O. Z. Sharaf, and M. F. Orhan. An overview of fuel cell technology. Renewable and Sustainable Energy Reviews. 32 (2014) 810.

[8] J. M. Andújar, and F. Segura. Fuel cells: History and updating. A walk along two centuries. Renewable and Sustainable Energy Reviews. 13 (2009) 2309.

[9] C. Song. Fuel processing for low-temperature and high-temperature fuel cells. Challenges, and opportunities for sustainable development in the 21st century. Catalysis Today. 77 (2002) 17.

[10] L. Carrete, K. Friedrich, and U. Stimming. Fuel cells: Principles, types and applications. Chemical Physics and Physical Chemistry. 1 (2000) 162.

[11] H. Gasteiger, S. Kocha, B. Sompalli, and F. Wagner. Activity benchmarks and requirements for Pt, Pt-alloy, and non-Pt oxygen reduction catalysts for PEMFCs. Applied Cataysis B: Environmental. 56 (2005) 9.

[12] Z. Chen, L. Xu, W. Li, M. Waje, and Y. Yan. Polyaniline nanofiber supported platinum nanoelectrocatalysts for direct methanol fuel cells. Nanotechnology. 17 (2006) 5254.

[13] J. R. Varcoe, and R. C. T. Slade. Prospects for alkaline anion-exchange membranes in low temperature fuel cells. Fuel Cells. 5 (2005) 187.

[14] M. L. Perry, and T. F. Fuller. A historical perspective of fuel cell technology in the 20th century. Journal of the Electrochemical Society. 149 (2002) S59.

[15] G. Merle, M. Wessling, and K. J. Nijmeijer. Anion exchange membranes for alkaline fuel cells: A review. Journal of Membrane Science. 377 (2011) 1.

[16] E. H. Yu, and K. Scott. Development of direct methanol alkaline fuel cells using anion exchange membranes. Journal of Power Sources. 137 (2004) 248.

[17] Z. Ogumi, K. Matsuoka, S. Chiba, M. Matsuoka, Y. Iriyima, T. Abe, and M. Inaba. Preliminary study on direct alcohol fuel cells employing anion exchange membrane. The Electrochemical Society of Japan. 70 (2002) 3.
[18] E. H. Yu, and K. Scott. Direct methanol alkaline fuel cells with catalyzed anion exchange membrane electrodes. Journal of Applied Electrochemistry. 35 (2005) 91.
[19] G. Merle, M. Wessling, and K. Nijmeijer. Anion exchange membranes for alkaline fuel cells. Journal of Membrane Science. 377 (2011) 1.
[20] L. An, and T. S. Zhao. Anion Exchange Membrane Fuel Cells. Principles, Materials and Systems. Springer. Switzerland, 2018
[21] E. Antolini, and E. R. González. Alkaline direct alcohol fuel cells. Journal of Power Sources. 195 (2010) 3431.
[22] Y. S. Li, and T. Zhao. A high performance integrated electrode for anion-exchange membrane direct ethanol fuel cells. International Journal of Hydrogen Energy. 36 (2011) 7707.
[23] E. H. Yu, K. Scott. Development of direct methanol alkaline fuel cells using anion exchange membranes. Journal of Power Sources. 137 (2004) 248.
[24] L. An, and T. Zhao. Performance of an alkaline direct ethanol fuel cell with hydrogen peroxide as oxidant. International Journal of Hydrogen Energy. 39 (2014) 2320.
[25] L. Carrete, K. Friedrich, and U. Stimming. Fuel cells: Principles, types and applications. Chemical Physics and Physical Chemistry. 1 (2000) 162.
[26] L. An L, and T. Zhao. An alkaline direct ethanol fuel cell with a cation exchange membrane. Energy and Environmental Science. 4 (2011) 2213.
[27] T. Zhao, S. Li, and Y. Shen. Anion-exchange membrane direct ethanol fuel cells: Status and perspective. Frontiers of Energy and Power Engineering in China. 4 (2010) 443.
[28] J. Tiwari, G. Sigh, and K. Sim K. Recent progress in the development of anode and cathode catalysts for direct methanol fuel cells. Nano Energy. 2 (2013) 553.
[29] U. Krewer, T. Koch, and L. Struckmann. Electochemical oxidation of carbon-containing fuels and their dynamics in low-temperature fuel cells. Chemical Physics and Physical Chemistry. 12 (2011) 2518.
[30] E. Antolini, T. Lopes, and E. González. An overview of platinum-based catalysts as methanol-resistant oxygen reduction materials for direct methanol fuel cells. Journal of Alloys and Compounds. 461 (2008) 253.
[31] R. M. Gupta. Hydrogen Fuel. Production, transport and storage. CRC Press. Florida, 2009.
[32] J. Zhang. PEM Fuel Cells Electrocatalysts and Catalyst Layers. Fundamentals and Applications. Springer. Vancouver, 2008.

[33] K. I. Ozoemena. Nanostructured platinum-free electrocatalysts in alkaline direct alcohol fuel cells: catalyst design, principles and applications. RSC Adv. 6 (2016) 89523.

[34] C. Lamy, A. Lima, V. LeRhun, F. Delime, C. Coutanceau, and J. M. Léger. Recent advances in the development of direct alcohol fuel cells (DAFC). Journal of Power Sources. 105 (2002) 283.

[35] U. B. Demirci. Direct liquid-feed fuel cells: Thermodynamic and environmental concerns. Journal of Power Sources. 169 (2007) 239.

[36] K. Matsuoka, Y. Iriyama, T. Abe, M. Matsuoka, and Z. Ogumi. Alkaline direct alcohol fuel cells using an anion exchange membrane. Journal of Power Sources. 150 (2005) 27.

[37] F. Vigier, S. Rousseau, C. Coutanceau, J. M. Leger, and C. Lamy. Electrocatalysis for the direct alcohol fuel cell. Topics in Catalysis. 40 (2006) 111.

[38] E. H. Yu, and K. Scott. Development of direct methanol alkaline fuel cell using anion exchange membranes. Journal of Power Sources. 137 (2004) 248.

[39] E. H. Yu. U. Krewer, and K. Scott. Principles and materials aspects of direct alkaline alcohol fuel cells. Energies. 3 (2010) 1499.

[40] E. H. Yu, X. Wang, U. Krewer, L. Le, and K. Scott. Direct oxidation alkaline fuel cells: From materials to systems. Energy & Environmental Science. 5 (2012) 5668.

[41] T. Maiyalaga, and V. S. Saji. Electrocatalysis for Low Temperature Fuel Cells. Fundamentals and Recent Trends. Wiley-VCH. Germany, 2017.

[42] O. T. Holton, and J. W. Stevenson. The role of platinum in proton exchange membrane fuel cells. Platinum Metals Review. 57 (2013) 259.

[43] J .L. Gavartin, M. Sarwar, D. C. Papageorgopoulos, D. Gunn, S. García, A. Perlov, A. Krystala, D. L. Ormsby, D. Thompsett, G. G. Wood, A. Andersen, and S. French. Exploring fuel cell cathode materials. A high throughput calculation approach. ECS Transactions. 25 (2009) 1335.

[44] M. J. Eslamibidgoli, J. Huang, T. Kadyk, A. Malek, and M. Eikerling. How theory and simulation can drive fuel cell electrocatalysis. Nano Energy. 29 (2016) 334.

[45] P. Quaino, F. Juárez, E. Santos, and W. Schmickler. Volcano plots in hydrogen electrocatalysis – uses and abuses. Beilstein Journal of Nanotechnology. 5 (2014) 846.

[46] J. Norskov, J. Rossmeisl, A. Logadottir, L. Lindqvist, J. Kitchin, T. Bligaard, and H. Jonsson. Origin of the overpotential for oxygen reduction at a fuel-cell cathode. Journal of Physical Chemistry B. 108 (2004) 17886.

[47] Y. Lu, S. Du, and R. S. Wilckens. One-dimensional nanostructured electrocatalysts for polymer electrolyte membrane fuel cells. A review. Applied Catalysis B: Environmental. 199 (2016) 292.

[48] Y. Nie, L. Li, and Z. Wei. Recent advances in Pt and Pt-free catalysts for oxygen reduction reaction. Chemical Society Reviews. 44 (2015) 2168.
[49] J. Stacy, Y. N. Regmi, B. Leonard, and M. Fan. The recent progress and future of oxygen reduction reaction catalysts: A review. Renewable and Sustainable Energy Reviews. 69 (2017) 401.
[50] N. V. Long, C. M. Thi, Y. Yong, M. Nogami, and M. Ohtaki. Platinum and palladium nano-structured catalysts for polymer electrolyte fuel cells and direct methanol fuel cells. Journal of Nanoscience and Nanotechnoloy. 13 (2013) 4799.
[51] O. T. Holton, and J. W. Stevenson. The role of platinum in proton exchange membrane fuel cells. Platinum Metals Review. 57 (2013) 259.
[52] S. Chen, J. Bi, Y. Zhao, L. Yang, C. Zhang, Y. Ma, Q. Wu, X. Wang, and Z. Hu. Nitrogen-doped carbon nanocages as efficient metal-free electrocatalysts for oxygen reduction reaction. Advanced Materials. 24 (2012) 5593.
[53] P. Sotelo-Mazón, R. G. González-Huerta, J. G. Cabañas-Moreno, and O. Solorza-Feria. Mechanically milled Ru_xFe_y electrocatalyst for oxygen reduction in acid media. International Journal of Electrochemical Science. 2 (2007) 523.
[54] J. X. Wang, J. Zhang, and R. R. Adzic. What matters after first electron transfer in oxygen reduction: A kinetic study of Pt(111) and Pt/C thin layer catalysts on rotating disk electrodes. American Chemical Society Division Of Fuel Cell Chemistry. 49 (2004) 664.
[55] J. Chen, L. Fang, Y. Liu, and S. Chen. Electrocatalytic O2 reduction on Pt: Multiple roles of oxygenated adsorbates, nature of active sites, and origin of overpotential. The Journal of Physical Chemistry C. 121 (2017) 6209.
[56] D. H. Lim, and J. Wilcox. Mechanisms of the oxygen reduction reaction on defective graphene-supported Pt nanoparticles from first principles. The Journal of Physical Chemistry C. 116 (2012) 3653.
[57] N. Ramaswamy, and S. Mukerjee. Fundamental mechanistic understanding of electrocatalysis of oxygen reduction on Pt and non-Pt surfaces: Acid versus alkaline media. Advances in Physical Chemistry. 2012 (2011) 1.
[58] X. Ge, A. Sumboja, D. Wuu, T. An, B. Li, F. W. Thomas, T. S. Andy, Y. Zong, and Z. Liu. Oxygen Reduction in alkaline media: From mechanisms to recent advances of catalysts. ACS Catalysis. 5 (2015). 4643.
[59] J. Bisquert. Nanostructured Energy Devices. Equilibrium, Concepts and Kinetics. CRC Press. Florida, 2015.

[60] M. G. Hosseini, and P. Zardari. Electrocatalytical study of carbon supported Pt, Ru, and bimetallic Pt-Ru nanoparticles for oxygen reduction reaction in alkaline media. Applied Surface Science. 345 (2015) 223.

[61] L. Su, W. Jia, C. M. Li, and Y. Lei. Mechanisms for enhanced performance on platinum-based electrocatalysts in proton exchange membrane fuel cells. Chemistry & Sustainability Energy & Materials. 7 (2014) 361.

[62] T. Toda, H. Igarashi, H. Uchida, and M. Watanabe. Enhancement of the electroreduction of oxygen on Pt alloys with Fe, Ni and Co. Journal of the Electrochemical Society. 146 (1999) 3750.

[63] Y. Bing, H. Liu, L. Zhang, D. Ghosh, and J. Zhang. Nanostructured Pt-alloy electrocatalysts for PEM fuel cell oxygen reduction reaction. Chemical Society Reviews. 39 (2010) 2184.

[64] X. Yu, J. He, D. Wang, Y. Hu, H. Tian, Z. He. Facile controlled synthesis of Pt-MnO2 nanostructured catalysts and their catalytic performance for oxidative decomposition of formaldehyde. The Journal of Physical Chemistry C. 116 (2012) 851.

[65] D. H. Lim, W. D. Lee, D. H. Choi, H. I. Lee. Effect of ceria nanoparticles into the Pt/C catalyst as cathode material on the electrocatalytic activity and durability for low-temperature fuel cell. Applied Catalysis B: Environmental. 94 (2010) 85.

[66] M. Takahashi, T. Mori, H. Yoshikawa, H. Togasaki, K. Fugane, A. Tada, V. Matolin, and J. Drennan. Influence of Pt and CeO_2 interaction in Pt-CeO_2 electrode on anode and cathode performance for fuel cell applications. Transactions of the Materials Research Society of Japan. 33 (2008) 1101.

[67] A. Altamirano-Gutierrez, A. M. Fernández, and F. J. Rodríguez-Varela. Preparation and characterization of Pt-CeO_2 and Pt-Pd electrocatalysts for the oxygen reduction in the absence and presence of methanol in alkaline medium. International Journal of Hydrogen Energy. 38 (2013) 12657.

[68] K. Klak, D. Marks, A. Wadas, M. Piatek, W. Lotowska, S. Zoladek, I. A. Rutkowska, and P. J. Kulesza. Nanostructured hybrid electrocatalytic material for ethanol oxidation: Activation of Pt-Ru centers through modification with selected metal oxides. ECS Transactions. 45 (2013) 13.

[69] S. Shanmugam, and A. Gedanken. Synthesis and electrochemical oxygen reduction reaction of platinum nanoparticles supported on mesoporous TiO_2. The Journal of Physical Chemistry C. 113 (2009) 18707.

[70] A. Lewera, L. Timperman, A. Roguska, and N. A. Vante. Metal-support interactions between nanosized Pt and metal oxides (WO_3 and TiO_2) studied using X-ray photoelectron spectroscopy. The Journal of Physical Chemistry C. 115 (2011) 20153.

[71] Y. Liu, S. Shrestha, and W. E. Mustain. Synthesis of nanosize tungsten oxide and its evaluation as an electrocatalyst support for oxygen reduction in acid media. ACS Catalysis. 2 (2012) 456.

[72] H. B. Yu, J. H. Kim, H. I. Lee, M. A. Scibioh, J. Lee, J. Han, S. P. Yoon, and H. Y. Ha. Development of nanophase CeO_2-Pt/C cathode catalyst for direct methanol fuel cell. Journal of Power Sources. 140 (2005) 59.

[73] M. A. Scibioh, S. K. Kim, E. A. Cho, T. H. Lim, S. A. Hong, and H. Y. Ha. Pt-CeO_2/C anode catalyst for direct methanol fuel cells. Applied Catalysis B: Environmental. 84 (2008) 773.

[74] D. R. Ou, T. Mori, K. Fugane, H. Togosaki, F. Yei, and J. Drennan. Stability of ceria supports in Pt-CeO_x/C catalysts. The Journal of Physical Chemistry C. 115 (2011) 19239.

[75] T. Mori, D. R. Ou, J. Zou, and J. Drennan. Present status and future prospect of design of Pt-cerium oxide electrodes for fuel cell applications. Progress in Natural Science: Materials International. 22 (2012) 561.

[76] H. Kurokawa, L. Yang, C. P. Jacobson, L. C. De Jonghe, and S. J. Visco. Y-doped $SrTiO_3$ based sulfur tolerant anode for solid oxide fuel cells. Journal of Power Sources. 164 (2007) 510.

[77] X. Li, H. Zhao, W. Shen, F. Gao, X. Huang, Y. Li, and Z. Zhu. Synthesis and properties of Y-doped $SrTiO_3$ as anode material for SOFCs. Journal of Power Sources. 166 (2007) 47.

[78] P. R. Slater, D. P. Fragg, and J. T. S. Irvine. Synthesis and electrical characterization of doped perovskite titanates as potential anode materials for solid oxide fuel cells. Journal of Materials Chemistry. 7 (1997) 2495.

[79] J. H. Li, X. Z. Fu, J. L. Lou, K. T. Chuang, and A. R. Sanger. Application of BaTiO3 as anode materials for H_2S-containing CH_4 fueled solid oxide fuel cells. Journal of Power Sources. 213 (2012) 69.

[80] Y. Qu, W. Xhou, Z. Ren, S. Du, X. Meng, G. Tian, K. Pan, G. Wang, and H. Fu. Facile preparation of porous $NiTiO_3$ nanorods with enhanced visible-light-driven photocatalytic performance. Journal of Materials Chemistry. 22 (2012) 16471.

[81] A. A. Tahir, M. Mazhar, M. Hamid, F. K. Upul, and K. C. Molloy. Photooxidation of water by $NiTiO_3$ deposited from single source precursor $[Ni_2Ti_2(OEt)_2(-\mu OEt)_6(acac)_4]$ by AACVD. Dalton Transactions.19 (2009) 3674.

[82] K. Wangkawong, S. Phanichphant, D. Tantraviwat, and B. Inceesungvorn. $CoTiO_3/Ag_3VO_4$ composite: A study on the role of $CoTiO_3$ and the active species in the photocatalytic degradation of methylene blue. Journal of Colloid and Interface Science. 15 (2015) 210.

[83] Y. Qu, W. Zhou, and H. Fu. Porous cobalt titanate nanorod: A new candidate for visible light-driven photocatalytic water oxidation. Chem. Cat. Chem. 6 (2014) 265.

[84] Z. Wang, Z. Wang, W. Yang, R. Peng, and Y. Liu. Carbon-tolerant solid oxide fuel cells using $NiTiO_3$ as an anode internal reforming layer. Journal of Power Sources. 225 (2014) 404.
[85] W. Cai, X. Fu, T. Guo, H. Chen, L. Zhao, X. Ou, P. Feng, and Y. Ling. An active functional layer of carbon-tolerant anode of intermediate temperature solid oxide fuel cells. Materials Letters. 208 (2017) 54.
[86] A. Li, Y. Huijun, C. Xin, L. Baio, X. Zhonghong, and X. Dingguo. Catalytic performance and mechanism of N-CoTi@$CoTiO_3$ catalysts for oxygen reduction reaction. Nano Energy. 20 (2016) 134.
[87] M. A. Ruiz-Preciado, A. A. Flores-Caballero. A. Manzo-Robledo, and A. Morales-Acevedo. Nanostructured $NiTiO_3$ as a catalytic material for methanol electrochemical oxidation in alkaline conditions. Journal of the Electrohcemical Society. 165 (2018) H24.
[88] V. Chellasamy, and P. Thangadurai. Structural and electrochemical investigations of nanostructured $NiTiO_3$ in acidic environment. Frontiers of Materials Science. 11 (2017) 162.
[89] T. Velumani, R. Manoharan, P. Karthikeyan, E. Nikhila, A. Hernández-Ramírez, and F. J. Rodríguez-Varela. Pt nanoparticles supported on $NiTiO_3$/C as electrocatalyst towards high performance methanol oxidation reaction. International Journal of Hydrogen Energy. 42 (2017) 9795.
[90] T. Velumani, P. Karthikeyan, R. Manoharan, S. Sampath, A. Hernández-Ramírez, M. E. Sánchez-Castro, I. Alonso-Lemus and F. J. Rodríguez-Varela. Pt-Ru-$NiTiO_3$ nanoparticles dispersed on Vulcan as high performance electrocatalyst for the methanol oxidation reaction. Electrocatalysis. 9 (2018) 582.
[91] E. Pérez-Mayoral, V. Calvino-Casilda, and E. Soriano. Metal-supported carbon-based materials: opportunities and challenges in the synthesis of valuable products. Catalysis Science & Technology. 6 (2016) 1265.
[92] E. Antolini. Carbon supports for low-temperature fuel cell catalysts. Applied Catalysis B: Environmental. 88 (2009) 1.
[93] Y. J. Wang, N. Zhao, B. Fang, H. Liu. X. T. Bi, and H. Wang. Carbon-supported Pt-based alloy electrocatalysts for the oxygen reduction reaction in polymer electrolyte membrane fuel cells: Particle size, shape, and composition manipulation and their impact to activity. Chemical Reviews. 115 (2015) 3343.
[94] E. Antolini. Formation, microstructural characteristics and stability of carbon supported platinum catalysts for low temperature fuel cells. Journal of Material Science. 38 (2003) 29995.
[95] H. Huang, and X. Wang. Journal of Materials Chemistry A. Recent progress on carbon-based support materials for electrocatalysts of direct methanol fuel cells. 2 (2014) 6266.

[96] J. Wang, G. Yin, Y. Shao, S. Zhang, Z. Wang and Y. Gao. Effect of carbon black support corrosion on the durability of Pt/C catalyst. Journal of Power Sources. 171 (2007) 331.
[97] S. Shahgaldi, and J. Hamelin. Improved carbon nanostructures as a novel catalyst support in the cathode side of PEMFC: A critical review. Carbon. 94 (2015) 705.
[98] Y. Wang. Nanomaterials for Direct Alcohol Fuel Cell. Pan Stanford Publishing Pte. Ltd. Singapore, 2017.
[99] I. J. Sanders, and T. L. Peeten. Carbon Black: Production, properties and uses. Nova Science Publishers, Inc. New York, 2011.
[100] M. Liu, R. Zhang, and W. Chen. Graphene-supported nanoelectrocatalysts fir fuel cells: synthesis, properties and applications. Chemical Reviews. 114 (2014) 5117.
[101] L. Dong, R. R. Sanganna-Gari, Z. Liu, M. M. Craig, and S. Hou. Graphene-supported platinum and platinum-ruthenium nanoparticles with high electrocatalytic activity for methanol and ethanol oxidation. Carbon. 48 (2010) 781.
[102] E. Antolini. Graphene as a new carbon support for low-temperature fuel cell catalysts. Applied Catalysis B: Environmental. 123-124 (2012) 52.
[103] S. V. Tkachev, E. Y. Buslaeva, A. V. Naumkin, S. L. Kotova, I. V. Laure, and S. P. Gubin. Reduced graphene oxide. Inorganic Materials. 48 (2012) 796.
[104] S. Pei, and H. M. Cheng. The reduction of graphene oxide. Carbon. 50 (2012) 3210.
[105] S. N. Alam, N. Sharma, and L. Kumar. Synthesis of graphene oxide (GO) by modified Hummers method and its thermal reduction to obtain reduced graphene oxide (rGO). Graphene. 6 (2017) 1.
[106] S. J. Rowley-Neale, E. P. Randviir, A. S. Abo-Dena, and C. E. Banks. An overview of recent applications of reduced graphene oxide as a basis of electroanalytical sensing platforms. Applied Materials Today. 10 (2018) 218.
[107] I. Fampiou, and A. Ramasubramaniam. Binding of Pt nanoclusters to point defects in graphene: Adsorption, morphology, and electronic structure. The Journal of Physical Chemistry C. 116 (2012) 6543.
[108] Y. Li, W. Gao, L. Ci, C. Wang, and P. Ajayan. Catalytic performance of Pt nanoparticles on reduced graphene oxide for methanol electro-oxidation. Carbon. 48 (2010) 1124.
[109] D. He, K. Cheng, T. Peng, X. Sun, M. Pan, and S. Mu. Bifunctional effect of reduced graphene oxides to support active metal nanoparticles for oxygen reduction reaction and stability. Journal of Materials Chemistry. 22 (2012) 21298.
[110] R. Kou, Y. Shao, D. Wang, M. H. Engelhard, J. H. Kwak, J. Wang, V. V. Viswanathan, C. Wang, Y. Lin, Y. Wang, I. A. Aksay, and J. Liu. Enhanced activity and stability of Pt catalysts

on functionalized graphene sheets for electrocatlytic oxygen reduction. Electrochemistry Communications. 11 (2009) 954.

[111] H. W. Ha, I. Y. Kim, S. J. Hwang, and R. S. Ruoff. One-pot synthesis of platinum nanoparticles embedded on reduced graphene oxide for oxygen reduction in methanol fuel cells. Electrochemical and Solid-State Letters. 14 (2011) B70.

[112] Y. Xin, J. G. Liu, Y. Zhou, W. Liu, J. Gao, Y. Xie, Y. Yin, and Z. Zou. Preparation and characterization of Pt supported on graphene with enhanced electrocatalytic activity in fuel cell. Journal of Power Sources. 196 (2011) 1012.

[113] M. Yaldagard, M. Jahanshahi, and N. Seghatoleslamil. Carbonaceous nanostructured support materials for low temperature fuel cell electrocatalysts – A review. World Journal of Nano Science and Engineering. 3 (2013) 121.

[114] B. Ladewing, S. P. Jiang, and Y. Yan. Materials for Low-Temperature Fuel Cells. Wiley-VCH. Germany, 2015.

[115] A. Vaseshta, and D. D. Malinovska. Nanostructured and nanoscale devices, sensors and detectors. Science and Technology of Advanced Materials. 6 (2005) 312.

[116] S. Banerjee, T. H. Benny, and S. S. Wong. Covalent surface chemistry of single-walled carbon nanotubes. Advanced Materials. 1 (2005) 17.

[117] J. Ye, J. Liu, Y. Zhou, Z. Zou, J. Gu and T. Yu. High catalytic performance and stability of Pt/C using acetic acid functionalized carbon. Journal of Power Sources. 194 (2009) 683.

[118] F. Derbyshire, V. H. J. de Beer, G. M. K. Abotsi, A. W. Scaroni, J. M. Solar, and D. J. Skrovanek. The influence of surface functionality on the activity of carbon-supported catalysts. Applied Catalysis. 27 (1986) 117.

[119] C. Prado-Burguete, A. Linares-Solano, F. Rodríguez-Reinoso, and C. Salinas-Martínez de Lecea. The effect of oxygen surface groups on the support on platinum dispersion in Pt/carbon catalysts. Journal of Catalysis. 115 (1989) 98.

[120] S. Stankovich, D. A. Dikin, R. D. Piner, K. A. Kohlhaas, A. Kleinhammes, Y. Jia, Y. Wu, S. T. Nguyen, and R. S. Ruoff. Synthesis of graphene-based nanosheets via chemical reduction of exfoliated graphite oxide. Carbon. 45 (2007) 1558.

[121] R. H. Crabtree. The organometallic chemistry of transition metals. Wiley-Interscience. New Jersey, 2005.

[122] H. U. Blaser, A. Indolese, and A. Schnyder. Applied homogeneous catalysis by organometallic complexes. Current Science. 78 (2000) 1336.

[123] K. L. Hass, and K. J. Franz. Application of metal coordination chemistry to explore and manipulate cell biology. Chemical Reviews. 109 (2009) 4921.

[124] S. M. Hubig, S. V. Lindeman, and J. K. Kochi. Charge-transfer bonding in metal-arene coordination. Coordination Chemistry Reviews. 200-202 (2000) 831.

[125] K. Oldenburg and A. Vogler. Photoredox chemistry of bismuth trichloride in benzene. Journal of Organometallic Chemistry. 515 (1996) 245.

[126] S. Alaa and A. E. Aziz. Monomers, oligomers and polymers containing arenes with pendent transition metal moieties. Coordination Chemistry Reviews. 233-234 (2002) 177.

[127] S. Sarkar, E. Bekyarova, and R. C. Haddon. Organometallic Chemistry of Carbon Nanotubes and Graphene in Carbon Nanotubes and Graphene (Second Edition). Chapter 9. Organometallic chemistry of carbon nanotubes and graphene. Elsevier. Netherlands, 2014.

[128] X. Tian, S. Sarkar, M. L. Moser, F. Wang, A. Pekker, E. Bekyarova, M. E. Itkis, and R. C. Haddon. Effect of group 6 transition metal coordination on the conductivity of graphite nanoplatelets. Materials Letters. 80 (2012) 171.

[129] L. J. Brennan, and Y. K. Gun´ko. Advances in the organometallic chemistry of carbon nanomaterials. Organometallics. 34 (2015) 2086.

[130] E. Bekyarova. S. Sarkar, S. Niyogi, M.E. Itkis, and R. C. Haddon. Advances in the chemical modification of epitaxial graphene. Journal of Physics D: Applied Physics. 45 (2012) 154009.

[131] L. Cui, J. Yu, X. Yu, Y. Lv, G. Li and S. Zhou. *In situ* synthesis of polyisoprene/grafted single-walled carbon nanotube composites. Polymer Journal. 45 (2013) 834.

[132] H. M. Huang, H. C. Tsai, I. C. Liu and R. C. Tsiang. Synthesis of polystyrene-grafted carbon nanotubes. Journal of Material Research. 22 (2007) 132.

[133] W. A. Herrmann. Synthetic methods of organometallic and inorganic chemistry. Volume 7: Transition metals Part 1. Georg Thieme Verlag Stuttgat. New York, 1997.

[134] M. Bochmann. Organometallics 1. Complexes with transition metal-carbon σ-bonds. Oxford Science Publications. New York, 1994.

[135] U. Radius, F. M. Bickelhaupt, A. W. Ehlers, N. Goldberg, and R. Hoffmann. Is CO a special ligand in organometallic chemistry? Theoretical investigation of AB, $Fe(CO)_4AB$ and $Fe(AB)_5$ (AB = N_2, CO, BF, SiO). Inorganic Chemistry. 37 (1998) 1080.

[136] S. Sarkar, S. Niyogi, E. Bekyarova and R. C. Haddon. Organometallic chemistry of extended periodic π-electron systems: hexahapto-chromium complexes of graphene and single-walled carbon nanotubes. Chemical Science. 2 (2011) 1326.

[137] S. Sarkar, M. L. Moser, X. Tian, X. Zhang, Y. F. Al-Hadeethi, and R. C Haddon. Metals on graphene and carbon nanotubes surfaces: From mobile atoms to atomtronics to bulk metals to clusters and catalysts. Chemistry of Materials. 26 (2014) 184.

[138] A. A. Siller-Ceniceros, M. E. Sánchez-Castro, D. Morales-Acosta, J. R. Torres-Lubián, E. Martínez, F. J. Rodríguez-Varela. Innovative functionalization of Vulcan XC-72 with Ru organometallic complex: Significant enhancement in catalytic activity of Pt/C electrocatalyst for the methanol oxidation reaction (MOR). Applied Catalysis B: Environmental. 209 (2017) 455.

Chapter III

Hypothesis

$NiTiO_3$ and $CoTiO_3$ as co-catalysts will enhance the catalytic activity of Pt/C and Pt/rGO for the ORR in alkaline media. Additionally, the use of rGO as support will promote a high performance of the Pt-$NiTiO_3$ and Pt-$CoTiO_3$ catalysts for the ORR. With the same purpose, chromium organometallic compounds as functionalizing agents will be able to coordinate to an individual benzoic ring of the rGO structure forming hexahapto (η^6) bonds preserving the graphitic structure of rGO. The organometallic functionalities will also act as reactive sites for anchoring Pt nanoparticles and promoting the ORR.

Chapter IV

Objectives

General objective:

To demonstrate the enhanced performance of the Pt-$NiTiO_3$ and Pt-$CoTiO_3$ catalysts supported on Vulcan XC-72, rGO and rGO functionalized with chromium organometallic compounds for the ORR in alkaline media, compared to the monometallic Pt/C catalyst.

Specific objectives:

4.1 To show the feasibility of synthesizing nanostructured Pt-$NiTiO_3$ and Pt-$CoTiO_3$ catalysts supported on Vulcan XC-72, rGO and functionalized rGO by the microwave-assisted polyol method.

4.2 To demonstrate that the functionalization of rGO with chromium organometallic compounds have no negative effect on their graphitized lattice.

4.3 To show the positive effect of using $NiTiO_3$ and $CoTiO_3$ as co-catalyst of Pt to enhance the mass and specific activity of the nanostructured catalysts for the ORR in alkaline media, on the different carbonaceous supports.

4.4 To determine the tolerance of the nanostructured catalysts to the presence of methanol and ethanol during the ORR.

Chapter V

Materials and methods

5.1 Reagents and gases.

Chemicals of analytical grade were used as acquired without any further purification or pretreatment: Nickel acetate ($Ni(OCOCH_3)_2 \cdot 4H_2O$), cobalt chloride ($CoCl_2 \cdot 6H_2O$), titanium isopropoxide ($Ti[OCH(CH_3)_2]_4$), citric acid ($C_6H_8O_7$), chromium hexacarbonyl ($Cr(CO)_6$), benzene-chromium tricarbonyl ($(\eta^6\text{-}C_6H_6)Cr(CO)_3$), anhydrous tetrahydrofuran (THF, C_4H_8O), dibutyl ether ($C_8H_{18}O$), chloroplatinic acid hexahydrate ($H_2PtCl_6 \cdot 6H_2O$), ethylene glycol (EG, $C_2H_6O_2$), sodium hydroxide (NaOH), sulfuric acid (H_2SO_4), 2-propanol (C_3H_8O), 5% wt. Nafion® solution, potassium hydroxide (KOH), methanol (CH_3OH) and ethanol (CH_3CH_2OH) were acquired from Sigma-Aldrich. UHP (Ultra High Purity) N_2 and O_2 from Infra (purity ≥ 99.999%). Carbon Vulcan XC-72 (C) was obtained from Cabot Corp. Commercial reduced graphene oxide (rGO) was purchased from IDnano.

5.2 Physicochemical characterization.

XRD analysis was performed in a Phillips X´Pert (PANanalytical) apparatus with a Ni-filtered Cu Kα radiation. Diffraction patterns were collected in the 2θ range 10° to 80° for the $MTiO_3$ powders and from 10° to 100° (2θ) for the Pt-based electrocatalysts. The data were collected with a step of 0.02° (2θ) at room temperature. The crystalline phase identification of the materials was determined by comparing the experimental X-ray patterns with data compiled by the JCPDS. The crystallite size (*d*) was calculated from the peak widths using the Scherrer equation (Equation 5.1).[1,2]

$$d_{hkl} = \frac{k\,\lambda}{\beta\,cos\theta} \qquad (5.1)$$

where d_{hkl} is the crystallite size of nanoparticles, *hkl* are the Miller index of the planes being analyzed, *k* is a numerical factor referred to as the crystallite-shape factor normally taken as 0.9, λ is the wavelength of the X-ray Cu Kα source (1.5418 Å), β is the full width at half maximum of the diffracted peak in radians and θ is the Bragg diffraction angle.

The interplanar distance (*D*) of Pt was calculated from the (311) reflection via the Bragg law (Equation 5.2). Subsequently, the lattice parameter (*a*) for a cubic structure was estimated with the Equation 5.3.[3,4]

$$D_{hlk(311)} = \frac{\lambda}{2\sin\theta} \qquad (5.2)$$

$$a = D_{hlk\,(311)}\sqrt{h^2 + k^2 + l^2} \qquad (5.3)$$

Raman analysis was carried out in a Xplora microscope from Horiba Scientific with an excitation wavelength of 532 nm (2.33 eV). FTIR spectra were obtained using a Perkin Elmer Spectrum Frontier spectrometer with a diffuse reflectance attachment.

SEM images and chemical composition analysis by EDS were obtained in a Phillips XL30 SEM apparatus having a accelerate voltage of 20 kV. The sample powders were mounted over a copper tape adhered to a stainless steel holder. TEM and HR-TEM images were acquired in a JEOL 2100 microscope operating at 200 kV. Samples were prepared by ultrasonically dispersing the powders in 2-propanol. A drop of the suspension was deposited onto a carbon-coated copper grid and then dried in air.

Surface chemical composition analysis was performed by the XPS technique in a Thermo Scientific Escalab 250 Xi equipment. A monochromatic Al Kα source (*hv* = 1486.86 eV) was used as incident radiation. High resolution XPS spectra were collected at 300 W with a pass energy of 20 eV and a beam size of 400 μm diameter. XPS data was deconvoluted with the AAnalyzer software. Binding energies (BE) were referenced to the C 1s line set at 284.8 eV.

5.3 Synthesis of $NiTiO_3$ and $CoTiO_3$.

$NiTiO_3$ and $CoTiO_3$ nanoparticles were obtained by a wet-chemical procedure. Stoichiometric amounts of nickel acetate (or cobalt chloride) and titanium isopropoxide were separately dissolved in methanol, maintaining an M:Ti cationic ratio = 1:1. Citric acid was added to the titanium solution under magnetic stirring until a transparent phase was achieved. Then, the nickel (or cobalt) solution was added to the titanium mixture. The resulting solution containing Ni-Ti (or Co-Ti) precursors was heated at 90°C for 12 h in order to evaporate the solvent and promote the formation of a metal-citrate complex. The precursors were calcined for 3 h in air atmosphere at 700°C for $NiTiO_3$ and 900°C for $CoTiO_3$. After cooling down to room temperature, $NiTiO_3$ and $CoTiO_3$ nanoparticles were recovered.[5]

5.4 Organometallic functionalization of rGO with $Cr(CO)_6$ and $(\eta^6\text{-}C_6H_6)Cr(CO)_6$.

5.4.1 Reaction of rGO with $Cr(CO)_6$.

Two rGO:$Cr(CO)_6$ have been studied. 20 mg of RGO were dispersed in a THF/dibuthyl ether mixture. Then, a) 47.8 mg (0.22) and b) 8.2 mg (0.04 mmol) of $Cr(CO)_6$ were added separately to the rGO dispersion. The suspensions were maintained in the absence of light under argon atmosphere and refluxed

at 95°C under magnetic stirring for 48 h. The reaction mixtures were filtered and the products were washed several times with anhydrous ether. Finally, the black powders were dried under vacuum and preserved in dark containers under inert conditions.[6]

5.4.2 Reaction of rGO with $[(\eta^6\text{-}C_6H_6)Cr(CO)_6]$.

rGO was functionalized using 36 mg (0.17 mmol) of $[(\eta^6\text{-}C_6H_6)Cr(CO)_6]$ under the same conditions indicated in Section 5.4.1.

5.5 Synthesis of Pt-$MTiO_3$ (M = Ni, Co) catalysts supported on Vulcan XC-72 (C), rGO and functionalized rGO.

The 20% Pt-$MTiO_3$ supported on Vulcan, rGO and functionalized rGO catalysts with Pt:$MTiO_3$ nominal ratio 1:1 (at. %) were synthesized by the microwave assisted polyol method. $H_2PtCl_6 \cdot H_2O$, $MTiO_3$ and carbon support were separately dispersed in ethylene glycol for 30 min. Then, a solution of NaOH (dissolved in EG) was added to adjust the pH to 11. The solutions were heated under magnetic stirring in a modified domestic microwave (600 W) by 4 cycles of pulses of 1 minute-on/1-minute off of microwave irradiation and after cooling down to room temperature, H_2SO_4 in EG was used to adjust the pH to 2, maintaining stirring for 1 h. The products were then filtered and dried in a dessiccator overnight. A 20% Pt/C and Pt/rGO electrocatalysts were synthesized under the same on/off pulses of microwave irradiation and pH variation for comparison purposes, only avoiding the addition of the titanate solution.

5.6 Electrochemical set-up.

5.6.1 Electrode preparation.

The catalytic ink of each electrocatalyst was prepared by the following procedure. 10 mg of the powder material were mixed by ultrasound for 30 min with 1 mL of 2-propanol and 5 µL of Nafion solution. To form the working electrode, an aliquot of 10 µL of the catalytic ink were dispersed in a glassy carbon electrode (0.196 cm^2 geometric area) which is placed in a rotating disc setup (0.02 mg_{Pt} in a 20% Pt/C). The catalyst layer deposition was performed by drop evaporation, forming a homogeneous film over the glassy carbon electrode.

5.6.2 ORR studies.

Catalytic activity measurements were carried out in an electrochemical three-electrode cell using a potensiostat (from Pine Inst.). A Pt coiled wire was used as the counter electrode, with an Ag/AgCl (sat. KCl) employed as the reference electrode. Attention was paid to avoid any electrolyte anion contamination, placing it in a separate reservoir with a salt bridge that ended up in a Luggin capillary closed to the working electrode. All the potentials have been reported in this work with respect to the RHE, using the Nernst equation (Equation 5.4):[7]

$$E_{RHE} = E_{Ag/AgCl} + 0.059\,pH + E^{\circ}_{Ag/AgCl} \qquad (5.4)$$

where E_{RHE} is the potential converted with respect to RHE, $E_{Ag/AgCl}$ is the potential measured against the Ag/AgCl reference electrode in the experiments, the pH of the 0.5 M KOH electrolyte is 13.69, $E^{\circ}_{Ag/AgCl}$ is 0.197 V (i.e., the potential of the reference electrode used in the experiments). CVs were obtained in N_2-satured 0.5 M KOH, in the 0.05 to 1.2 V/RHE range at a scan rate of 20 mV s^{-1}.

The electrochemical surface area (ECSA, in $m^2\ g^{-1}$) is an important parameter for evaluating the number of electrochemically active sites per gram of the catalyst and is a parameter that gives an insight of the Pt active sites participation during the potential scan. ECSA values were calculated according the following equation (Equation 5.5):[8-10]

$$ECSA\ (m^2\ g^{-1}) = \frac{Q_H}{Q_{ref}\ L_{Pt}} \qquad (5.5)$$

where Q_H (in μC) is the charge in the H_{des} region after double layer correction in the CVs, Q_{ref} is the theoretical charge needed for the oxidation of a monolayer of hydrogen on smooth Pt, taking here as 210 μC cm^{-2} and L_{Pt} is the Pt loading (in g) in the working electrode confirmed by the elemental EDS analysis.

To evaluate the catalytic activity of the synthesized electrocatalysts for the ORR, the cell environment was saturated with oxygen atmosphere (bubbling oxygen at least 20 min). Then, the ORR polarization curves were obtained at different rotation rates (400, 800, 1200, 1600 and 2000 rpm) at the scan rate of 5 mV s^{-1} from 0.5 V to 1.2 V (vs. RHE). In addition, CV curve in N_2-satured electrolyte at a scan rate of 5 mV s^{-1} at 2000 rpm was obtained in order to eliminate any contributions of capacitive current. Figure 5.1 is presented as an example of the CVs obtained from the Pt/C catalyst. This background current was substracted from the experimental ORR current densities.

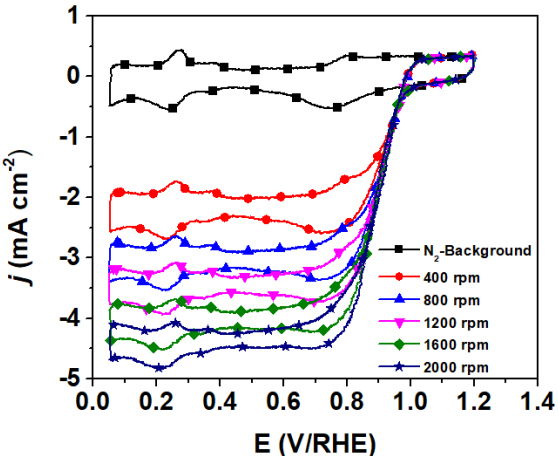

Figure 5.1 CVs of Pt/C in N_2 and O_2-satured electrolyte (0.5 M KOH) before background current subtraction. Scan rate: 5 mV s^{-1}.

The tolerance behavior of the catalysts was studied obtaining polarization curves at 2000 rpm adding CH_3OH and CH_3CH_2OH in a concentration of 0.1 y 0.5 M under O_2 atmosphere.

The ORR kinetic parameters were calculated on the basis of the mass-transport correction Koutecky-Levich equation (Equation 5.6) where the disk current density (j) correlates with the kinetic (j_k) and the diffusion limited (j_d) current densities as follows:[11-13]

$$\frac{1}{j} = \frac{1}{j_k} + \frac{1}{j_d} = \frac{1}{j_k} + \frac{1}{B\,\omega^{1/2}} \qquad (5.6)$$

Koutecky-Levich plot ($1/j$ vs. $\omega^{-1/2}$) was constructed to determinate the value of the slope B and via the Levich equation (Equation 5.7) calculate the transferred electron number (n) per oxygen molecule involved in the ORR process.[13,14]

$$n = \frac{B}{0.2FD^{2/3}v^{-1/6}C_{O_2}} \qquad (5.7)$$

Here, the constant 0.2 applies when ω is expressed in rpm, *F* is the Faraday constant (96 485 C mol^{-1}), *D* is the diffusion coefficient O_2 in the electrolyte (1.9 x 10^{-5} cm^2 s^{-1}), *v* is the kinematic viscosity of the electrolyte (1 x 10^{-2} cm^2 s^{-1}), and C_{O_2} is the concentration of the molecular oxygen in 0.5 mol L^{-1} KOH solution at 25 °C (1.2 x 10^{-6} mol cm^{-3}).

The kinetic current was calculated from the ORR polarization curves using the following Koutecky-Levich relation (Equation 5.8):[13]

$$i_k = \frac{i_d i}{i_d - i} \qquad (5.8)$$

where i_k is the mass-transport kinetic current, i_d is the diffusion-limited current and *i* is the experimental current collected at the working electrode.

Mass and specific activities were calculated by normalizing the kinetic current i_k with respect to the Pt load (mg_{Pt}, based in the EDS results) deposited in the glassy carbon electrode and with the Pt real surface area (A_{Pt} in cm^2), respectively, obtained from the following relationship (Equation 5.9):[10]

$$A_{Pt} = \frac{Q_H}{Q_{ref}} \qquad (5.9)$$

Q_H and Q_{ref} are described in equation 5.5.

5.7 References.

[1] U. Holzwarth, and N. Gibson. The Scherrer equation versus the ¨Debye-Scherrer equation". Nature Nanotechnology. 6 (2011) 534.

[2] R. Sharma, D. P. Bisen, U. Shukla, and B. G. Sharma. X-ray diffraction: A powerful method of characterizing nanomaterials. Recent Research in Science and Technology. 4 (2012) 77.

[3] Y. Kim, H. W. Kim, S. Lee, J. Han, D. Lee, J. R. Kim, C. U. Kim, S. Y. Jeong, H. J. Chae, B. S. Kim, H. Chang, W. B. Kim, S. M. Choi, and H. J. Kim. The role of ruthenium on carbon-supported PtRu catalysts for electrocatalytic glycerol oxidation under acidic conditions. ChemCatChem. 9 (2017) 1683.

[4] Y. Holade, C. Morais, K. Servat, T. W. Napporn, and K. B. Kokoh. Enhancing the available specific surface area of carbon supports to boost the electroactivity of nanostructured Pt catalysts. Physical Chemistry Chemical Physics. 16 (2014) 25609.

[5] R. Vijayalakshmi, and V. Rajendran. Effect of reaction temperature on size and optical properties of $NiTiO_3$ nanoparticles. E-Journal Chemistry. 9 (2012) 282.

[6] S. Sarkar, S. Niyogi, E. Bekyarova, and R. C. Haddon. Organometallic chemistry of extended periodic π-electron systems: hexahapto-chromium complexes of graphene and single-walled carbon nanotubes. Chemical Science. 2 (2011) 1326.

[7] X. Ge, A. Sumboja, D. Wuu, T. An. B. Li, F. W. T. Goh, T. S. A. Hor, Y. Zong, and Z. Liu. Oxygen reduction in alkaline media: From mechanisms to recent advances. ACS Catalysis. 5 (2015) 4643.

[8] B. P. Vinayan, R. I. Jafri, R. Nagar, N. Rajalakshmi, K. Sethupathi, and S. Ramaprabhu. Catalytic activity of platinum-cobalt alloy nanoparticles decorated functionalized multiwalled carbon nanotubes for oxygen reduction reaction in PEMFC. International Journal of Hydrogen Energy. 37 (2012) 412.

[9] M. L. Gorzny, A. S. Walton, and S. D. Evans. Synthesis of high-surface-area platinum nanotubes using a viral template. Advanced Functional Materials. 20 (2010) 1295.

[10] Y. Garsany. Experimental methods for quantifying the activity of platinum electrocatalysts for the oxygen reduction reaction. Analytical Chemistry. 82 (2010) 6321.

[11] S. Duron, R. Rivera-Noriega, P. Nkeng, G. Poillerat, and O. Solorza-Feria. Kinetik study of oxygen reduction on nanoparticles of ruthenium synthesized by pyrolysis of $Ru_3(CO)_{12}$. Journal of Electroanalytical Chemistry. 566 (2004) 281.

[12] D. Morales-Acosta, D. López de la Fuente, L. G. Arriaga, G. Vargas Gutiérrez, and F. J. Rodríguez Varela. Electrochemical investigation of Pt-Co/MWCNT as an alcohol-tolerant ORR catalyst for direct oxidation fuel cells. International Journal of Electrochemical Science. 6 (2011) 1835.

[13] U. A. Paulus, T. J. Schmidt, H. A. Gasteiger, and R. J. Behm. Oxygen reduction reaction on a high-surface area Pt/Vulcan carbon catalyst: A thin-film rotating ring-disk electrode study. Journal of Electroanalytical Chemistry. 495 (2001) 134.
[14] B. Jang, S. Bong, S. Woo, S. Park, J. Ha, E. Choi, and Y. Piao. Facile synthesis of one-dimensional iron-oxide/carbon hybrid nanostructures as electrocatalysts for oxygen reduction reaction in alkaline media. Journal of Nanoscience and Nanotechnology. 14 (2014) 8852.

Chapter VI

Enhanced electrocatalytic performance for the Oxygen Reduction Reaction on Pt-$MTiO_3$/C (M = Ni, Co) catalysts

6.1 Physicochemical characterization of $NiTiO_3$ and $CoTiO_3$ nanoparticles.

6.1.1 X-Ray diffraction analysis (XRD).

The XRD patterns of $NiTiO_3$ and $CoTiO_3$ nanoparticles (Figure 6.1) display narrow and intense peaks revealing the high crystallinity of rhombohedral pure phases. The patterns match with cards 083-0198 and 077-1373, respectively, of the JCPDS database.[1-5] XRD is a useful technique for determining the crystallite size (*d*) of nanomaterials, by averaging the thickness of the crystals in a direction perpendicular to the *hkl* plane, with the aid of the well-known Scherrer formula (Equation 5.1 in experimental section).[6] From the patterns in Figure 6.1 the crystallite size of $NiTiO_3$ and $CoTiO_3$ are determined to be 26 and 42 nm, respectively (Table 6.1).

6.1.2 SEM/EDS characterization.

SEM micrographs in Figure 6.2 show that $NiTiO_3$ and $CoTiO_3$ nanoparticles are predominantly spherical in shape and with agglomerated regions. Table 6.1 shows the chemical composition of $NiTiO_3$ and $CoTiO_3$ deduced from EDS analysis. Both nanomaterials have similar content of their constituents. For example, the Ni and Ti concentration at $NiTiO_3$ are 38.29 and 31.24, while Co and Ti content at $CoTiO_3$ are 39.94 and 30.17 (wt. %, respectively). The Ni:Ti and Co:Ti ratios are 1:1 (at. %), the nominally expected value.

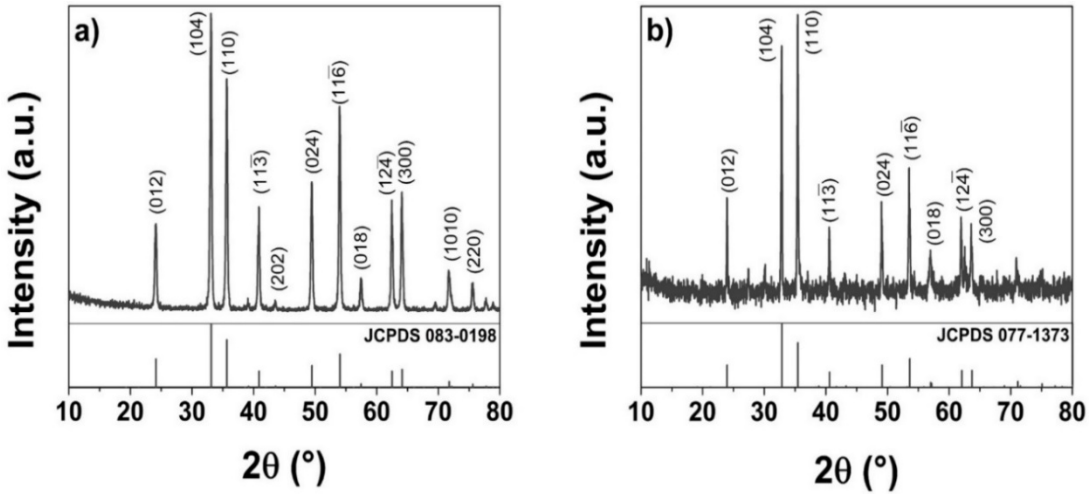

Figure 6.1 X-ray diffraction patterns of a) $NiTiO_3$ and b) $CoTiO_3$ nanoparticles.

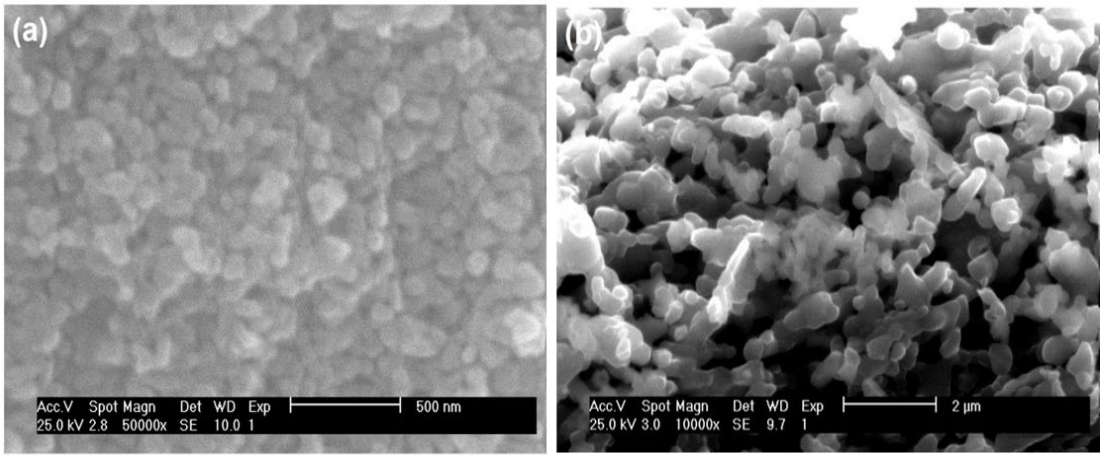

Figure 6.2 SEM images of a) $NiTiO_3$ and b) $CoTiO_3$ nanoparticles.

Table 6.1. Physical and chemical characteristics of $NiTiO_3$ and $CoTiO_3$.

	d_{XRD} (nm)	Particle size $_{TEM}$ (nm)	Chemical composition (wt. %)			M:Ti:O (at. %)
			M	Ti	O	
$NiTiO_3$	26	15-40	38.29 ± 1.52	31.53 ± 0.66	30.17 ± 1.16	1:1:2.9
$CoTiO_3$	42	19	39.94 ± 1.17	30.17 ± 1.49	29.87 ± 1.51	1:1:2.9

6.1.3 HR-TEM analysis.

The TEM image in Figure 6.3a shows the quasi-spherical morphology of the $NiTiO_3$ material. Its particle size has been determined to be in the 15-40 nm range. Figure 6.3b shows the HR-TEM micrograph of a $NiTiO_3$ nanoparticle having around 20 nm in diameter. The $NiTiO_3$ co-catalyst shows highly crystalline characteristics, as seen in the SAED pattern inserted, in good agreement with XRD results. Lattice fringes with an interplanar distance of 0.36 nm have been determined, which can be assigned to the (012) crystallographic plane of $NiTiO_3$. The particle size of $CoTiO_3$ obtained from HR-TEM micrograph in Figure 6.3c is 19 nm (Table 6.1).[7-9] Also, the SAED pattern of $CoTiO_3$ co-catalyst reveals its crystallinity, in good agreement with the XRD characterization. In this case, an interplanar of 0.33 nm has been obtained, assigned to the (012) plane of $CoTiO_3$.[9-11]

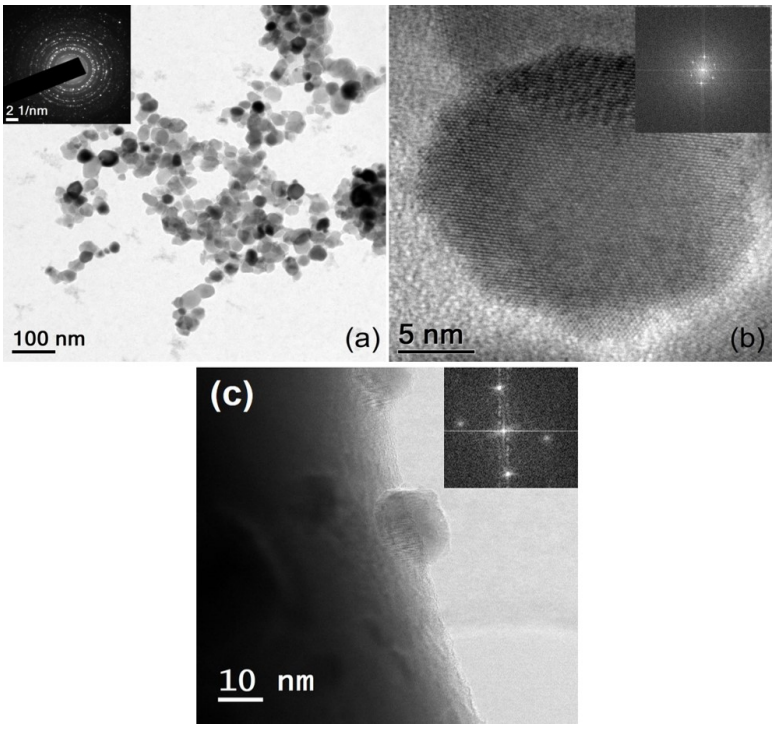

Figure 6.3. TEM and HR-TEM images of $NiTiO_3$ (a-b), HR-TEM of $CoTiO_3$ (c). SAED patterns from the nanoparticles are shown in the insets.

6.2 Physicochemical characterization of the Pt/C, Pt-$NiTiO_3$/C and Pt-$CoTiO_3$/C catalysts.

6.2.1 X-Ray diffraction analysis (XRD).

Figure 6.4a-c shows the diffraction patterns of the Pt/C, Pt-$NiTiO_3$/C and Pt-$CoTiO_3$/C catalysts. All diffractograms clearly show the characteristic features of face centered cubic (fcc) Pt. Reflections at ca. 2θ = 40, 67 and 81 can be ascribed to Pt (111), (220) and (311), respectively. The peaks located at around 25° (2θ) are due to the Vulcan support and are attributed to the graphite (002) plane. In the diffractogram of Pt-$NiTiO_3$/C, besides the Pt reflections, narrow peaks at 2θ around 33, 35, 49, 53, 62 and 64°, corresponding to the nickel titanate planes (104), (110), (024) (116), (214) and (300) are clearly detectable. Similarly, the pattern of Pt-$CoTiO_3$/C shows reflections at 2θ = 33 and 35° due to the (114) and (110) planes, respectively. Figure 6.4d depicts a zooming of the (311) reflections. No significant shift to higher or lower angles is observed when comparing the peaks of Pt-$NiTiO_3$/C, Pt-$CoTiO_3$/C and Pt/C, as reported elsewhere for Pt-metal oxide catalysts.[12-14]

This structural characteristic may be related to the fact that the Pt precursor is reduced to metallic nanoparticles in the presence of already formed $NiTiO_3$ and $CoTiO_3$ particles. Nevertheless, the Pt lattice parameter (*a*) calculated from the (311) reflection (Equations 5.2 and 5.3 from experimental section) is slightly modified, from 0.391 nm of Pt/C to 0.396 nm of both Pt-$NiTiO_3$/C and Pt-$CoTiO_3$/C. (Table 6.2).

The data of the wide Pt (311) peak has been used to estimate the crystallite size of the catalysts using the Scherrer equation (5.1 in experimental section). This reflection is chosen in order to minimize the interference of the titanate peaks observed at the (220) reflection in Figure 6.4b-c. Sizes of 1.4, 1.7 nm

and 2.5 have been calculated for Pt/C, Pt-NiTiO$_3$/C and Pt-CoTiO$_3$/C, respectively (Table 6.2).

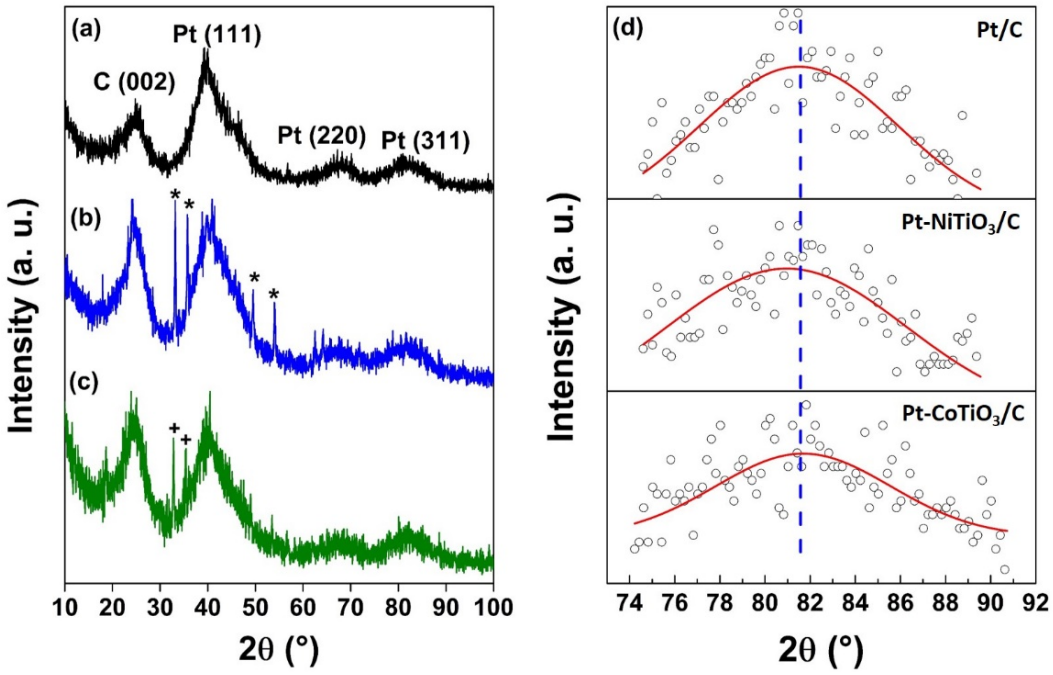

Figure 6.4 XRD patterns of a) Pt/C, b) Pt-NiTiO$_3$/C and c) Pt-CoTiO$_3$/C catalysts. Reflections of NiTiO$_3$ and CoTiO$_3$ marked with * and +, respectively, can be observed. d) Zoom-in of the (311) reflections of each catalyst.

Table 6.2. Physical and chemical characteristics of Pt/C, Pt-NiTiO$_3$/C and Pt-CoTiO$_3$/C catalysts

	a (nm)	d_{XRD} (nm)	Particle size $_{TEM}$ (nm)	Chemical composition (wt. %)			Pt:MTiO$_3$ (at. %)
				Pt	MTiO$_3$	C	
Pt/C	0.391	1.4	2.2	16.39 ± 0.83	-	83.61 ± 0.83	-
Pt-NiTiO$_3$/C	0.396	1.7	2.3	10.37 ± 0.68	8.65 ± 0.16	80.98 ± 0.69	0.95:1
Pt-CoTiO$_3$/C	0.396	2.5	1.8	8.56 ± 0.73	6.75 ± 0.27	84.71 ± 0.68	0.99:1

6.2.2 SEM/EDS characterization.

The results of the EDS analysis are shown in Table 6.2. The data is the average of the analyses over 5 different regions of the catalysts. The experimental chemical composition of Pt-$NiTiO_3$/C catalyst is very close to the expected from nominal calculations. The Pt:$NiTiO_3$ ratio was 0.95:1 (at. %) and the total catalyst content is roughly 20 wt%. Pt-$CoTiO_3$/C has a catalyst content of 15.36 (wt. %), with a Pt:$CoTiO_3$ ratio of 0.99:1, which approaches the expected value.

6.2.3 HR-TEM analysis.

The morphology and particle size distribution of Pt/C, Pt-$NiTiO_3$/C and Pt-$CoTiO_3$/C (Figures 6.5a-f) have been also analyzed by TEM and HR-TEM. The TEM images show the highly homogenous dispersion and nanosized characteristics of all Vulcan-supported electrocatalysts. The inset in HR-TEM image of the Pt/C catalyst (Figure 6.5d) is the SAED pattern corresponding to the region specified by the red square. A distance between lattice fringes of 0.22 nm, attributed to the Pt (111) plane, has been determined.[15] The SAED pattern in Figure 6.5b illustrates different rings of Pt-$NiTiO_3$/C (labeled 1 to 4) with interplanar distance of 0.39, 0.28, 0.22 and 0.18 nm, ascribed to the $NiTiO_3$ (012) and (104), and the Pt(111) and (200) planes, respectively.[1,15,16] Meanwhile, distances between planes of 0.39 and 0.22 nm ($NiTiO_3$ (012) and Pt (111) planes, respectively) have been calculated from the SAED patterns of the HR-TEM image, shown in the inset of Figure 6.5e, which corresponds to the areas highlighted by the red squares.

Figure 6.5f shows the HR-TEM image of Pt-$CoTiO_3$/C, with insets showing the SAED pattern of the regions highlighted by the red square. Distances between planes have been determined as 0.37 and 0.22 nm, ascribed to the $CoTiO_3$ (012) and Pt (111) planes, respectively. These analysis confirms that Pt, $NiTiO_3$ and $CoTiO_3$ nanoparticles are present in the corresponding catalyst. The

histograms of Pt/C, Pt-$NiTiO_3$/C and Pt-$CoTiO_3$/C (Figures 6.5g-i) show the narrow particle size distribution of the electrocatalysts. The average particle size of Pt/C is 2.2 nm, while that of Pt-$NiTiO_3$/C and Pt-$CoTiO_3$/C are 2.3 and 1.8 nm, respectively. These values are slightly different than those obtained from XRD calculations (see Table 6.2). However, it can be concluded that the two analyses indicate a very small particle size of the catalysts.

It is important to mention that the SAED patterns obtained from different areas of the HR-TEM images allowed to distinguish between Pt and $NiTiO_3$ (or $CoTiO_3$) nanoparticles, and this analysis gives evidence that some Pt nanoparticles may be dispersed on titanate sites.

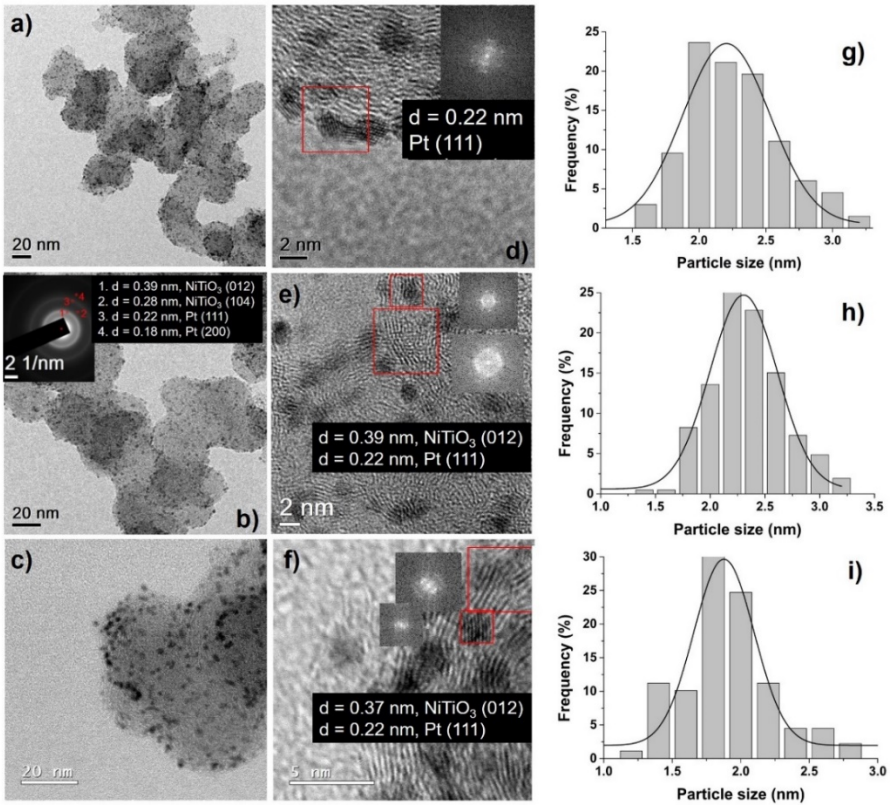

Figure 6.5 TEM and HR-TEM micrographs of Pt/C (a,d), Pt-$NiTiO_3$/C (b,e) and Pt-$CoTiO_3$/C (c,f). The insets are SAED patterns corresponding to the areas highlighted by red squares. The histograms of particle size distribution of the catalysts are shown in g), h) and i), respectively.

6.3 Catalytic activity of the Pt/C, Pt-$NiTiO_3$/C and Pt-$CoTiO_3$/C catalysts for the ORR.

6.3.1 ORR kinetics.

The CVs of Pt/C, Pt-$NiTiO_3$/C and Pt-$CoTiO_3$/C are shown in Figure 6.6. The curves in the full potential scan (Figure 6.6a) show the characteristic regions expected for Pt-based electrocatalysts, i.e., the hydrogen adsorption/desorption region ($H_{ads/des}$, 0.42 to 0.05 V/RHE and 0.05 to 0.47 V/RHE, respectively), double layer and Pt-oxides formation/reduction region (0.69 to 1.2 V/RHE and 1.2 to 0.47 V/RHE, respectively).

The Pt/C catalyst shows higher current densities than Pt-$NiTiO_3$/C and Pt-$CoTiO_3$/C. The peaks corresponding to the $H_{ads/des}$ region at the metaltitanate-containing catalysts are well defined indicating a high Pt participation during the potential scan, but the intensity observed is lower compared to the monometallic, which is more evident for Pt-$CoTiO_3$/C. The behavior of Pt-$NiTiO_3$/C and Pt-$CoTiO_3$/C indicates that there is no noticeable detrimental effect of the titanate on the $H_{ads/des}$ features of the cathode. Also, in the oxides region, which in alkaline media is mostly due to the specific adsorption of hydroxide anions,[17-20] the onset potential (E_{onset}) of Pt-OH formation in Pt/C, Pt-$NiTiO_3$/C and Pt-$CoTiO_3$/C are practically the same. A noticeable difference is that the typical peak at the beginning of the Pt-OH formation is more flat at Pt-$NiTiO_3$/C, and even more at Pt-$CoTiO_3$/C.

Figure 6.6b shows a comparison of the Pt-oxides reduction peaks. A very small shift of 3 mV to lower potentials is observed for the Pt-$NiTiO_3$/C (719 mV/RHE) compared to Pt/C (722 mV/RHE) at the peak maximum**.** In the case of Pt-$CoTiO_3$/C, this value is slightly displaced to higher potentials (732 mV/RHE). Therefore, it can be concluded that the adsorption strength of oxygen species on the Pt sites at the titanate-containing catalysts is roughly the same as that

in the monometallic. This means that the reduction of intermediates should proceed similarly on both catalysts.

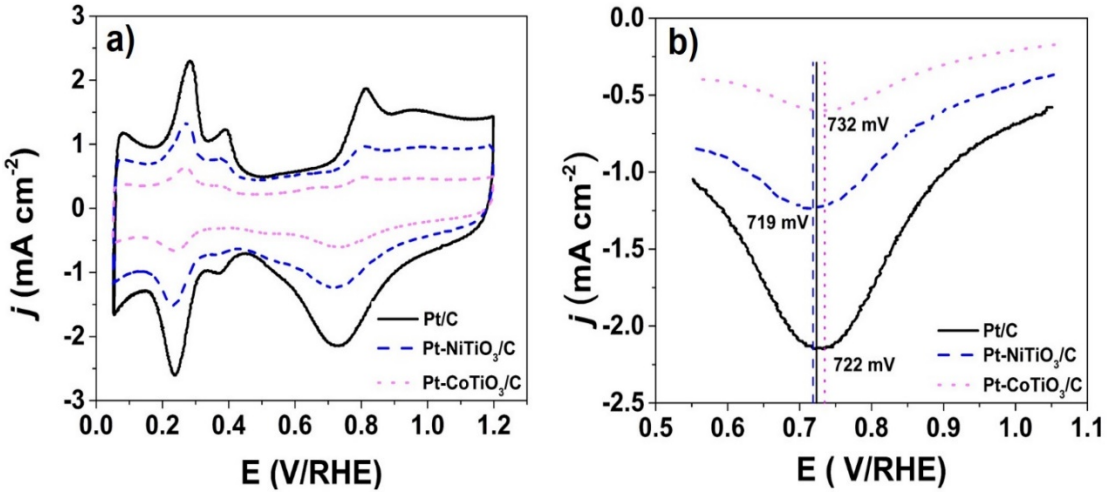

Figure 6.6 (a) CVs of Pt/C, Pt-NiTiO$_3$/C and Pt-CoTiO$_3$/C. Electrolyte: N_2-satured 0.5 M KOH. Scan rate: 20 mV s^{-1}. (b) Zooming of the Pt-oxide reduction peaks of Pt/C, Pt-NiTiO$_3$/C and Pt-CoTiO$_3$/C.

The polarization curves of the ORR at Pt/C, Pt-NiTiO$_3$/C and Pt-CoTiO$_3$/C (cathodic sweep) at rotation rates of 400, 800, 1200, 1600 and 2000 rpm are shown in Figures 6.7a-c, respectively. The curves have been built after background current subtraction (see Experimental section).

From the curves, the E_{onset} of the ORR at Pt/C (~1.03 V/RHE) is roughly the same as that of Pt-NiTiO$_3$/C (~1.04 V/RHE) and slightly higher than Pt-CoTiO$_3$/C (1.00 V/RHE) (Table 6.3). Meanwhile, the current density at 0.9 V/RHE and ω = 2000 rpm is −2.50 mA cm^{-2} for Pt/C, very close to the value of −2.10 mA cm^{-2} at Pt-NiTiO$_3$/C under the same conditions. For Pt-CoTiO$_3$/C was found to be -0.47 mA cm^{-2}. These results indicates that the Pt-NiTiO$_3$/C material has fundamentally the same catalytic activity for the ORR, compared to that of the monometallic cathode.

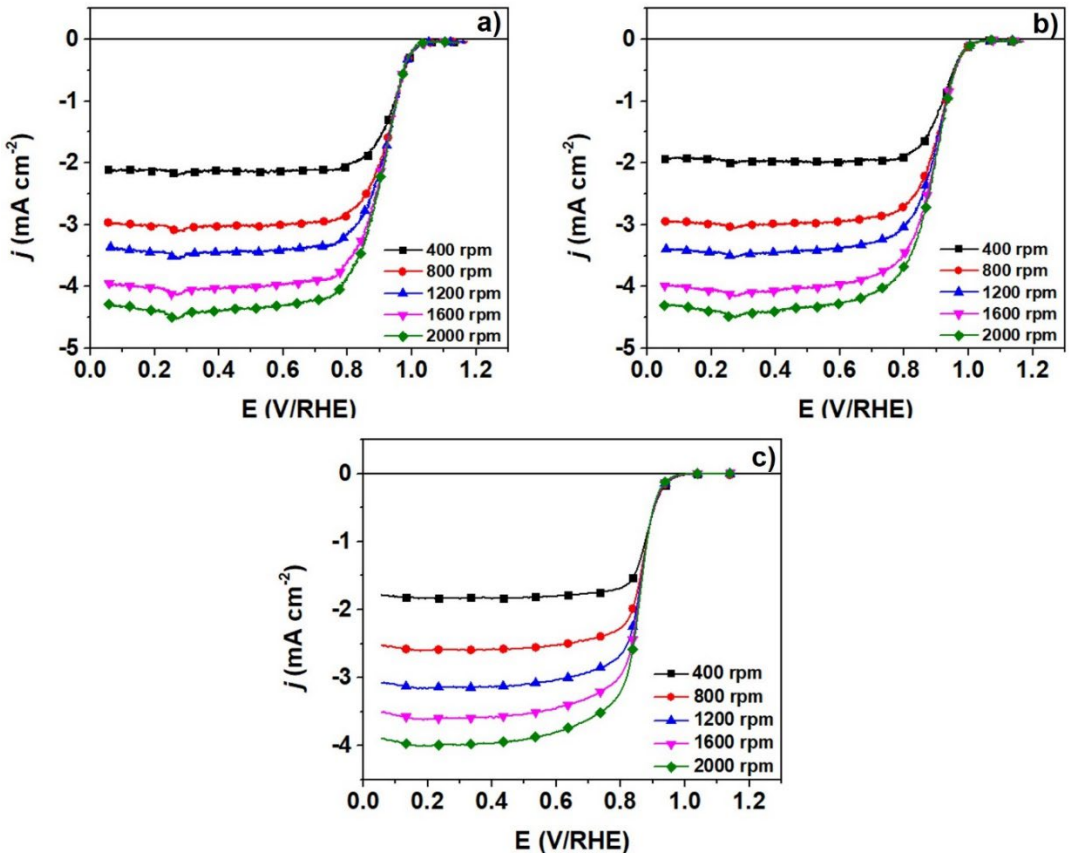

Figure 6.7 Polarization curves for the ORR on: a) Pt/C, b) Pt-NiTiO$_3$/C and c) Pt-CoTiO$_3$/C catalysts in O$_2$-satured 0.5 M KOH electrolyte. Scan rate: 5 mV s^{-1}.

Table 6.3 Electrochemical parameters at Pt/C, Pt-NiTiO$_3$/C and Pt-CoTiO$_3$/C.

Catalyst	E_{onset} (V)	$j_{0.9\ V/RHE}$ (mA cm^{-2})	Q_H (μC)	A_{Pt} (cm^2)	*b* at *lop* (mV dec^{-1})	*b* at *hop* (mV dec^{-1})
Pt/C	1.03	-2.50	2947.2	14.03	77	116
Pt-NiTiO$_3$/C	1.04	-2.10	1549.6	7.37	67	112
Pt-CoTiO$_3$/C	1.00	-0.47	650.4	3.09	56	122

It is well known that the Levich Equation applies when RDE measurements of the ORR are collected (equation 5.6 in Chapter V).[21-23] Nafion layer diffusion parameters have no effect in the behavior of the catalysts for the ORR curves

because the amount of Nafion used in this study is very small.[23] The measured ORR current densities in the mixed-controlled region (Figures 6.8a-c) can be expressed as a function of the rotation rate using equation 5.7.

Koutecky-Levich plots of Pt/C, Pt-$NiTiO_3$/C and Pt-$CoTiO_3$/C at different potentials are shown in Figures 6.8a-c, respectively. The plots show linearity and parallelism, indicating first-order kinetics with respect to O_2. [20,21,23] In all cases, the lines fall close to that corresponding to a theoretical $4e^-$ transfer slope, also included in Figure 6.8 and calculated from Equation 5.7. The slope of a $2e^-$ mechanism is shown for comparison too. From the experimental data, *n* has been calculated as 3.8 for Pt/C and Pt-$NiTiO_3$/C and 3.2 for Pt-$CoTiO_3$/C. This result suggests that the ORR at the novel home-developed catalysts may proceed via a $4e^-$ mechanism according to the reaction in alkaline media (Reaction 6.1):

$$O_2 + 2H_2O + 4e^- \rightarrow 4OH^- \qquad (6.1)$$

Mass and specific activity plots of the ORR at the catalysts are shown in Figure 6.10, calculated from the data of polarization curves (Figure 6.7) using the mass-transport correction expressed in the equation 5.8 (Chapter V). The mass activity curves in Figure 6.10a have been normalized with respect to the Pt mass content deposited in the thin porous electrodes taking into account the EDS results (Table 6.2). Meanwhile, the specific activity plots in Figure 6.10b have been built taking into account the Pt real surface area (A_{Pt}, in cm^2, equation 5.9 in Chapter V), calculated by measuring the charge in the H_{des} region (Q_H, in μC) after double layer correction in the CVs of Figure 6.6a. The calculated values of Q_H and A_{Pt} are shown in Table 6.3.

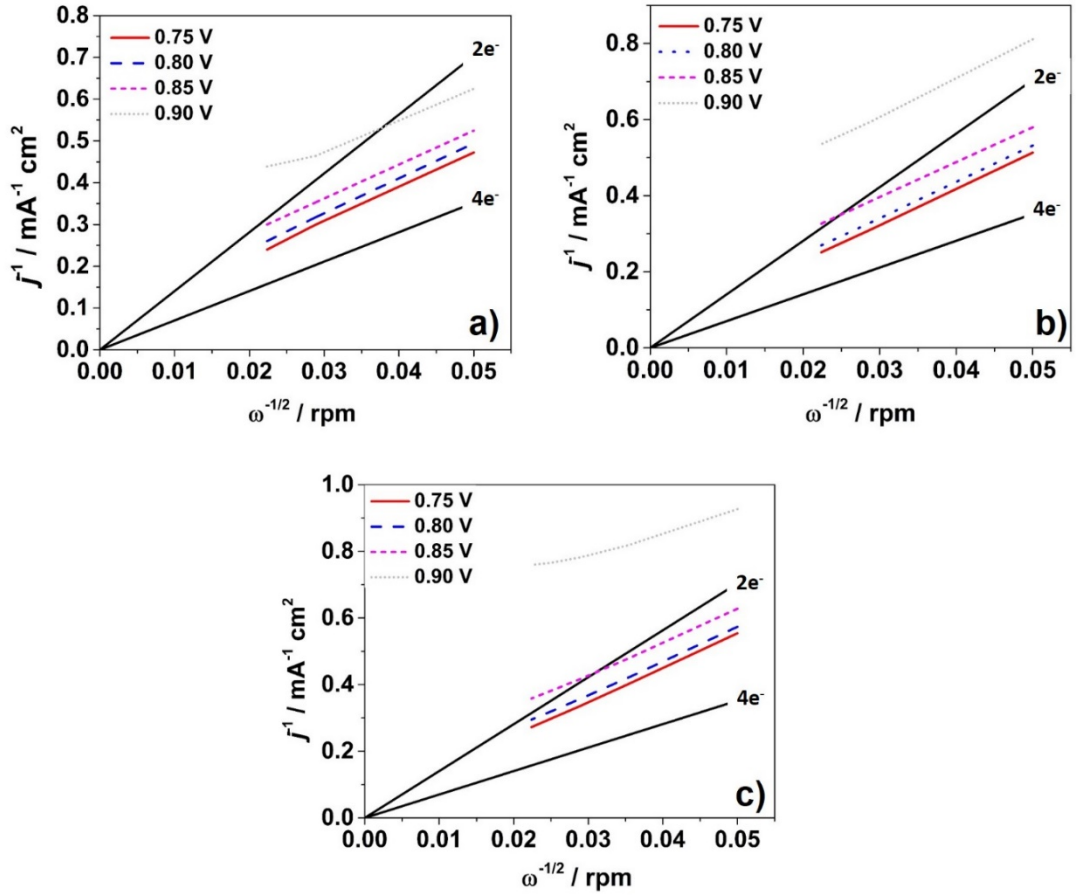

Figure 6.8 Koutecky-Levich plots of the ORR at different potentials on Pt/C (a), Pt-$NiTiO_3$/C (b) and Pt-$CoTiO_3$/C (c).

Two regions with distinct Tafel slopes (*b*) can be observed. The first one is at low overpotentials (*lop*), i.e., potentials between 0.95 and 0.85 V/RHE. At high overpotentials (*hop*), i.e. 0.85 V and lower, there is a change into higher slopes in good agreement with the behavior reported in several references, beginning with those of Damjanovic *et al.*[24-28] The change in Tafel slope is attributed to an effect of the adsorbed oxygen-containing species such as reaction intermediates from the ORR, or chemisorbed hydroxyl groups (OH_{ads}) from the electrolyte.[28] The smaller *b* at low overpotentials is associated to a Temkin adsorption mechanism at a higher coverage of O-like species, while the slope at high overpotentials is ascribed to a Langmuir adsorption due to the first

electron transfer of the reaction (rate determining step).[28,29] Tafel slopes of -60 and -120 mV dec^{-1} at low and high overpotentials, respectively, have been reported for the ORR in alkaline media.[26]

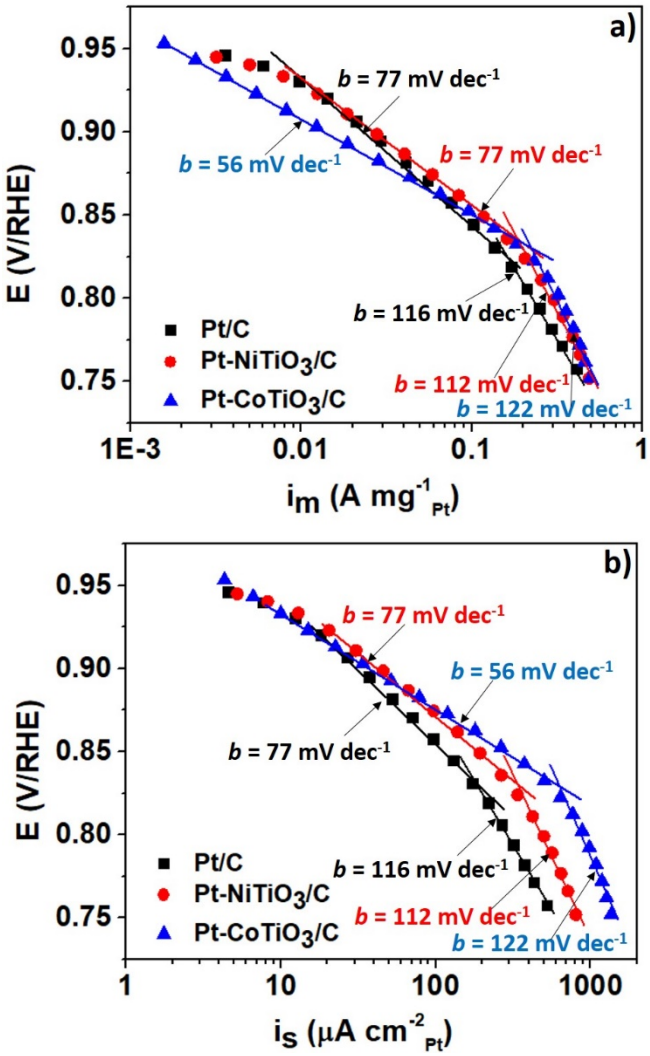

Figure 6.9 (a) Mass and (b) specific activity plots of the ORR on Pt/C, Pt-$NiTiO_3$/C and Pt-$CoTiO_3$/C catalysts. Electrolyte: O_2-satured 0.5 M KOH. ω = 2000 rpm.

The *b* values under Langmuir adsorption mechanism are 116, 112 and 122 mV dec^{-1} at the Pt/C, Pt-$NiTiO_3$/C and Pt-$CoTiO_3$/C catalysts, respectively, close

to 120 mV dec^{-1}. Meanwhile, the values of *b* at *lop* are 77, 67 and 56 mV dec^{-1} for Pt/C, Pt-$NiTiO_3$/C and Pt-$CoTiO_3$/C, respectively. These values are closer to the theoretical 60 mV dec^{-1}. However, particularly in the case of the monometallic, the slope is higher. The behavior of the catalysts may be related to the participation of the carbon support on the ORR, which has an important effect on the kinetics of the reaction as has been reported previously.[26,30] Overall, the approximation in Tafel slopes in Figures 6.9a and 6.9b indicates that the reaction mechanism of the ORR at Pt-$NiTiO_3$/C and Pt-$CoTiO_3$/C is the same as the mechanistic pathway on Pt/C in the KOH electrolyte.

However, it should be noticed that the mass catalytic activity of Pt-$NiTiO_3$/C and Pt-$CoTiO_3$/C surpasses that of Pt/C at potentials of ca. 0.91 and 0.86 V/RHE and below, respectively (Figure 6.9a). Likewise, the specific activity of Pt-$NiTiO_3$/C and Pt-$CoTiO_3$/C is higher at potentials of ca. 0.94 V/RHE and below compared to Pt/C in Figure 6.9b. At potentials more negative than 0.88 V/RHE, the specific activity of Pt-$CoTiO_3$/C surpasses that of Pt-$NiTiO_3$/C. These results suggests a positive effect of using the titanate as co-catalyst for the ORR in the alkaline electrolyte.

6.3.2 Tolerance tests.

It is well known that Pt/C cathodes become rapidly depolarized by the presence of organic molecules, with a decrease in catalytic activity for the ORR and therefore a negative impact in the efficiency of a fuel cell.[31] The loss of catalytic activity of Pt/C has been observed for a wide variety of liquid fuels such as methanol,[31,32] ethanol,[23] ethylene glycol,[23,33] and 2-propanol.[23] For example, the shift in potential with respect to E_{onset} towards more negative values (ΔE_{onset}) can be as high as 620 mV in the presence of 0.125 M ethylene glycol, when Pt/C is used in acid media.[21] A loss in performance of Pt/C has also been demonstrated in alkaline media in the presence of methanol.[34] Therefore, a key

feature of candidate catalysts to be used in A-DAFC cathodes is their selectivity toward the ORR and tolerance to organic substances.

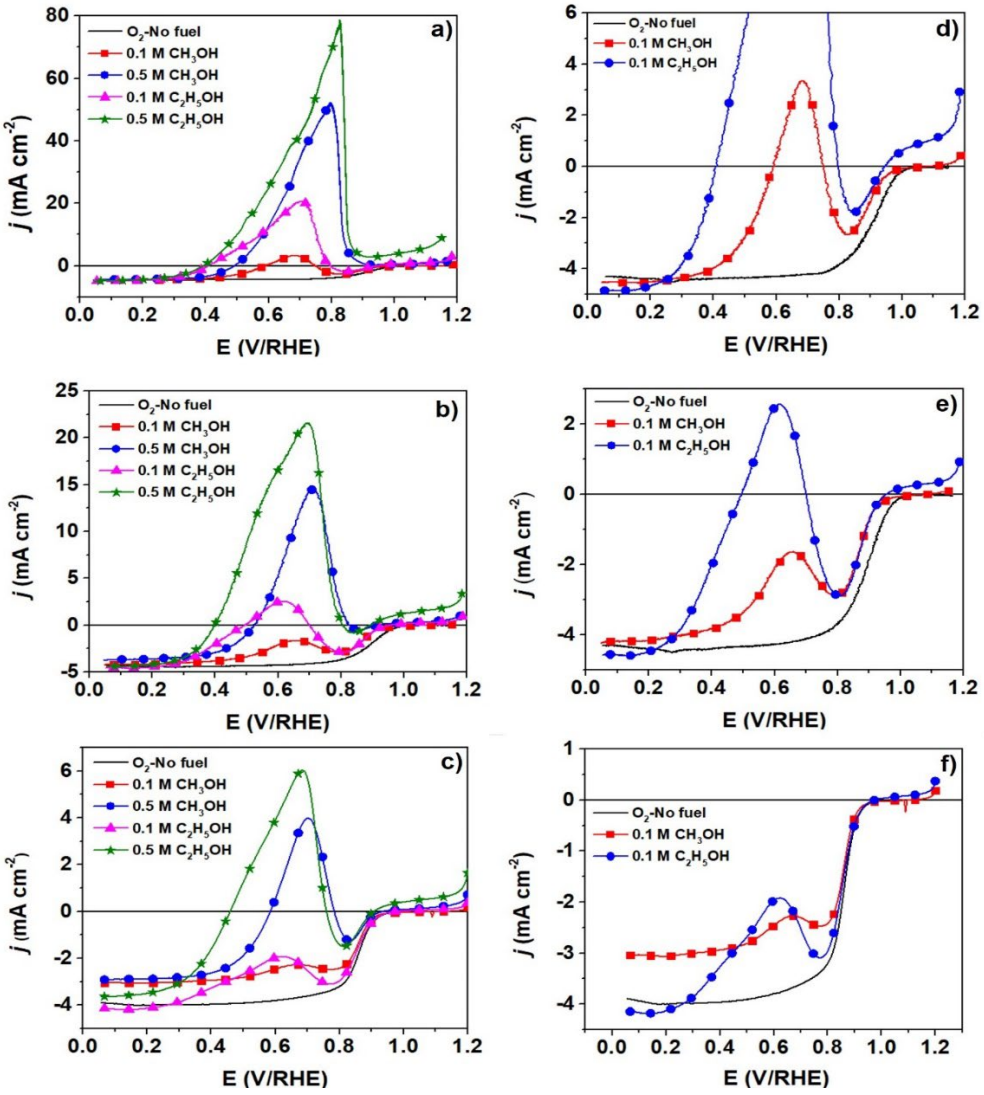

Figure 6.10 Polarization curves of the ORR at (a) Pt/C, (b) Pt-NiTiO$_3$/C and (c) Pt-CoTiO$_3$/C in the absence and presence of 0.5 and 0.1 M CH_3OH or C_2H_5OH. Figures (d-f) show the details with 0.1 M fuels. Electrolyte: 0.5 M KOH. Scan rate: 5 mV s^{-1}. ω = 2000 rpm.

Figure 6.10 shows the polarization curves of the ORR on Pt/C, Pt-$NiTiO_3$/C and Pt-$CoTiO_3$/C in the absence (with data from Figure 6.7, ω = 2000 rpm) and presence of 0.5 and 0.1 M CH_3OH or C_2H_5OH. At the higher concentration (Figures 6.10 a-c), all catalysts show a preference for the oxidation of both of the fuels, with Pt/C delivering higher peak current densities. At the low concentration, the Pt/C catalyst shows higher current densities associated to the oxidation of the molecules, with peak maximums due to the oxidation of 0.1 M CH_3OH and C_2H_5OH of 3.3 and 20.5 mA cm^{-2}, respectively. The corresponding values at Pt-$NiTiO_3$/C are –1.6 and 2.5 mA cm^{-2}, while those of Pt-$CoTiO_3$/C are -2.2 mA cm^{-2} and -1.9 mA $cm^{-2,}$ respectively (Table 6.4).

A zoom of the polarization curves, taking into account only the 0.1 M concentration of the fuels is shown for Pt/C, Pt-$NiTiO_3$/C and Pt-$CoTiO_3$/C in Figures 6.10d-f, respectively. The higher tolerance in terms of oxidation current densities of each of the fuels is more evident at Pt-$CoTiO_3$/C. Furthermore, the ΔE_{onset} values with CH_3OH and C_2H_5OH on Pt-$CoTiO_3$/C are 40 and 30 mV, respectively, smaller compared to Pt/C and Pt-$NiTiO_3$/C (Table 6.4). In summary, the behavior of the catalysts in Figure 6.10 indicates that the higher selectivity toward the ORR is obtained with Pt-$CoTiO_3$/C in the presence of both alcohols.

Table 6.4. Fuel oxidation current densities and ORR ΔE_{onset} on Pt/C, Pt-$NiTiO_3$/C and Pt-$CoTiO_3$/C in the presence of 0.1 and 0.5 M CH_3OH and C_2H_5OH.

	***j* (mA cm^{-2})**				**ΔE_{onset} (V/RHE) with 0.1 M fuel**	
	CH_3OH		**C_2H_5OH**		**CH_3OH**	**C_2H_5OH**
Catalyst	**0.1 M**	**0.5 M**	**0.1 M**	**0.5 M**		
Pt/C	3.3	52.7	20.5	78.3	60	90
Pt-$NiTiO_3$/C	-1.6	14.4	2.5	21.6	60	90
Pt-$CoTiO_3$/C	-2.2	3.9	-1.9	5.9	40	30

Even though a full tolerance to the organic molecules has not been reached, from the catalytic behavior in Figure 6.10, the presence of the titanate increases the catalyst's selectivity towards the oxygen reduction, over the oxidation of methanol and ethanol. Interestingly, one of the reasons of the enhanced selectivity of Pt-$NiTiO_3$/C and Pt-$CoTiO_3$/C (compared to Pt/C) toward the ORR can be due to a geometric effect. The presence of the titanate may inhibit the dissociative chemisorption of the organic fuels, which requires three neighboring Pt atoms to be activated while that of the oxygen requires only two adjacent Pt-sites.[32]

Moreover, it has been reported that by Goodenough *et al.* that at oxide materials, the ORR in alkaline media occurs by exchange of surface OH^-.[35] For $NiTiO_3$ and $CoTiO_3$ nanoparticles, the O-site present in the $NiTiO_{3-x}(OH)_x$ and $CoTiO_{3-x}(OH)_x$ phases may be functioning as the reaction sites for the ORR. Reaction 6.1 occurs by exchange of surface OH^- species present in the surface of $NiTiO_{3-x}(OH)_x \cdot H_2O$ or $CoTiO_{3-x}(OH)_x \cdot H_2O$.[36] This can explain why mass and specific activities of Pt-$NiTiO_3$/C and Pt-$CoTiO_3$/C are the same and at some potentials better than those of Pt/C. Also, the surface OH^- species may be a positive issue increasing the tolerance behavior of Pt-$NiTiO_3$/C and Pt-$CoTiO_3$/C for low concentration CH_3OH and C_2H_5OH. Another factor promoting the tolerance may be that O_2 is more strongly adsorbed than alcohols at Pt sites in Pt-$NiTiO_3$/C and Pt-$CoTiO_3$/C (due to the presence of the titanates), compared to the Pt-alone catalyst.

Even though this may not be the optimized chemical composition of Pt-$NiTiO_3$/C and Pt-$CoTiO_3$/C, their catalytic activity and enhanced selectivity for the ORR (especially in the case of Pt-$CoTiO_3$/C) make them potential cathodes materials for AEMFCs and A-DAFCs.

6.3.3 Stability of $NiTiO_3$ in acid media.

On the other hand, it is of interest to further evaluate the stability of the $NiTiO_3$ nanoparticles in order to discard any structural modification or leaching of Ni in the acid media. $NiTiO_3$ samples have been submitted to 500 cycles between 0.05 and 1.2 V/RHE, in 0.5 M H_2SO_4. Post-mortem TEM analysis has been carried out. Figure 6.12a shows a HR-TEM image of a $NiTiO_3$ nanoparticle after electrochemical cycling, with its SAED pattern shown in Figure 6.12b. It can be observed that the morphology and crystallinity are not significantly changed after electrochemical tests, compared to its characteristics in Figure 6.3b, i.e., before cycling.

EDS analysis shows that after electrochemical testing, $NiTiO_3$ preserves high Ni and Ti contents (35.64 and 47.78 wt %, respectively). Even though this result may not be conclusive, it suggests that leaching of Ni is not occurring, or at least not significantly. Table 6.4 shows a comparison of chemical composition of as-synthesized $NiTiO_3$ and after electrochemical cycling.

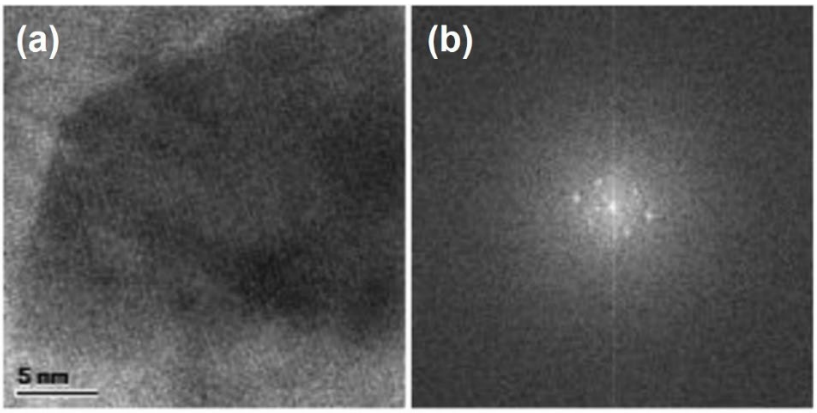

Figure 6.12 a) HR-TEM image of $NiTiO_3$ nanoparticles after electrochemical cycling (500 cycles between 50 and 1200 mV/RHE) in 0.5 M H_2SO_4. b) corresponding SAED pattern.

Table 6.4 Chemical composition of as-synthesized $NiTiO_3$

	Chemical composition (wt. %)		
$NiTiO_3$ sample	**Ni**	**Ti**	**O**
As-synthesized	31.53	38.29	30.17
After cycling	35.64	47.78	16.58
After acid treatment	32.08	33.03	34.89

Furthermore, in order to evaluate the effects of strong acid solution on the structural characteristics of the titanate, a $NiTiO_3$ sample has been soaked in 1 M H_2SO_4 for 24 h. Figure 6.13 shows the XRD pattern after acid treatment, demonstrating that there are not significant structural changes when compared with the pattern before treatment (Figure 6.1a). The relative intensity of the reflections is only slightly modified, while no shifts in the peaks maximum has been observed. Furthermore, the chemical composition of the sample after acid treatment is shown in Table 6.4. No major differences are observed with respect to the composition before soaking. Overall, the results suggest that nanostructured $NiTiO_3$ is stable in acid media.

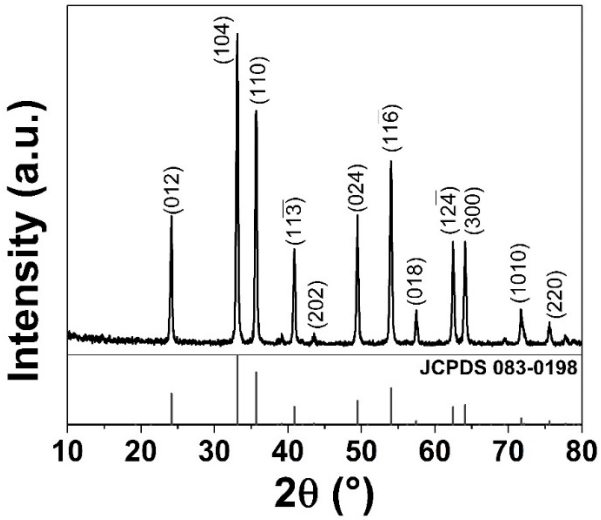

Figure 6.13 XRD pattern of $NiTiO_3$ after acid treatment in 1 M H_2SO_4 for 24 h.

6.4 References.

[1] T. D. Nguyen-Phan, C. Nguyen-Huy, and E. W. Shin. Morphological evolution of hierarchical nickel titanates by elevation of the solvothermal temperature. Materials Letter. 131 (2014) 217.

[2] W. Dong, Y. Zhu, H. Huang, L. Jiang, H. Zhu, C. Li, B. Chen, Z. Shi, and G. Wang. A performance study of enhancement visible-light-driven photocatalysts and magnetical protein separation of multifunctional yolk-shell nanostructures. Journal of Materials Chemistry A. 1 (2013) 10030.

[3] K. L. Lopes, L. S. Cavalcante, A. Z. Simoes, J. A. Varela, E. Longo, and E. R. Leite. $NiTiO_3$ powders obtained by polymeric precursor method: Synthesis and characterization. Journal of Alloys and Compounds. 468 (2009) 327.

[4] Y. Qu. W. Zhou, and H. Fu. Porous cobalt titanate nanorod: A new candidate for visible light-driven photocatalytic water oxidation. ChemCatChem. 6 (2014) 265.

[5] Y. J. Lin, Y. H. Chang, W. D. Yang, and B. S. Tsai. Synthesis and characterization of ilmenite $NiTiO_3$ and $CoTiO_3$ prepared by a modified Pechini method. Journal of Non-Crystalline Solids. 352 (2006) 789.

[6] R. Sharma. D. P. Bisen, U. Shukla, and B. G. Sharma. X-ray diffraction: A powerful method of characterizing nanomaterials. Recent Research in Science and Technology. 4 (2012) 77.

[7] V. Chellasamy, and P. Thangadurai. Structural and electrochemical investigations of nanostructured $NiTiO_3$ in acidic environment. Frontiers of Materials Science. 11 (2017) 162.

[8] J. Xu, W. Ding, W. Zhao, W. Zhao, Z. Hong, and F. Huang. In situ growth enabling ideal graphene encapsulation upon mesocrystalline $MTiO_3$ (M = Ni, Co, Fe) nanorods for stable lithium storage. ACS Energy Letters. 2 (2017) 659.

[9] Y. Qu, W. Zhou, L. Jiang, and H. Fu. Novel heterogeneous CdS nanoparticles/$NiTiO_3$ nanorods with enhanced visible-light-driven photocatalytic activity. RSC Advances. 3 (2013) 18305.

[10] J. Lu, Y. Jiang, Y. Zhang, J. Huang, and Z. Xu. Preparation of gas sensing $CoTiO_3$ nanocrystallites using EDTA as the chelating agent in a sol–gel process. Ceramics International. 41 (2015) 3714.

[11] Q. Wang, Q. Guo, L. Wang, and G. Li. The flux growth of single-crystalline $CoTiO_3$ polyhedral particles and improved visible-light photocatalytic activity of heterostructured $CoTiO_3$/g-C_3N_4 composites. Dalton Transactions. 45 (2016) 17748.

[12] C. Xu, P. K. Shen, and Y. Liu. Ethanol electrooxidation on Pt/C and Pd/C catalysts promoted with oxide. Journal of Power Sources. 164 (2007) 527.

[13] D. J. Guo, and Z. H. Jing. A novel co-precipitation method for preparation of Pt-CeO_2 composites on multi-walled carbon nanotubes for direct methanol fuel cells. Journal of Power Sources. 195 (2010) 3802.

[14] H. Song, X. Qiu, and F. Li. Effect of heat treatment on the performance of TiO_2-Pt/CNT catalysts for methanol electro-oxidation. Electrochimica Acta. 53 (2008) 3708.

[15] A. Altamirano-Gutierrez, A. M. Fernández, and F. J. Rodríguez-Varela. Preparation and characterization of Pt-CeO_2 and Pt-Pd electrocatalysts for the oxygen reduction reaction in the absence and presence of methanol in alkaline medium. International Journal of Hydrogen Energy. 38 (2013) 12657.

[16] M. Hinojosa-Reyes, V. Rodríguez-González, and R. Zanella. Gold nanoparticles supported on TiO2-Ni as catalysts for hydrogen purification via water-gas shift reaction. RSC Advances. 4 (2014) 4308.

[17] N. M. Mackovic, H. A. Gasteiger, and P. N. Ross. Oxygen reduction on platinum low-index single-crystal surfaces in alkaline solution: Rotating ring disk$_{Pt(hkl)}$ studies. The Journal of Physical Chemistry. 100 (1996) 6715.

[18] M. R. Tarasevich, A. Sadkowski, and E. Yeager, in Comprehensive Treatise of Electrochemistry, B. E. Conway, J. O M. Bockris, E. Yeager, S. U. M. Khan, and R. E. White. Editors, p. 301, Plenum Press, New York, 1983.

[19] N. Ramaswamy, and S. Mukerjee. Influence of inner- and outer-sphere electron transfer mechanisms during electrocatalysis of oxygen reduction in alkaline media. The Journal of Physical Chemistry C. 115 (2011) 18015.

[20] R. C. Sekol, X. Li, P. Cohen, G. Doubek, M. Carmo, and A. D. Taylos. Silver palladium core–shell electrocatalyst supported on MWNTs for ORR in alkaline media. Applied Catalysis B: Environmental. 138 (2013) 285.

[21] S. Durón, R. Rivera-Noriega, P. Nkeng, G. Polillerat, and O. Solorza-Feria. Kinetic study of oxygen reduction on nanoparticles of ruthenium synthesized by pyrolysis of $Ru_3(CO)_{12}$. Journal of Electroanalytical Chemistry. 566 (2004) 281.

[22] H. Meng, and P. K. Shen. Novel Pt-free catalyst for oxygen electroreduction. Electrochemical Communications. 8 (2006) 588.

[23] D. Morales-Acosta, D. López de la Fuente, L. G. Arriaga, G. Vargas Gutiérrez, and F. J. Rodríguez-Varela. Electrochemical investigation of Pt-Co/MWCNT as an alcohol-tolerant ORR catalyst for direct oxidation fuel cells. International Journal of Electrochemical Science. 6 (2011) 1835.

[24] A. Damjanovick, and V. Brusic. Electrode kinetics of oxygen reduction on oxide-free platinum electrodes. Electrochimica Acta. 12 (1967) 615.

[25] D. B. Sepa, M. V. Voinovic, and D. Damjanovick. Reaction intermediates as a controlling factor in the kinetics and mechanism of oxygen reduction at platinum electrodes. Electrochimica Acta. 26 (1981) 781.

[26] F. H. B. Lima, J. R. C. Salgado, E. R. González, and E. A. Ticianelli. Electrocatalytic properties of PtCo/C and PtNi/C alloys for the oxygen reduction reaction in alkaline solution. Journal of Electrochemical Society. 154 (2007) A369.

[27] A. Oliveira Neto, J. Pérez, E. R. González, and E. A. Ticianelli. Platinum/Cobalt electrocatalysts dispersed on high surface area carbon: Study of the oxygen reduction reaction. Journal of New Materials for Electrochemical Systems. 2 (1999) 189.

[28] Eric J. Coleman, Muntasir H. Chowdhury, and Anne C Co. Insights into the oxygen reduction reaction activity of Pt/C and PtCu/C catalysts. ACS Catalysis. 5 (2015) 1245.

[29] G. Wu, H. T. Chung, M. Nelson, K. Artyushkova, K. L. More, C. Johnston, and P. Zelenay. Graphene-riched Co_9S_8-N-C non-precious metal catalyst for oxygen reduction in alkaline media components for alkaline PEFCs. ECS Transactions. 41 (2011) 1709.

[30] J. Pérez, E. R. González, and E. A. Ticianelli. Oxygen electrocatalysis on thin porous coating rotating platinum electrodes. Electrochimica Acta. 44 (1998) 1329.

[31] H. Yang, N. Alonso-Vante, J. M. Láger, and C. Lamy. Tailoring structure, and activity of carbon-supported nanosized Pt-Cr alloy electrocatalysts for oxygen reduction in pure and methanol-containing electrolytes. The Journal of Physical Chemistry B. 108 (2004) 1938.

[32] H. Yang, C. Coutanceau, J. M. Láger, N. Alonso-Vante, and C. Lamy. Methanol tolerant oxygen reduction on carbon-supported Pt–Ni alloy nanoparticles. Journal of Electroanalytical Chemistry. 576 (2005) 305.

[33] D. Morales-Acosta, L. G. Arriaga, L. Álvarez-Contreras, S. Fraire-Luna, and F. J. Rodríguez Varela. Evaluation of $Pt_{40}Pd_{60}$/MWCNT electrocatalyst as ethylene glycol-tolerant oxygen reduction cathodes. Electrochemical Communications. 11 (2009) 1414.

[34] L. Dermarconnay, C. Contanceau, and J. M. Léger. Electroreduction of dioxygen (ORR) in alkaline medium on Ag/C and Pt/C nanostructured catalysts - effect of the presence of methanol. Electrochimica Acta. 49 (2004) 4513.

[35] J. B. Goodenough, R. Manoharan, and R. Paranthaman. Surface protonation and electrochemical activity of oxides in aqueous solution. Journal of American Chemical Society. 112 (1990) 2076.

[36] V. Thiagarajan, R. Manoharan, P. Karthikeyan, E. Nikhila, A. Hernández-Ramírez, F. J. Rodríguez-Varela. Pt nanoparticles supported on $NiTiO_3$/C as electrocatalyst towards high performance methanol oxidation reaction. International Journal of Hydrogen Energy. 42 (2017) 9795.

Chapter VII

Electrocatalytic activity of the rGO-supported Pt-MTiO$_3$ (M = Ni, Co) catalysts for the Oxygen Reduction Reaction in alkaline media

7.1 Physicochemical characterization of the rGO support.

7.1.1 Vibrational spectra analysis by FTIR.

Figure 7.1 shows the FTIR spectrum of rGO. The aromatic stretching vibrations of the hybridized sp^2 C=C bond is visualized at 1480 and 1570 cm^{-1}. The absorption peaks localized in the 2930-2870 cm^{-1} region are associated to the symmetric/anti-symmetric vibrations of -CH_2 groups. Furthermore, the peaks at 3080 and 1330 cm^{-1} correspond to the O-H stretching and bending vibrations, respectively.

The absorption peak at 1740 cm^{-1} is assigned to C=O vibrations from carboxyl functional groups. Meanwhile, the peaks at 1120 y 990 cm^{-1} are ascribed to the stretching vibrations of C-O bonds from epoxy and alkoxy groups, respectively.[1-4] The structure of rGO with the oxygen functional groups is shown in the inset in Figure 7.1.

7.1.2 Raman spectroscopy characterization.

The Raman spectrum of carbonaceous materials is characterized by two main features, the D-band (usually observed at ~1575 cm^{-1}) which is representative of the presence of defects and structural disorder in graphitic systems caused by the breakage of the six-fold symmetry, and the G-band (at ~1350 cm^{-1})

which is the response of the in-plane stretching of symmetric vibrations of the sp^2 C=C bonds.[5-8]

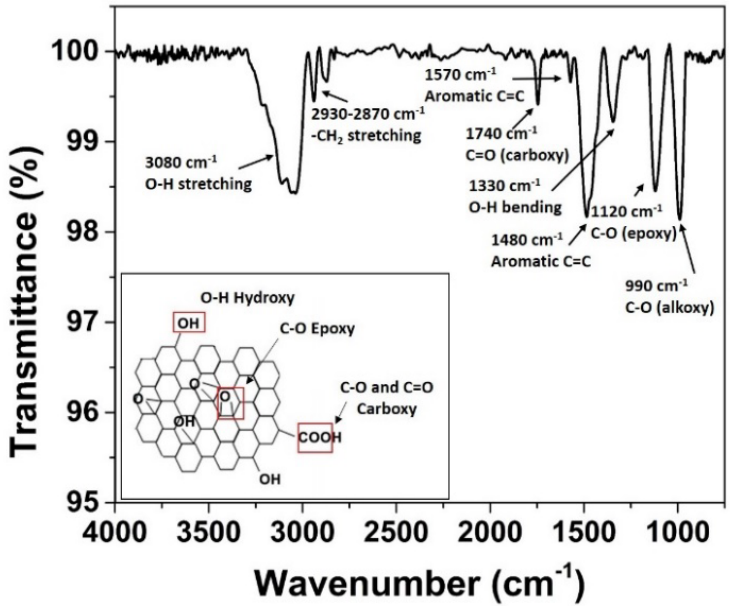

Figure 7.1 FTIR spectrum of rGO. The inset shows a schematic representation of the rGO structure.

The deconvoluted Raman spectrum of rGO in Figure 7.2 show a strong G-band at 1348.1 cm^{-1} along with a more intense D-band (at 1582.8 cm^{-1}). The relative intensity ratio between the D and G bands (I_D/I_G) has been calculated after Lorentzian fitting of the spectrum. This factor gives an approach to the density of defect sites in the rGO network. The I_D/I_G value of rGO is 1.2 due to the higher intensity of the D-band and indicates a disordered carbon structure. In this context, the deconvolution of the Raman spectrum is essential for understanding the structural characteristics of the rGO. Three additional bands can be observed in the spectrum. The D´ peak is ascribed to the vibration of graphene layers outside of the sandwich formed by other graphene layers; the D´´ band emerges from the fraction of amorphous carbon at the sample due to functional groups and the I peak, which can either be due to the sp^2-sp^3 mixed structure or to the increase in defects as a result of the reduction process.[9-14]

On the other hand, the high-frequency region of the Raman spectrum is deconvoluted into four Lorentzian peaks, i.e., D+D´´, 2D, D+D´ and 2D´ at 2445.5, 2658.8, 2925.3 and 3185.8 cm^{-1}, respectively.[15-17] The 2D peak is an overtone of the D band. Unlike the defect-induced D band, the 2D peak is an effect of the disorder or defects at carbon-based materials.

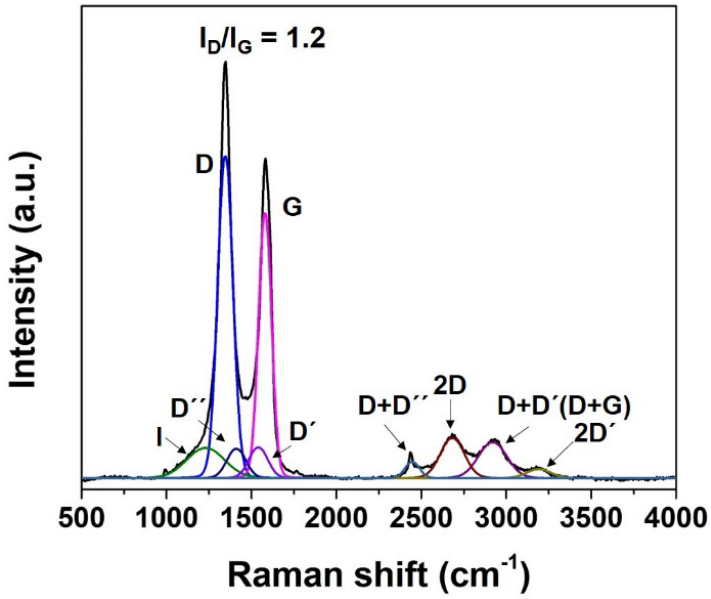

Figure 7.2 Raman spectrum of rGO.

7.2 Physicochemical characterization of the Pt/rGO, Pt-$NiTiO_3$/rGO and Pt-$CoTiO_3$/rGO catalysts.

7.2.1 X-Ray diffraction analysis (XRD).

Figures 7.3a-c show the XRD patterns of the Pt/rGO, Pt-$NiTiO_3$/rGO and Pt-$CoTiO_3$/rGO catalysts having the characteristic signals of Pt. The peaks can be indexed to the (111), (200), (220), (311) and (222) reflections of a typical polycrystalline face centered cubic (fcc) Pt structure. The reflection at 25° (2θ) is associated to the rGO support and corresponds to the (002) crystalline graphite plane. Figure 7.3d depicts a peak position analysis. Comparing the (311) reflection of Pt/rGO with those of Pt-$NiTiO_3$/rGO and Pt-$CoTiO_3$/rGO

(Figure 7.3d), it can be concluded that no significant shift to higher or lower angles is observed in the presence of titanates indicating that the addition of the oxide has no effect on the crystalline lattice of Pt. This observation is in agreement with previous reports of Pt-metal oxides catalysts.[18-20]

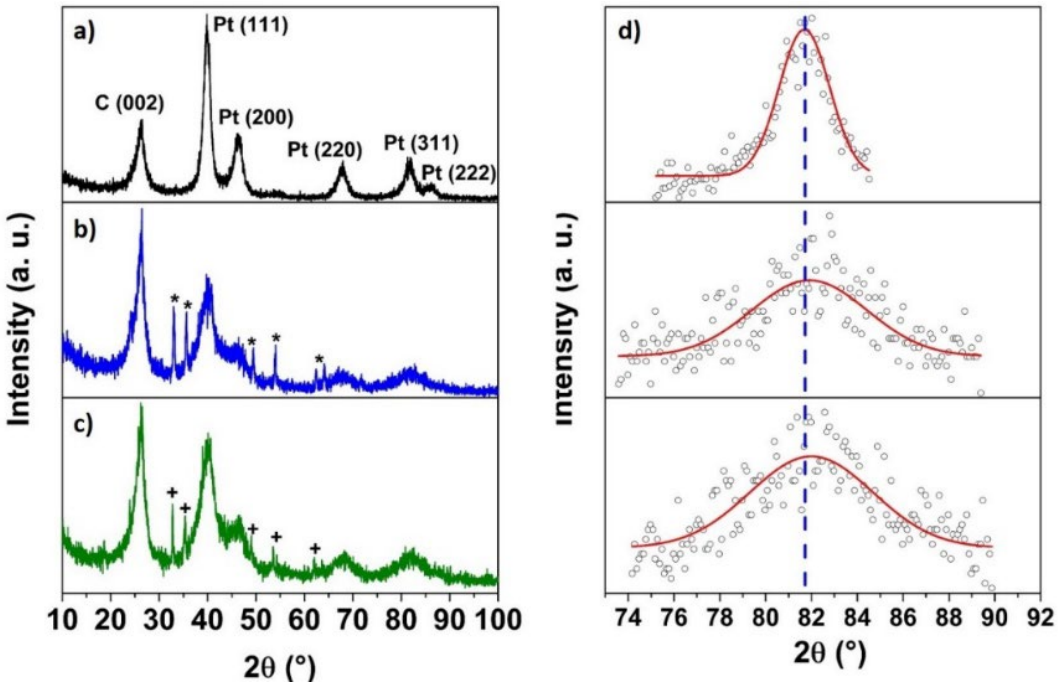

Figure 7.3 XRD patterns of a) Pt/rGO, b) Pt-$NiTiO_3$/rRGO and c) Pt-$CoTiO_3$/rGO catalysts. d) Zoom-in of the (311) reflections of each catalyst.

It is well known that the shape and position of the XRD peaks provide information about the crystallite size of fuel cell catalysts, by using the Scherrer formula (Equation 5.1 in Experimental section). Figure 7.3d shows that the (311) peak is broad, particularly at Pt-$NiTiO_3$/rGO and Pt-$CoTiO_3$/rGO suggesting the formation of nanostructured catalysts. The crystallite size from such reflection is 4.0 nm for Pt/rGO and decreases to 1.8 and 1.7 nm for Pt-$NiTiO_3$/rGO and Pt-$CoTiO_3$/rGO (Table 7.1).

7.2.2 SEM/EDS characterization.

The chemical composition of the Pt/rGO catalyst indicates a Pt and C content of 19.97 and 80.03 (wt. %) respectively, very close to the nominally expected values (Table 7.1). Meanwhile, Pt-$NiTiO_3$/rGO and Pt-$CoTiO_3$/rGO also have a Pt content of nearly 20 wt. %, higher than the theoretically calculated. For example, the Pt-$NiTiO_3$/C and Pt-$CoTiO_3$/C (in Chapter VI) have 10.37 and 8.56 wt. %, respectively. On the other hand, their C concentration is less than the expected 80 wt. %, a low value that can be attributed to the presence of titanates (10.63 and 12.17 wt. % at Pt-$NiTiO_3$/rGO and Pt-$CoTiO_3$/rGO, respectively). At these catalysts, the Pt-$MTiO_3$ ratio is 1:0.72 (at. %), close to the 1:1 value expected.

Table 7.1. Physicochemical features of the Pt/rGO, Pt-$NiTiO_3$/rGO and Pt-$CoTiO_3$/rGO catalysts.

	d_{XRD} (nm)	Particle size $_{TEM}$ (nm)	Chemical composition (wt. %)			Pt:$MTiO_3$ (at. %)
			Pt	$MTiO_3$	C	
Pt/rGO	4.0	4.0	19.97 ± 1.27	-	80.03 ± 1.01	-
Pt-$NiTiO_3$/rGO	1.8	2.0	18.93 ± 1.31	10.63 ± 0.90	70.97 ± 0.92	1:0.72
Pt-$CoTiO_3$/rGO	1.7	2.0	21.05 ± 1.34	12.17 ± 1.07	66.76 ± 1.40	1:0.72

SEM images of the rGO support and the Pt/rGO, Pt-$NiTiO_3$/rGO and Pt-$CoTiO_3$/rGO catalysts are shown in Figure 7.4. In all cases, the surface morphology is the typical micron-sized layered sheets, due to the rGO support.[21-23]

7.2.3 HR-TEM analysis.

The TEM image of Pt/rGO (Figure 7.5a) shows a morphology of Pt nanoparticles mostly quasi-spherical in shape and dispersed over the support with some degree of agglomeration. Figure 7.5b is a High Resolution TEM

micrograph of the catalyst showing nanosized particles. Analysis of particle size distribution has shown that the average particle size of Pt/rGO is 4.0 nm, in good agreement with XRD results (Table 7.1). The solid-line square over some of the nanoparticles is the zone where a Selected Area Electron Diffraction (SAED) pattern has obtained using an FFT analysis. The pattern is displayed as an inset in Figure 7.5c) and shows the crystalline nature of the Pt nanoparticles. Moreover, the reconstructed inverse FFT (iFFT) image in Figure 7.5c (obtained from the SAED pattern) allows to identify lattice fringes with an interplanar distance of 0.22 nm, ascribed to Pt nanoparticles grown preferentially along the (111) plane.[24,25]

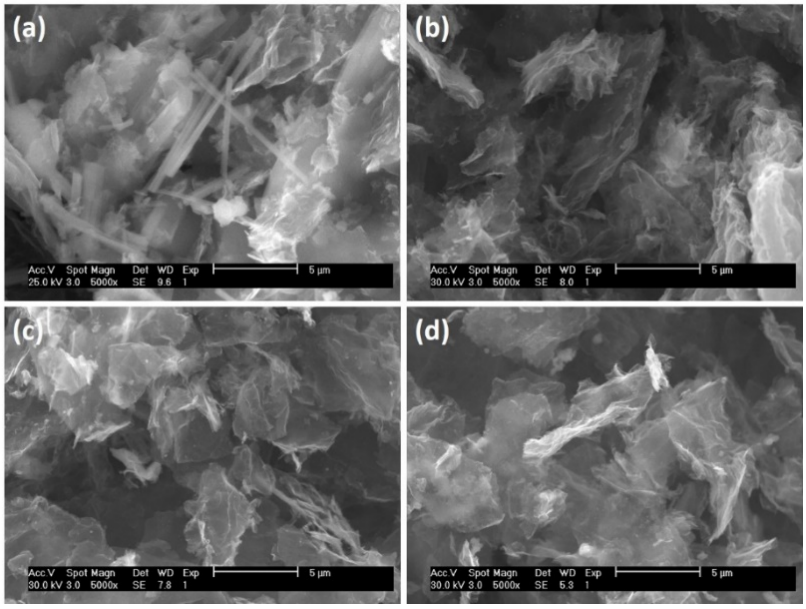

Figure 7.4 SEM images of a) RGO, b) Pt/RGO, c) Pt-$NiTiO_3$/RGO and d) Pt-$CoTiO_3$/RGO.

Likewise, Figure 7.5b also displays a dashed-line square over a zone involving the RGO support only. The inset in Figure 7.5d is the corresponding SAED pattern, with a single set of hexagonal spots, which correlates well with the typical six-fold symmetry of rGO. Moreover, the iFFT image in Figure 7.5d

clearly identifies the hexagonal atomic arrangement of the carbon nanostructure network.[26,27]

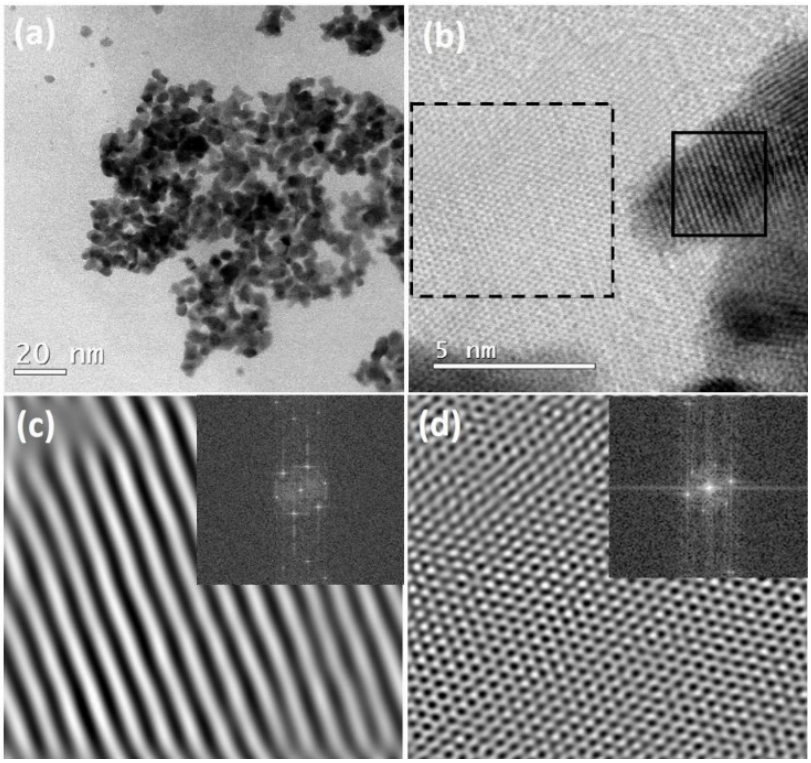

Figure 7.5 a) TEM and b) HR-TEM micrographs of Pt/rGO. c) reconstructured iFFT image from the SAED pattern (inset), which in turn has been obtained from the solid-line square in b). d) reconstructured iFFT image from the SAED pattern (inset), which in turn has been obtained from the dashed-line square in b).

Figure 7.6a is a representative TEM image of Pt-$NiTiO_3$/rGO. Its morphology is that of nanoparticles well dispersed over the rGO support, with slight agglomerations in some areas. Figure 7.6b shows the nanoscale of the particles, with an average size of 2.0 nm (Table 7.1). Figure 7.6c displays an image reconstructured (using the iFFT procedure) from the SAED pattern shown as inset, which in turn has been obtained from the solid-line square in Figure 7.6b. Analysis of the image allows to determine lattice fringes with an

interplanar distance of 0.22 nm corresponding to the (111) Pt plane. Figure 7.6d illustrates the iFFT reconstructed image, obtained from the SAED pattern (inset) derived from the dotted-line square in Figure 7.6b. A distance between lattice fringes of 0.25 has been determined, attributed to the (110) $NiTiO_3$ plane.[28,29]

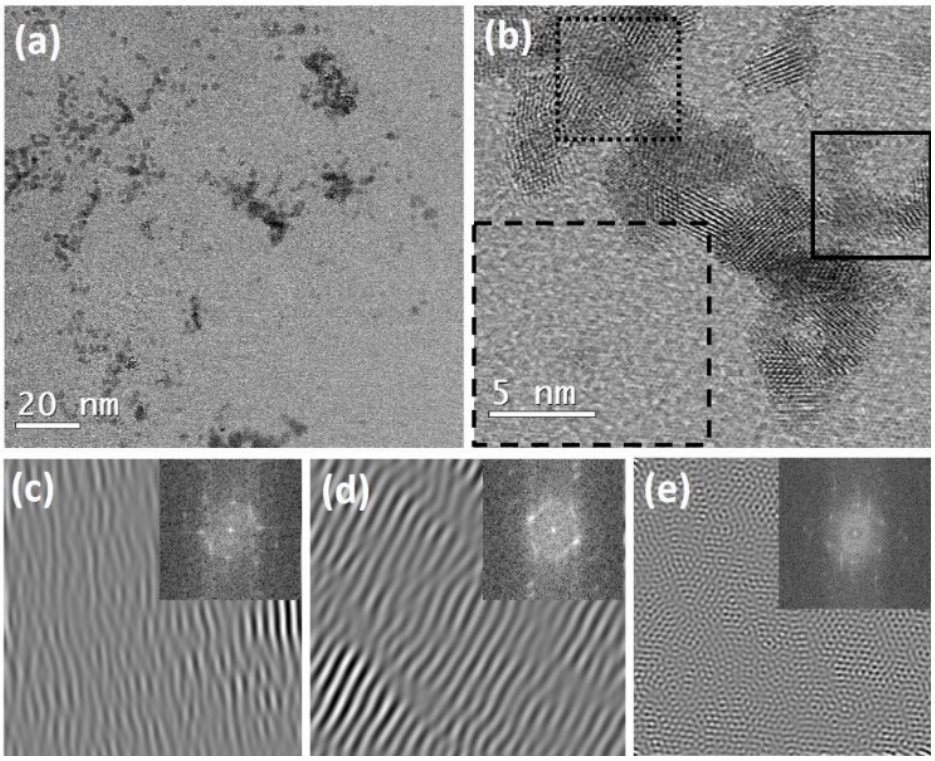

Figure 7.6 a) TEM and b) HR-TEM micrographs of Pt-$NiTiO_3$/rGO. c) reconstructured iFFT image from the SAED pattern (inset), which in turn has been obtained from the solid-line square in b). d) reconstructured iFFT image from the SAED pattern (inset), which in turn has been obtained from the dotted-line square in b). e) reconstructured iFFT image from the SAED pattern (inset), which in turn has been obtained from the dashed-line square in b).

The structural characteristics obtained from Figures 7.6d-b confirm that the presence of Pt and $NiTiO_3$ at the Pt-$NiTiO_3$/rGO catalyst. On the other hand,

the inset in Figure 7.6e is the SAED pattern obtained from the dashed-line in Figure 7.6b, i.e., a zone covering rGO only. It shows a ring of six spots which confirms the hexagonal network of rGO. Meanwhile, Figure 7.6e is an image reconstructured after iFFT analysis of the inset confirming a well-resolved graphene-like lattice.

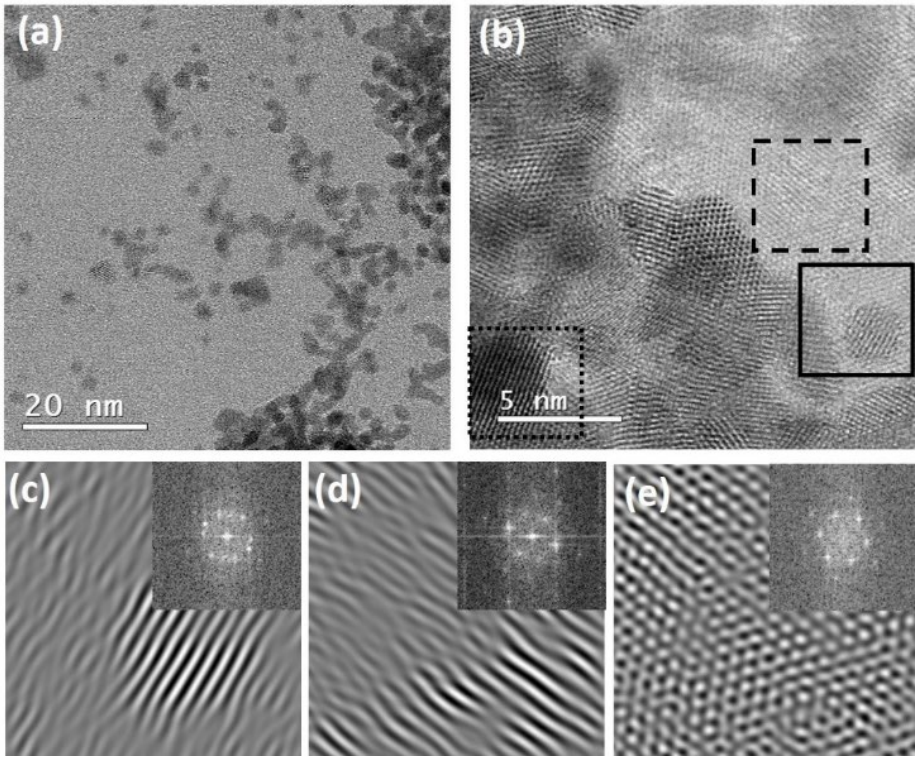

Figure 7.7 a) TEM and b) HR-TEM micrographs of Pt-$CoTiO_3$/rGO. c) reconstructured iFFT image from the SAED pattern (inset), which in turn has been obtained from the solid-line square in b). d) reconstructured iFFT image from the SAED pattern (inset), which in turn has been obtained from the dotted-line square in b). e) reconstructured iFFT image from the SAED pattern (inset), which in turn has been obtained from the dashed-line square in b).

A similar analysis has been developed for Pt-$CoTiO_3$/rGO. TEM and HR-TEM micrographs shows the nanostructured morphology of the catalyst (Figures

7.7a-b). The reconstructed iFFT images in Figures 7.7c-e where derived from the corresponding insets, in turn developed from the solid, dotted and dashed-line squares in 7.7b, respectively. Interplanar distances of 0.21 and 0.36 nm have been determined from Figures c and d), respectively, attributed to Pt (111) and $CoTiO_3$ (012).[21] Meanwhile, by applying a hexagonal mask to the six-spots inset in Figure 7.7e, the corresponding iFFT pattern clearly depicts the typical honeycomb hexagonal-network of rGO.

7.2.4 Chemical surface analysis by XPS.

Figure 7.8 shows the high resolution XPS spectra of Pt/rGO. The Pt 4f binding energy (BE) region shows the $4f_{7/2}$ and $4f_{5/2}$ states due to spin-orbit splitting and has been deconvoluted into three doublets (Figure 7.8a).

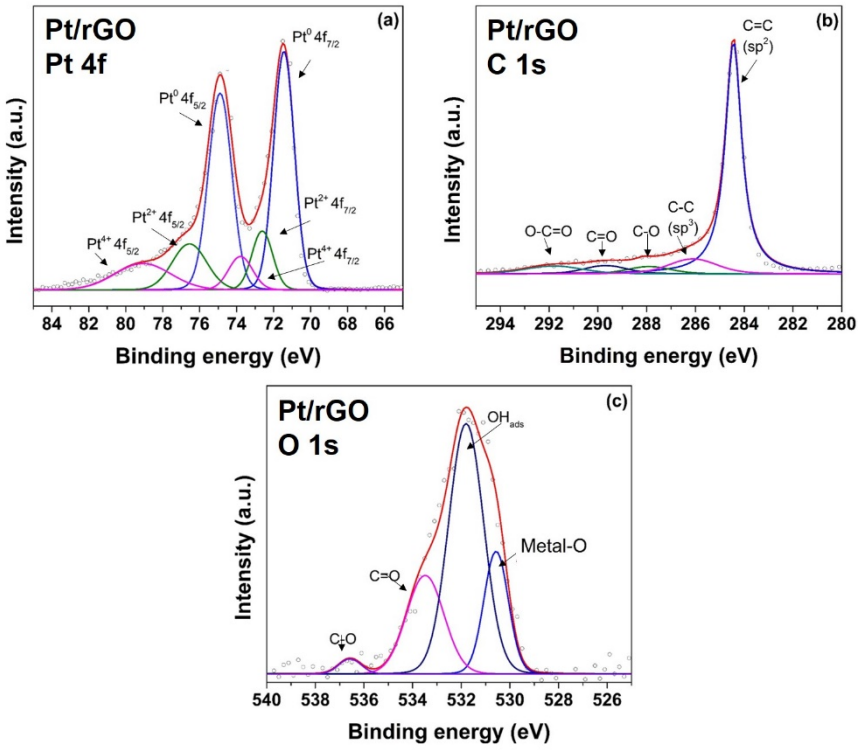

Figure 7.8 High resolution XPS spectra of the Pt/rGO catalyst: a) Pt 4f, b) C 1s and c) O 1s BE regions.

The peaks observed at 71.4 and 74.9 eV (Table 5.2) are attributed to Pt in metallic state (Pt^0). The peaks at 72.5 and 76.5 eV correspond to Pt^{2+} oxidation state and may be assigned to PtO. Meanwhile, the doublet observed at 73.8 and 79.0 eV is due to the presence of the Pt^{4+} species, specifically PtO_2.[30-32]

Figure 7.8b shows the C 1s core-level of the Pt/rGO catalyst. The most intense peak at 284.4 eV is attributed to the C=C sp^2 hybridization of the rGO support. A smaller contribution of C-C sp^3 is demonstrated by the low-intensity peak at a BE of 286.1 eV. The peaks with BEs of 287.8, 289.6 and 291.7 eV are ascribed to several oxygen-containing carbon groups: C-O, C=O and O-C=O, respectively. Such characteristics are typically observed for the rGO structure.[31,33]

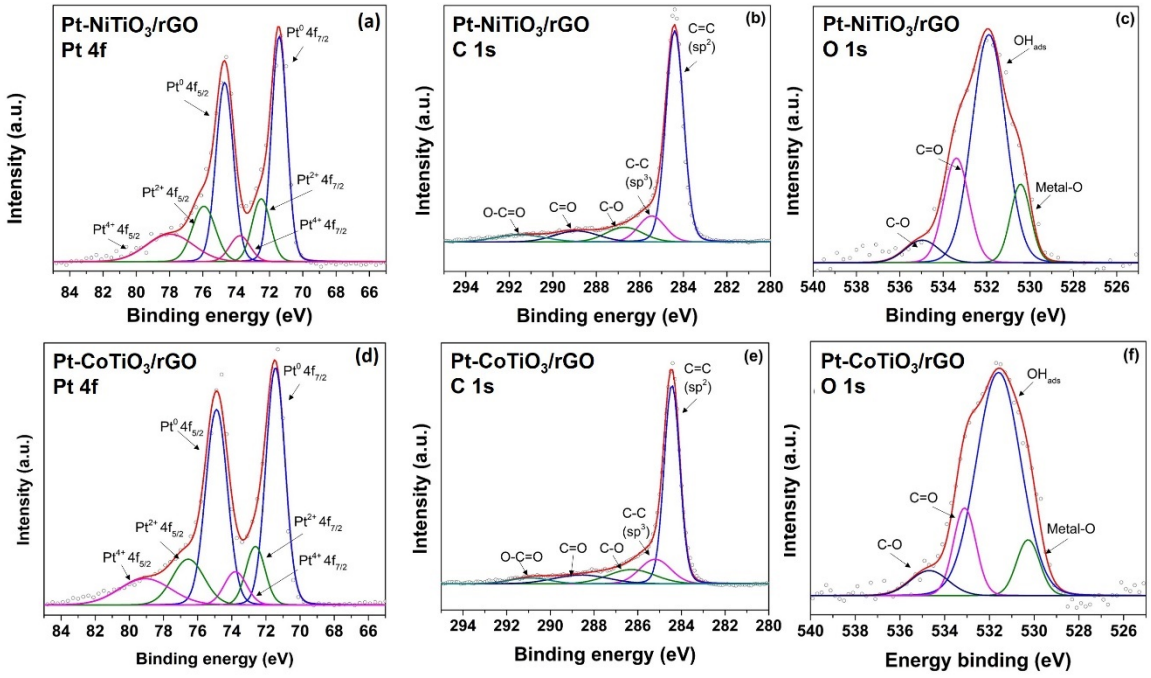

Figure 7.9 High resolution XPS spectra of Pt-$NiTiO_3$/rGO catalyst: a) Pt 4f, b) C 1s, c) O 1s regions; and of Pt-$CoTiO_3$/rGO: d) Pt 4f, e) C 1s and f) O 1s regions.

The O1s core level region in Figure 5.8c has also been deconvoluted into several states. The peak at BE = 530.7 eV is assigned to oxygen ions (O^{2-}) in the crystal lattice of PtO[34-36] while the signal centered at 531.8 eV has been suggested to be due to the hydroxyl ions adsorbed on the Pt-surface.[37,38] In addition, the peaks at 533.4 and 536.5 eV are associated with the C=O and C-O species, in agreement with the C 1s spectrum.

XPS analysis of the metaltitanate-based catalysts has also been performed. Figure 7.9a shows the spectrum of Pt-$NiTiO_3$/rGO in the Pt4f region, deconvoluted into three doublets as in the case of Pt/rGO. The most significant contribution at the Pt $4f_{7/2}$ and Pt $4f_{5/2}$ state is that of Pt^0, compared to the Pt^{2+} and Pt^{4+} species. The BE in the Pt $4f_{7/2}$ state of Pt^0 is 71.6 eV, a shift of 0.2 eV compared to Pt/rGO (Table 7.2) that can be attributed to a change in the *d*-valence band of the Pt due to an electron transfer from $NiTiO_3$ to platinum atoms.[39] However, it cannot be suggested that alloyed phases have been formed, in agreement with the XRD analysis in Figure 7.3.

The high-resolution C 1s region of Pt-$NiTiO_3$/rGO in Figure 7.9b has been deconvoluted into five components, having a main peak at 284.4 eV assigned to the C=C sp^2 hybridization bond of rGO. The C-C sp^3 bond shows a lower contribution with a peak at ~285 eV. The peaks located at 286.7, 288.9 and 291.5 eV are attributed to the C-O, C=O and O-C=O bonds, respectively. Meanwhile, the peak at BE of 530.4 eV in the O 1s region rGO (Figure 7.9c) arises from Metal-O bonds which may be due to Pt-oxides and/or the $NiTiO_3$ compound. This signal is analogous to the Pt-O observed at Pt/rGO in Figure 7.8c. Even more, the strong peak at 531.8 eV is assigned to surface hydroxyl groups, while the peaks at 533.3 and 535 eV correspond to C=O and C-O functional-groups at the carbon support.

Figures 7.9d-f show the spectra of Pt-$CoTiO_3$/rGO in the Pt 4f, C 1s and O 1s regions. The shift in BE of Pt^0 in the $Pt4f_{7/2}$ state (71.5 eV) compared to Pt/rGO is 0.1 eV, less than in the previous case. It can be observed that the signals of Pt-$CoTiO_3$/rGO are similar to those of Pt-$NiTiO_3$/rGO. Moreover, it should be mentioned that low-intensity signal of Ni, Ti and Co have been detected at Pt-$NiTiO_3$/rGO and Pt-$CoTiO_3$/rGO (spectra not shown). Overall, the same species have been detected for the three catalysts, with some variations in the relative intensities of several of the peaks. Table 7.2 shows the identified species along with their oxidation state and BE.

Table 7.2 XPS parameters of Pt/rGO, PT-$NiTiO_3$/rGO and Pt-$CoTiO_3$/rGO.

Catalyst	Species	State	BE (eV)
Pt/rGO	Pt^0	Pt 4f $_{7/2}$	71.4
		Pt 4f $_{5/2}$	74.9
	PtO	Pt 4f $_{7/2}$	72.5
		Pt 4f $_{5/2}$	76.5
	PtO_2	Pt 4f $_{7/2}$	73.8
		Pt 4f $_{5/2}$	79.0
	C=C sp^2	C 1s	284.4
	C-C sp^3	C 1s	286.1
	C-O	C 1s	287.8
	C=O	C 1s	289.6
	O-C=O	C 1s	291.7
	Metal-O	O 1s	530.7
	OH_{ads}	O 1s	531.8
	C=O	O 1s	533.4
	C-O	O 1s	536.5
Pt-$NiTiO_3$/rGO	Pt^0	Pt 4f $_{7/2}$	71.6
		Pt 4f $_{5/2}$	74.6

	PtO	Pt 4f $_{7/2}$	72.5
		Pt 4f $_{5/2}$	75.9
	PtO_2	Pt 4f $_{7/2}$	73.8
		Pt 4f $_{5/2}$	78.0
	C=C sp^2	C 1s	284.4
	C-C sp^3	C 1s	285.4
	C-O	C 1s	286.7
	C=O	C 1s	288.9
	O-C=O	C 1s	291.5
	Metal-O	O 1s	530.4
	OH_{ads}	O 1s	531.8
	C=O	O 1s	533.3
	C-O	O 1s	535.0
Pt-$CoTiO_3$/rGO	Pt^0	Pt 4f $_{7/2}$	71.5
		Pt 4f $_{5/2}$	74.9
	PtO	Pt 4f $_{7/2}$	72.5
		Pt 4f $_{5/2}$	76.5
	PtO_2	Pt 4f $_{7/2}$	73.8
		Pt 4f $_{5/2}$	79.0
	C=C sp^2	C 1s	284.4
	C-C sp^3	C 1s	285.1
	C-O	C 1s	286.3
	C=O	C 1s	288.7
	O-C=O	C 1s	290.9
	Metal-O	O 1s	530.2
	OH_{ads}	O 1s	531.5
	C=O	O 1s	533.1
	C-O	O 1s	534.7

7.3 Catalytic activity of the Pt/rGO, Pt-$NiTiO_3$/rGO and Pt-$CoTiO_3$/rGO catalysts for the ORR.

7.3.1 ORR kinetics.

Figure 7.10 shows the CVs of Pt/rGO, Pt-$NiTiO_3$/rGO and Pt-$CoTiO_3$/rGO. The hydrogen adsorption/desorption peaks on the polycrystalline Pt surface are clearly seen (~0.05 to 0.50 V/RHE). The formation of Pt-oxides is observed in the anodic scan at potentials above ca. 0.70 V/RHE and their subsequent reduction in the cathodic sweep, indicated by a peak current density at around 0.77 V/RHE. On the other hand, the double layer region is wider that in the case of the Vulcan-supported catalysts (Chapter VI) which is attributed to the electrochemical behavior of rGO. It is well-known that graphene supports have a high electrical double layer capacitance due to their specific surface area and this effect can be seen in the CVs in the Figure 7.10.[40,41]

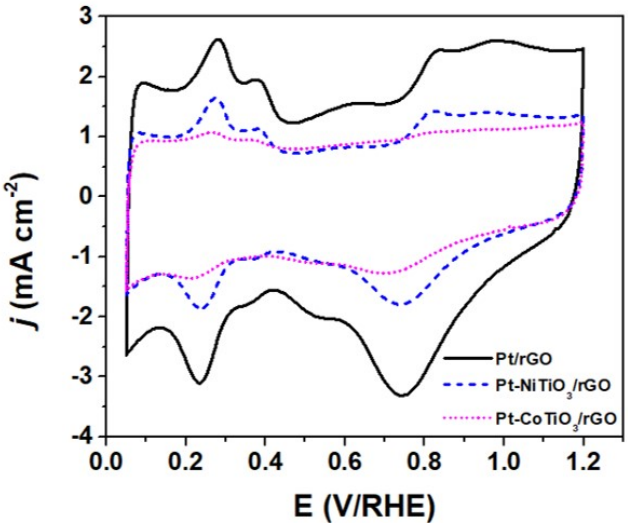

Figure 7.10 CVs of the Pt/rGO, Pt-$NiTiO_3$/rGO and Pt-$CoTiO_3$/rGO catalysts. Electrolyte: N_2-satured 0.5 M KOH. Scan rate of 20 mV s^{-1}.

The electrochemical active surface area (ECSA) provides important information regarding the number of electrochemically active sites per gram of

catalyst. At first, the H_{UPD} coulombic charge (Q_H) has been calculated from the area under the hydrogen desorption region after double-layer correction. This value represents the number of hydrogen atoms desorbed and therefore the number of adsorption sites.[41] Table 7.3 summarizes the Q_H, the real area (A_{Pt}) and the electrochemically active area (ECSA) values of the catalysts obtained with the Equations 5.5 and 5.9 (Chapter V).

The ECSA of Pt/rGO catalyst is calculated to be 62.33 $m^2\ g^{-1}$, which is clearly larger than those of Pt-$NiTiO_3$/rGO and Pt-$CoTiO_3$/rGO. The decrease in ECSA values in Pt-$NiTiO_3$/rGO and Pt-$CoTiO_3$/rGO catalysts can be explained in terms of the inaccessibility of H^+ to the Pt surface due to the presence of the metaltitanate, being not electrochemically active sites.

Table 7.3 Electrochemical parameters of Pt/rGO, Pt-$NiTiO_3$/rGO and Pt-$CoTiO_3$/rGO.

Catalyst	Q_H (μC)	A_{Pt} (cm^2)	ECSA ($m^2\ g^{-1}$)	E_{onset} (V/RHE)	$j_{0.9\ V/RHE}$ ($mA\ cm^{-2}$)
Pt/rGO	2610	12.44	62.33	1.04	-0.94
Pt-$NiTiO_3$/rGO	1510	7.18	39.07	1.00	-0.41
Pt-$CoTiO_3$/rGO	533	2.54	12.07	0.99	-0.41

The polarization curves of the ORR at Pt/rGO, Pt-$NiTiO_3$/rGO and Pt-$CoTiO_3$/rGO at different rotation rates after background current subtraction (see Chapter V) are shown in Figure 7.11. The current vs. potential curves have been acquired at 5 mV s^{-1} in the 1.2 to 0.05 V/RHE interval. It is shown that all polarization curves have three regions under different control mechanisms: i) a kinetic due to charge transfer limitations at high overpotentials, ii) mixed at intermediate overpotentials, and iii) diffusion-controlled at high overpotentials. As can be seen, higher rotational speeds result in an increase of current densities (*j*) due to the oxygen diffusion to electrode surface.

The Pt/rGO catalyst has an onset potential (E_{onset}) for the ORR of 1.04 V/RHE and a *j* value of -0.94 mA cm^{-1} at 0.9 V/RHE (Table 7.3). A slight negative shift in E_{onset} is observed for Pt-$NiTiO_3$/rGO and Pt-$CoTiO_3$/rGO (1.00 and 0.99 V/RHE, Figures 5.11b and c, respectively). However, the current density of Pt-$NiTiO_3$/rGO and Pt-$CoTiO_3$/rGO at 0.9 V/RHE decreases to -0.41 mA cm^{-1}, in both cases (Table 7.3).

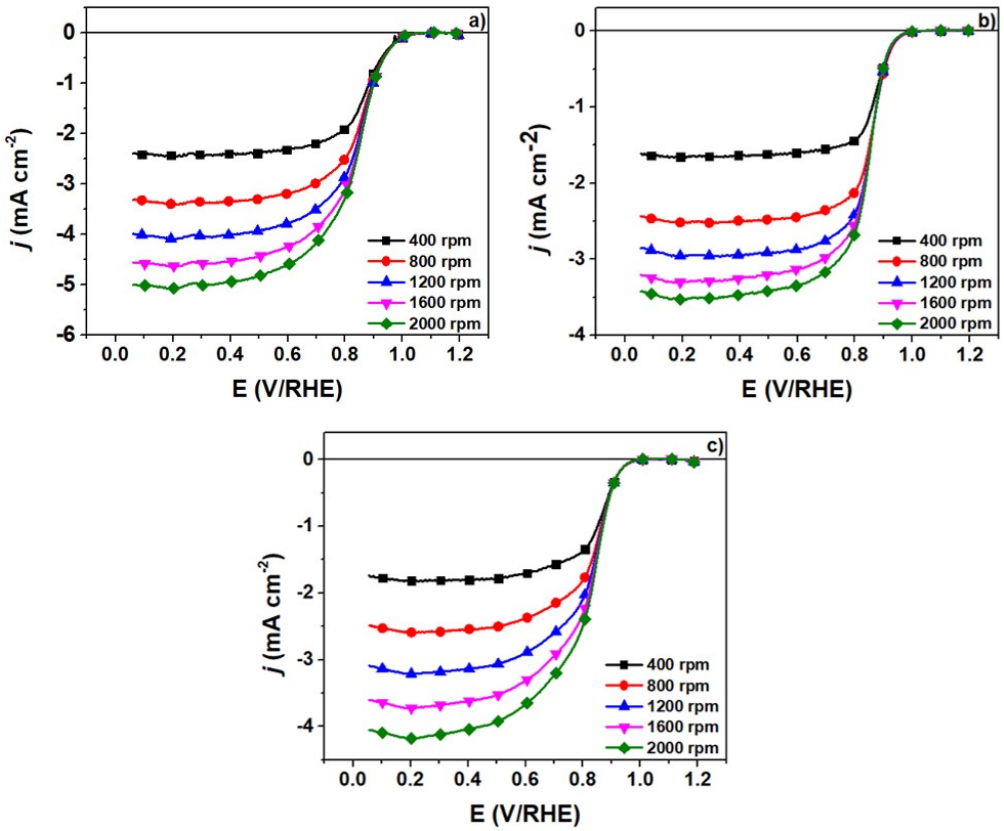

Figure 7.11 Polarization curves for the ORR on: a) Pt/rGO, b) Pt-$NiTiO_3$/rGO and c) Pt-$CoTiO_3$/rGO in O_2-satured 0.5 M KOH electrolyte. Scan rate: 5 mV s^{-1}.

As indicated in reactions 2.15-2.19 (from Chapter II) the ORR is a multielectron transfer process that has two main possible pathways. One is a four-electron transfer mechanism where molecular oxygen is directly reduced to OH^-. The second one, is a two-step mechanism through which oxygen is reduced to HO_2^-

(two-electron transfer mechanism) followed by a further reduction to OH^- (also a two-electron transfer process).[42,43] In order to construct the Koutecky-Levich plots that serve as a basis to elucidate the ORR mechanism, *j* values at different rotation rates and several potentials have been considered. Figure 7.12 shows the Koutecky-Levich plots of Pt/rGO, Pt-$NiTiO_3$/rGO and Pt-$CoTiO_3$/rGO. The number of electrons transferred per oxygen molecule (*n*) was calculated from the Koutecky-Levich slope (*B* in Equation 5.7 from the experimental section). The ORR on Pt/rGO and Pt-$NiTiO_3$/rGO proceeds predominantly by the direct $4e^-$ pathway (n = 3.8 and 3.5, respectively). On the other hand, the number of electrons involved in the overall ORR on the Pt-$CoTiO_3$/rGO catalyst was calculated to be *n* = 2.4.

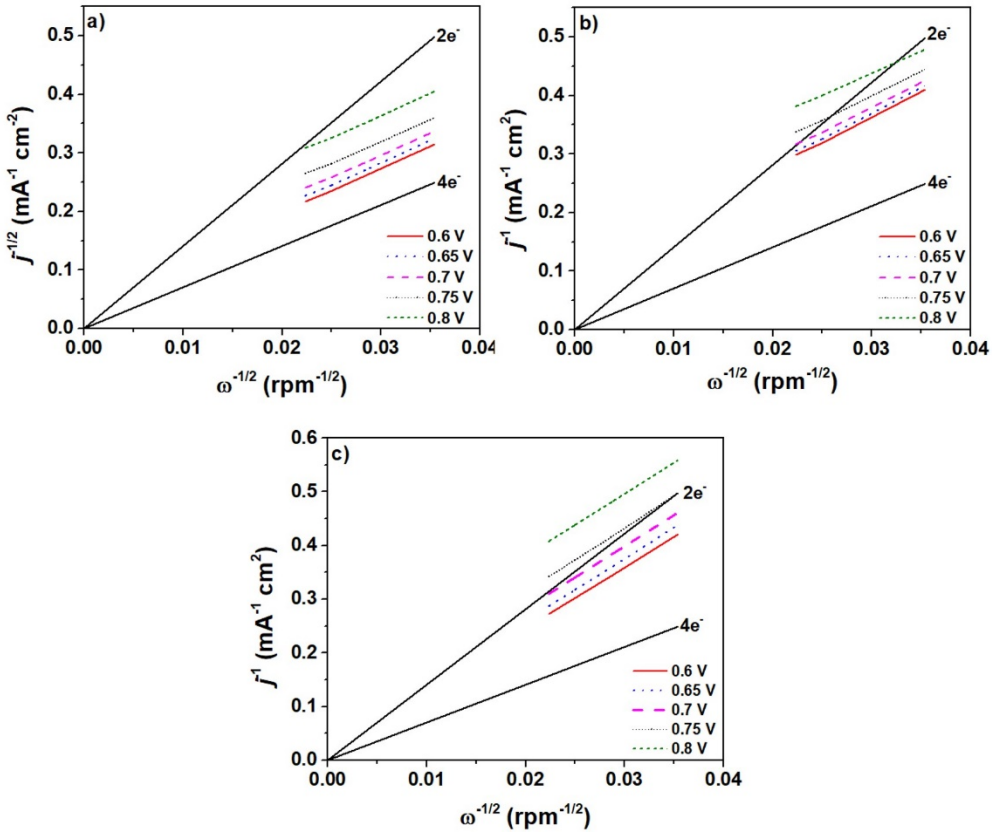

Figure 7.12 Koutecky-Levich plots of the ORR at different electrode potentials on Pt/rGO (a), Pt-$NiTiO_3$/rGO (b) and Pt-$CoTiO_3$/rGO (c).

Mass and specific activity Tafel plots have been obtained from the ORR polarization curves by using the mass-transport correction (Equation 5.8 from the experimental section) and normalizing the current to the Pt content (to obtain i_m, in A mg^{-1}_{Pt}) and the real area of Pt (to determine i_s, in mA cm^{-2}_{Pt}), respectively. The Tafel plots on Pt/rGO, Pt-$NiTiO_3$/rGO and Pt-$CoTiO_3$/rGO exhibit two slopes, as can be seen in Figure 7.13. As discussed earlier, the change in the slope has been interpreted as a change from a Temkin to a Langmuir adsorption isotherm with decreasing coverage of oxygenated species and the first electron transfer as rate determining step.[44-46]

Tafel slopes at lop of 64 mV dec^{-1} for Pt-$NiTiO_3$/rGO and 70 mV dec^{-1} for Pt-$CoTiO_3$/rGO have been obtained (Table 5.4), fairly close to the expected theoretical value of 60 mv dec^{-1}. The *b* values are similar, indicating that the ORR proceeds via the same pathway in such potential range at both catalysts. Meanwhile, the *b* value al lop in the case of Pt/rGO is considerably higher (102 mv dec^{-1}) as given in Table 7.4. At hop, the *b* values at Pt/rGO, Pt-$NiTiO_3$/rGO and Pt-$CoTiO_3$/rGO are 236, 153 and 176 mV dec^{-1}, respectively, i.e., significantly higher than the 120 mV dec^{-1} expected.

Some works that have been devoted to elucidate the dependence of the Tafel slope with the state of the electrode surface, suggesting that higher experimental Tafel slopes at lop may be ascribed to a change in the O_2 adsorption mechanism, because the oxygen dissociative process can be the rate-determining step.[47-51] Also, it has been proposed that the variation in Tafel slopes may be due to a participation of the rGO support on the ORR.[52] It should be remembered than non-noble metal graphene catalysts have been evaluated for the ORR in alkaline media showing a high catalytic activity.[53-56]

The mass activity (i_m, data from Figure 7.13) of the catalysts at 0.9 V/RHE is shown in Table 5.4. The value at Pt/rGO is 0.011 A mg^{-1}_{Pt}, clearly higher than

Pt-NiTiO$_3$/rGO and Pt-CoTiO$_3$/rGO with about the same amount of Pt at the catalysts (Table 7.1). On the other hand, Pt-CoTiO$_3$/rGO is the most active catalyst in terms of specific activity (i_s) with a value of 28.2 μA cm$^{-2}_{Pt}$, a 1.5 and 2.6-fold increase over Pt/rGO and Pt-NiTiO$_3$/rGO (18.2 and 10.8 μA cm$^{-2}_{Pt}$, respectively). The specific activity of the catalyst can be correlated with the CVs in Figure 7.10 and the corresponding A_{Pt} values in Table 7.3. Even though Pt-CoTiO$_3$/RGO has a smaller A_{Pt}, the exposed Pt sites catalyze the ORR to a larger extent compared to Pt/rGO.

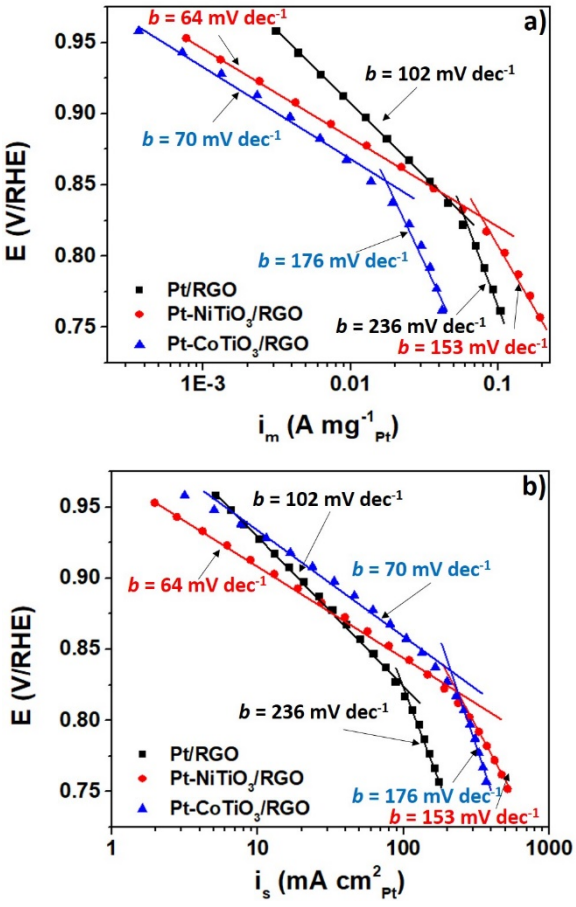

Figure 7.13 (a) Mass and (b) specific activity plots of the ORR on Pt/rGO, Pt-NiTiO$_3$/rGO and Pt-CoTiO$_3$/rGO catalysts. Electrolyte: 0.5 M KOH saturated with O_2. ω = 2000 rpm.

Table 7.4 Mass and specific activities data for ORR at Pt/rGO, Pt-$NiTiO_3$/rGO and Pt-$CoTiO_3$/rGO catalysts.

Catalyst	*b* at lop (mV dec^{-1})	*b* at hop (mV dec^{-1})	Mass activity at 0.9 V/RHE (A mg^{-1}_{Pt})	Specific activity at 0.9 V/RHE (μA cm^{-2}_{Pt})
Pt/rGO	102	236	0.011	18.2
Pt-$NiTiO_3$/rGO	64	153	0.005	10.8
Pt-$CoTiO_3$/rGO	70	176	0.003	28.2

7.3.2 Tolerance tests.

In A-DAFCs, the fuel and/or the oxidation intermediaries can diffuse from the anode to the cathode through the polymer electrolyte membrane, seriously decreasing the performance of the cathode catalyst.[57] Therefore, a good cathode catalyst should be able to selectively promote the ORR, instead of oxidizing the fuel. The catalytic activity towards the ORR of Pt/rGO, Pt-$NiTiO_3$/rGO and Pt-$CoTiO_3$/rGO in the presence of (0.1 and 0.5 M) CH_3OH and C_2H_5OH has been evaluated.

As shown in Figure 7.14a, the Pt/rGO catalyst exhibits high electrocatalytic activity of methanol oxidation reaction since the positive current densities reach 11.5 and 21.5 mA cm^{-2} for concentrations of 0.1 and 0.5 M of the fuel, respectively (see Table 7.5). Also, a high oxidation current density is observed when the ethanol concentration is 0.5 M. With a concentration of 0.1 M C_2H_5OH, negative current densities are generated over the potential scanned. In terms of ORR current densities, the Pt/rGO catalyst is greatly affected by C_2H_5OH, since in the presence of both concentrations of the fuel, the ORR diffusion-controlled current density decreases from -5.07 mA cm^{-2} (at 0.1 V/RHE in fuel-free electrolyte saturated with O_2) to -3.13 and -0.92 mA cm^{-2}, respectively. With 0.1 M C_2H_5OH, there is an increase in E_{onset} relative to the value without fuel, but the value has not been obtained with 0.5 M C_2H_5OH (Table 7.5). Overall, the decay in catalytic activity of Pt/rGO for the ORR is due

to the well-known high activity of Pt towards the methanol and ethanol oxidation reactions, the catalytic sites may absorb oxygen and/or fuel molecules in a strong competition leading to a mixed reaction that decreases the activity of Pt for the ORR.[58]

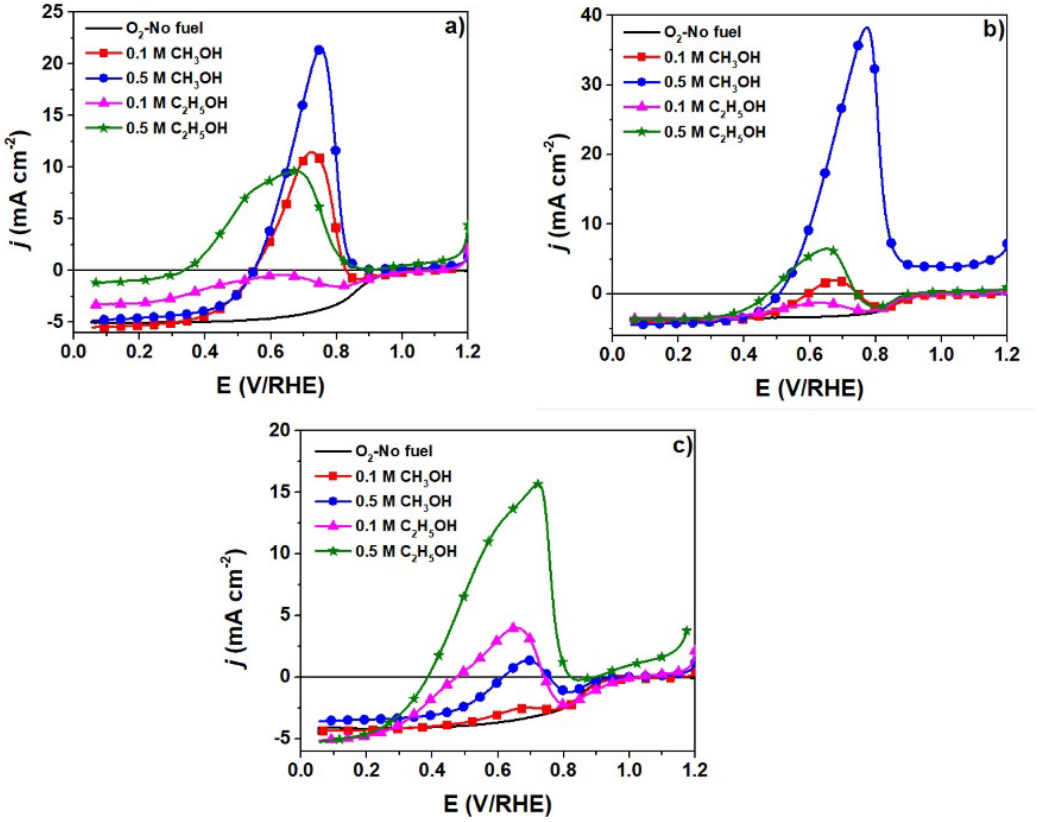

Figure 7.14 Polarization curves of the ORR at (a) Pt/rGO, (b) Pt-$NiTiO_3$/rGO and (c) Pt-$CoTiO_3$/rGO in the absence and presence of 0.1 and 0.5 M CH_3OH or C_2H_5OH. Electrolyte: O_2-satured 0.5 M KOH. Scan rate: 5 mV s^{-1}. ω = 2000 rpm.

Table 7.5 Fuel oxidation current densities and ORR E_{onset} on Pt/rGO, Pt-$NiTiO_3$/rGO and Pt-$CoTiO_3$/rGO in the presence of 0.1 and 0.5 M CH_3OH and C_2H_5OH.

	***j* (mA cm^{-2})**				***E*$_{onset}$ (V/RHE)**				
	CH_3OH		**C_2H_5OH**		**O_2-No fuel**	**CH_3OH**		**C_2H_5OH**	
Catalyst	**0.1 M**	**0.5 M**	**0.1 M**	**0.5 M**		**0.1 M**	**0.5 M**	**0.1 M**	**0.5 M**
Pt/rGO	11.5	21.5	-0.34	9.64	1.04	1.04	-	1.09	-
Pt-$NiTiO_3$/rGO	2.12	38.4	-1.22	6.56	1.00	1.08	-	0.96	0.90
Pt-$CoTiO_3$/rGO	-2.44	1.37	3.99	15.63	0.99	1.06	0.97	1.01	0.88

Figure 7.14b shows the polarization curves of Pt-$NiTiO_3$/rGO in O_2-satured electrolyte in the presence of 0.1 and 0.5 M of CH_3OH and C_2H_5OH. An intense current density peak (about 38.4 mA cm^{-2}) appears in the presence of 0.5 M CH_3OH. With 0.1 M CH_3OH the peak current density is smaller, but still positive (2.12 mA cm^{-2}, Table 7.5). The E_{onset} with 0.1 M CH_3OH is 80 mV more positive than in the absence of the fuel (with 0.5 M CH_3OH it could not been determined). Pt-$NiTiO_3$/rGO results to be less active for the ethanol oxidation reaction (EOR) in the O_2-satured electrolyte than Pt/rGO, since its oxidation currents are much lower. A concentration of 0.1 M ethanol causes an increase in the ORR overpotential of 40 mV, while the shift is of 100 mV with 0.5 M fuel, in comparison with the E_{onset} of the fuel-free electrolyte (see Table 7.5). In the Pt-$NiTiO_3$/rGO catalyst, there is no noticeable variation in the ORR diffusion-controlled current densities with CH_3OH and C_2H_5OH.

From Figure 7.14c it is evident that the tolerance of Pt-$CoTiO_3$/rGO to methanol is higher than those of Pt/rGO and Pt-$NiTiO_3$/rGO, since lower methanol oxidation current densities are obtained (see Table 7.5). Thus, the catalytic activity of Pt-$CoTiO_3$/rGO for the ORR in the methanol-containing electrolyte is less affected. Moreover, the polarization curve of the ORR at Pt-$CoTiO_3$/rGO in the presence of 0.1 M CH_3OH is quite similar to that in the methanol-free

electrolyte. This indicates that the presence of methanol has no significant effect on the catalytic activity of the catalyst for the ORR. With low methanol concentration, the E_{onset} value is positively shifted 70 mV relative to the ORR without alcohol (Table 7.5). At 0.5 M CH_3OH, a positive current density is generated, due to the MOR.

On the other hand, in the presence of 0.1 and 0.5 M C_2H_5OH, the behavior of Pt-$CoTiO_3$/rGO is similar to the other catalysts, i.e., it generates positive current densities (Table 7.5). Also, the E_{onset} values shift positively by 20 mV at low, and negatively by 110 mV at high alcohol concentration.

These findings suggest that the Pt-$CoTiO_3$/rGO catalyst is almost fully methanol tolerant (at an alcohol concentration of 0.1 M) and can selectively perform the ORR in the presence of methanol. Such tolerance to methanol may be associated with the fact that the dissociative chemisorption of oxygen requires two adjacent Pt-sites, while that of the alcohol requires at least three. The cobalt titanate as co-catalyst reduces the probability of having three neighboring Pt atoms thereby suppressing the methanol adsorption and further oxidation. Thus, the ORR is more favorable at the Pt-$CoTiO_3$/rGO catalyst.[59-61] This performance makes a promising cathode catalyst for practical A-DAFC applications.

7.4 References.

[1] L. Kashinath, K. Namratha, S. Srikantaswamy, A. Vinu, and K. Byrappa. Microwave treated sol-gel synthesis and characterization of hybrid ZnS-RGO composites for efficient photodegradation of dyes. New Journal of Chemistry. 41 (2017) 1723.

[2] M. Zhong, Y. Huang, Y. Zhao, X. Sun, C. Qu, D. Luo, and J. Zheng. Facile preparation, high microwave absorption and microwave absorbing mechanism of RGO-Fe_3O_4 composites. RSC Adv. 3 (2013) 23638.

[3] X. Huang, N. Hu, R. Gao, Y. Yu, Y. Wang, Z. Yang, E. Kong, H. Wei, and Y. Zhang. Reduced graphene oxide -polyaniline hybrid: Preparation, characterization and its applications for ammonia gas sensing. Journal of Materials Chemistry. 22 (2012) 22488.

[4] B. D. Ossonon, and D. Bèlanger. Synthesis and characterization of sulfophenyl-functionalized reduced graphene oxide sheets. RSC Advances. 7 (2017) 27224.

[5] A. Kaniyoor, and S. Ramaprabhu. A Raman spectroscopic investigation of graphite oxide derived graphene. AIP Advances. 2 (2012) 0132183.

[6] G. Dresselhaus, and M. S. Dresselhaus. Raman spectroscopy in graphene related systems. Wiley-VCH. 2011

[7] Q. Xue, J. Li, P. P. Huang, X. R. Liu, Z. Y. Yang, D. Wang, W. G. Song, D. W. Yan, and Z. J. Gu. Catalytic performance of Pt/reduced graphene oxide composites to methanol electrochemical oxidation: Optimization of mass-specific activity. Journal of Nanoscience and Nanotechnology. 15 (2015) 6628.

[8] A. Sadezky, H. Muckenhuber, H. Grothe, R. Niessner, and U. Pöschl. Raman microspectroscopy of soot and related carbonaceous materials: Spectral analysis and structural information. Carbon. 43 (2005) 1731.

[9] V. N. Tsaneva, W. Kwapinski, X. Teng, and B. A. Glowacki. Assessment of the structural evolution of carbons from microwave plasma natural gas reforming and biomass pyrolysis using Raman spectroscopy. Carbon. 80 (2014) 617.

[10] R. Brunetto, J. Borg, E. Dartois, F. J. M. Rietmeijer, F. Grossemy, C. Sandt, L. Le Sergeant, A. Rotundi, P. Dumas, Z. Djouadi, and F. Jamme. Mid-IR, far-IR, Raman micro-spectroscopy, and FESEM-EDX study of IDP L2021C5 : Clues to its origin. Icarus. 212 (2012) 896.

[11] B. Manoj. Investigation of nanocrystalline structure in selected carbonaceous materials. International Journal of Minerals, Metallurgy and Materials. 21 (2014) 940.

[12] A. N. Mohan, A. V. Ramya, and B. Manoj. Synthesis and characterization of sp^2-sp^3 bonded disordered graphene like nanocarbon from coconut shell. Advanced Science, Engineering and Medicine. 8 (2016) 112.

[13] X. Lui, Y. Zheng, Z. Lui, H. Ding, X. Huang, and C. Zheng. Study on the evolution of the char structure during hydrogasification process using Raman spectroscopy. Fuel. 157 (2015) 97.

[14] A. V. Ramya, A. N. Mohan, and B. Manoj. Wrinkled graphene: synthesis and characterization of few layer-like nanocarbons from kerosene. Materials Science-Poland. 34 (2016) 330.

[15] C. D. Elcey, and B. Manoj. Graphitization of coal by bio-solubilization: Structure probe by Raman spectroscopy. Asian Journal of Chemistry. 28 (2016) 1557.

[16] K. Hareesh, B. Shateesh, R. P. Joshi, J. F. Williams, D. M. Phase, S. K. Haram, and S. D. Dhole. Ultra high stable supercpacitance performance of conducting polymer coated MnO_2 nanorods/rGO nanocomposites. RSC Advances. 7 (2017) 20027.

[17] B. Tang, H. Gouxin, and H. Gao. Raman spectroscopic characterization of graphene. Applied Spectroscopy Reviews. 45 (2010) 369.

[18] C. Xu, P. K. Shen, and Y. Liu. Ethanol electrooxidation on Pt/C and Pd/C catalysts promoted with oxide. Journal of Power Sources. 164 (2007) 527.

[19] D. J. Guo, and Z. H. Jing. A novel co-precipitation method for preparation Pt-CeO_2 composites on multi-walled carbon nanotubes for direct methanol fuel cells. Journal of Power Sources. 195 (2010) 3802.

[20] H. Song, X. Qiu, and F. Li. Effect of heat treatment on the performance of TiO_2-Pt-CNT catalysts for methanol electro-oxidation. Electrochimica Acta. 53 (2008) 3708.

[21] Z. Li, Q. Gao, H. Zhang, W. Tian, Y. Tan, W. Qian, and Z. Liu. Low content Pt nanoparticles anchored on N-doped reduced graphene oxide with high and stable electrocatalytic activity for oxygen reduction reaction. Scientific reports. 7 (2017) 43352.

[22] P. Wu, H. Lv, T. Peng, D. He, and S. Mu. Nano conductive ceramic wedged graphene composites as highly efficient metal supports for oxygen reduction. Scientific reports. 4 (2014) 3968.

[23] T. L. Guo, J. G. Li, X. Sun, and Y. Sakka. Photocatalytic growth of Ag nanocrystals on hydrothermally synthesized multiphasic TiO_2/reduced graphene oxide (rGO) nanocoposites and their SERS performance. Applied Surface Science. 423 (2017) 1.

[24] R. Esparza, A. Santoveña, A, Ruiz, A. Ángeles, D. Bahena, J. Maya, J. Ledesma, and R. Pérez. Study of PtPd bimetallic nanoparticle for fuel cell applications. Materials Research. 20 (2017) 1193.

[25] X. Du, S. Luo, H. Du, M. Tang, X. Huang, and P. Kang. Monodisperse and self-assembled Pt-Cu nanoparticles as an efficient electrocatalyst for the methanol oxidation reaction. Journal of Materials Chemistry A. 4 (2016) 1579.

[26] W. Gu, W. Zhang, X. Li, H. Zhu, J. Wei, Z. Li, Q. Shu, C. Wang, K. Wang, W. Shen, F. Kang, and D. Wu. Graphene sheets from worm-like exfoliated graphite. Journal of Materials Chemistry. 19 (2009) 3367.

[27] L. Hawelek, A. Kolano, J. Szade, W. Maziarz, N. Woznica, and A. Burian. The atomic scale structure of nanographene platelets studied by X-ray diffraction, high-resolution transmission electron microscopy and molecular dynamics. Diamond & Related Materials. 35 (2013) 40.

[28] A. Hernández-Ramírez, M. E. Sánchez-Castro, I. Alonso-Lemus, Kalasapurayil Kunhiraman Aruna, Palanisamy Karthikeyan, Ramasamy Monoharan and F. J. Rodríguez-Varela. Evaluation of the nickel titanate-modified Pt nanostructured catalyst for the ORR in alkaline media. Journal of the Electrochemical Society. 163 (2016) F16.

[29] V. Thiagarajan, R. Manoharan, P. Karthikeyan, E. Nikhila, A. Hernández-Ramírez, and F. J. Rodríguez-Varela. Pt nanoparticles supported on $NiTiO_3$/C as electrocatalyst towards high performance methanol oxidation reaction. International Journal of Hydrogen Energy. 42 (2017) 9795.

[30] Z. Yang, C. Li, W. Chen, R. Liu, H. Wei, Y. Ma, S. Meng, S. Hu, and Y. Wei. Preparation and catalytic property of carbon nanotubes supported Pt and Ru nanoparticles for hydrogenation of aldehyde and substituted acetophenone in water. Indian Journal of Chemistry. 56A (2017)1321.

[31] J. R. Croy, S. Mosfata, L. Hickman, H. Heinrich, and B. R. Cuenya. Bimetallic Pt-metal catalysts for the decomposition of methanol: Effect of secondary metal in the oxidation state, activity, selectivity of Pt. Applied Catalysis A: General. 350 (2008) 207.

[32] A. Eguizabal, L. Uson, V. Sebastian, J. L Hueso, and M. P Pina. Efficient and facile tuning of Vulcan XC-72 with ultra-small Pt nanoparticles for electrocatalytic applications. RSC Advances. 5 (2015) 90691.

[33] Z. Bo, X. Shuai, S. Mao, H. Yang, J. Qian, J, Chen, J. Yan, and K. Cen. Green preparation of reduced graphene oxide for sensing and energy storage applications. Scientific Reports. 4 (2014) 4684.

[34] Z. Yang, N. Zhang, Y. Li, Y. Liao, Y. Li, M. Gong, and Y. Chen. Promotional effect of lanthana on the high-temperature thermal stability of Pt/TiO2 sulfur-resistant diesel oxidation catalysts. RSC Advances. 7 (2017) 19318.

[35] C. Ren, L. Zhou, Y. Duan, and Y. Chen. Synergetic effect of thermo-photocatalytic oxidation of benzene on Pt-TiO_2/Ce-MnO_x. Journal of Rare Earths. 30 (2012) 1106.

[36] J. C. Dupin, D. Gonbeau, P. Vinatier, and A. Levasseur. Systematic XPS studies of metal oxides, hydroxides and peroxides. Physical Chemistry Chemical Physics. 2 (2000) 1319.

[37] H. Takahashi, M. Sagihara, and M. Taguchi. Electrochemically reduced Pt oxide thin film as a highly active electrocatalyst for direct ethanol alkaline fuel cell. International Journal of Hydrogen Energy. 39 (2014) 18424.

[38] V. Alderucci, L. Pino, P. L. Antonucci, W. Roh, J. Cho, H. Kim, D. L. Cocke, and V. Antonucci. XPS study of surface oxidation of carbon-supported Pt catalysts. Materials Chemistry and Physics. 41 (1995) 9.

[39] A. A. Siller-Ceniceros, M. E. Sánchez-Castro, D. Morales-Acosta, J. R. Torres-Lubián, E. Martínez, F. J. Rodríguez-Varela. Innovative functionalization of Vulcan XC-72 with Ru organometallic complex: Significant enhancement in catalytic activity of Pt/C electrocatalyst for the methanol oxidation reaction (MOR). Applied Catalysis B: Environmental. 209 (2017) 455.

[40] H. Wu, T. Peng, Z. Kou, J. Zhang, K. Chen, D. He, M. Pan, and S. Mu. Core-shell graphene@amorphous carbon composites supported platinum catalysts for oxygen reduction reaction. Chinese Journal of Catalysts. 36 (2015) 490.

[41] J. Zhu, D. Yang, Z. Ying, Q. Yan, and H. Zhang. Graphene and graphene-based materials for energy storage applications. Small. 10 (2014) 3480.

[42] M. Shao, P. Liu, and R. R. Adzic. Superoxide anion is the intermediate in the oxygen reduction reaction on platinum electrodes. Journal of the American Chemical Society. 128 (2006) 7408.

[43] J. Zang. PEM Fuel Cell Electrocatalysis and Catalyst Layers. Springer. Canasá. 2008.

[44] C. He, H. R. Kunz, and J. M. Fenton. Evaluation of platinum-based catalysts for methanol electro-oxidation in phosphoric acid electrolyte. Journal of the Electrochemical Society. 144 (1997) 970.

[45] E. J. Coleman, M. H. Chowdhury, and A. C. Co. Insights into the oxygen reduction reaction activity of Pt/C and PtCu/C catalysts. ACS Catalysis. 5 (2015) 1245.

[46] J. Perez, E. R. González, and E. A. Ticianelli. Oxygen electrocatalysis on thin porous coating rotating platinum electrodes. Electrochimica Acta. 44 (1998) 1329.

[47] S. Gupta, L. Qiao, S. Zhao, H. Xe, Y. Li, S. V. Devaguptapu, X. Wang, M. T. Swihart, and G. Wu. Highly active and stable graphene tubes decorated with FeCoNi alloy nanoparticles via a template-free graphitization for bifunctional oxygen reduction and evolution. Advanced Energy Materials. 6 (2016) 1601198.

[48] K. L. Hsueh, E. R. González, and S. Srinvasan. Effects of phosphoric acid concentration on oxygen reduction kinetics at platinum. Journal of Electrochemical Society: Electrochemical Science and Technology. 131 (1984) 823.

[49] S. M. Park, S. Ho, S. Aruliah, M. F. Weber, C. A. Ward, R. D. Venter, and S. Srinivasan. Electrochemical reduction of oxygen at platinum electrodes in KOH solutions – Temperature and concentration effects. Journal of the Electrochemical Society. 133 (1986) 1641.

[50] N. Alexeyeva, K. Tammeveski, A. Lopez-Cudero, J. Solla-Gullón, and J. M. Feliu. Electroreduction of oxygen on Pt nanoparticle/carbon nanotube nanocomposites in acid and alkaline solutions. Electrochimica Acta. 55 (2010) 794.

[51] K. Tammeveski, T. Tenno, J. Claret, and C. Ferrater. Electrochemical reduction of oxygen on thin-film Pt electrodes in 0.1 M KOH. Electrochimica Acta. 42 (1997) 893.

[52] J. Perez, E. R. González, and E. A. Ticianelli. Oxygen electrocatalysis on thin porous coating rotating platinum electrodes. Electrochimica Acta. 44 (1998) 1329.

[53] Z. S. Wu, S. Yang, Y. Sunt, K. Paravez, X. Feng, and K. Mullen. 3D nitrogen-doped aerogel-supported Fe_3O_4 nanoparticles as efficient electrocatalysts for the oxygen reduction reaction. Journal of the American Chemical Society. 134 (2012) 9082.

[54] K. Niu, B. Yang, J. Cui, J. Jin, X. Fu, Q. Zhao, and J. Zhang. Graphene-based non-noble-metal Co/N/C catalyst for oxygen reduction reaction in alkaline solution. Journal of Power Sources. 243 (2013) 65.

[55] H. A. Alessandro, V. Monteverde, S. Ban, S. Speecchia, L. Zhang, and J. Zhang. Non-noble Fe-N_x electrocatalysts supported on the reduced graphene oxide for oxygen reduction reaction. Carbon. 76 (2014) 386.

[56] C. He, J. J. Zhang, and P. K. Shen. Nitrogen self-doped-graphene-based non-precious metal catalyst with superior performance to Pt/C catalyst toward oxygen reduction reaction. Journal of Materials Chemistry A. 9 (2014) 3231.

[57] H. Yang, N. Alonso-Vante, J. M. Láger, and C. Lamy. Tailoring, structure and activity of carbon-supported nanosized Pt-Cr alloy electrocatalysts for oxygen reduction reaction in pure and methanol-containing electrolytes. The Journal of Physical Chemistry B. 108 (2004) 1938.

[58] H. Zhang, Q. Hao, H. Geng, and C. Xu. Nanoporous PdCu alloys as highly active and methanol-tolerant oxygen reduction electrocatalysts. International Journal of Hydrogen Energy. 38 (2013) 10029.

[59] R. N. Singh, R. Awasthi, and C. S. Sharma. Review: An overview or recent development of platinum-based cathode materials for direct methanol fuel cells. International Journal of Electrochemical Science. 9 (2014) 5607.

[60] J. Yang, W. Zhou, C. H. Cheng, J. Y. Lee, and Z. Liu. Pt-decorated PdFe nanoparticles as methanol-tolerant oxygen reduction electrocatalyst. Applied Materials and Interfaces. 2 (2010) 119.

[61] E. Antolini, J. C. R. Salgado, L.G. R. A. Santos, G. García, E. A. Ticianelli. E. Pastor, and E. R. González. Carbon supported Pt-Cr alloys as oxygen-reduction catalysts for direct methanol fuel cells. Journal of Applied Electrochemistry. 36 (2006) 355.

Chapter VIII

rGO functionalized with chromium organometallic compounds as a novel support for highly active Pt-$CoTiO_3$ catalyst for the Oxygen Reduction Reaction

8.1 rGO functionalized with Cr organometallic compounds. Structural and morphological features.

8.1.1 Vibrational spectra analysis by FTIR.

Figure 8.1 shows the FTIR spectra of the $Cr(CO)_6$ and $[(\eta^6\text{-}C_6H_6)Cr(CO)_3]$ organometallic precursors (labeled as Cr-hexac and Cr-bz, respectively). Strong adsorption peaks at 1864 and 1808 cm^{-1} due to the C≡O antisymmetric stretching vibrations are observed, while the lower intensity bands at 1963 and 1945 cm^{-1} are attributed to symmetric stretching vibrations of C≡O. It is known that free C≡O has a stretching frequency of ~2143 cm^{-1}. The shift in the stretching frequency of the Cr-hexac and Cr-bz can be explained as follows: when C≡O ligands bond to a transition metal, the back donation of electron density from the metal to the carbonyl empty orbital causes an increase in bond order and therefore a shift in stretching frequency of C≡O occurs, as observed in Figure 8.1.[1-4]

The intense bands at 628 and 619 cm^{-1} of the Cr-hexac and Cr-bz organometallics, respectively correspond to the M-C≡O bending vibration. The overtone and combination bands of the M-C stretching and M-C≡O bending modes are observed in the infrared spectrum of the Cr-hexac compound (Figure 8.1a) in the 877-1190 cm^{-1} region.[5,6] Similar bands in the 902-1147 cm^{-}

[1] interval are identified for Cr-bz (Figure 8.1b). Also, in the Cr-bz compound, the aromatic structure is recognized by the presence of: i) the -CH stretching and bending vibrations at 3105 and 781 cm^{-1}, and ii) the ring breathing vibrations at 1444 cm^{-1}.[7,8] The corresponding chemical structures of the Cr-hexac and Cr-bz organometallics are visualized in the insets of Figure 8.1.

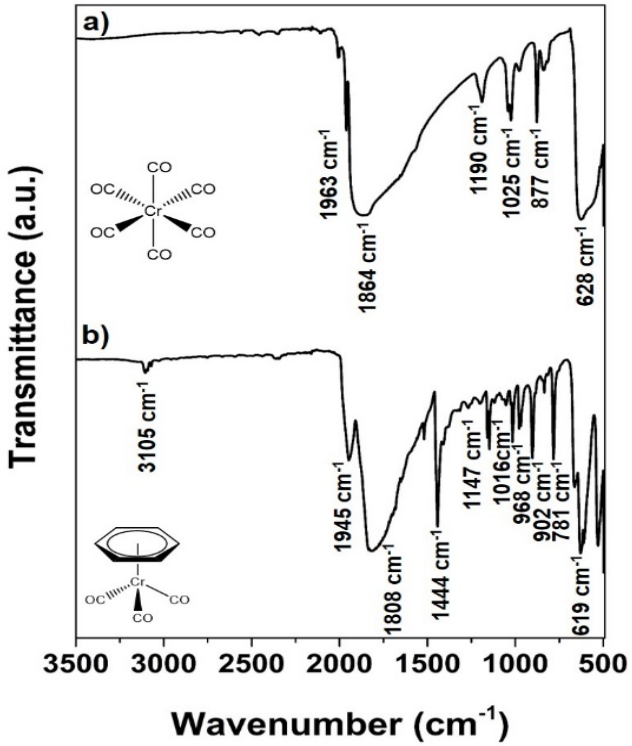

Figure 8.1 FTIR spectra of the chromium organometallic compounds: a) Cr-hexac and b) Cr-bz.

The FTIR spectrum of the complexation reaction of rGO with 0.22 mmol of Cr-hexac (Figure 8.2a) shows the appearance of an absorption peak at 1768 and 1073 cm^{-1} due to the stretching vibrations of the C≡O functional groups and M-C≡O vibration modes, respectively. As already mentioned above, the IR frequency of the carbonyl groups is sensitive to the electronic effect of the substituent ligand. Therefore, a decrease in the CO stretching frequency is observed (compared to Cr-hexac in Figure 8.1a).

Since a mild heating of the organometallic causes the elimination of carbonyl groups, benzene (and its derivatives) may react to displace three donor ligands.[9-11] The formation of a hexahapto metal bond between the graphitic lattice and the organometallic compound its viable, giving a complex of formula $[(\eta^6\text{-rGO})Cr(CO)_3]$ (schematized in Figure 8.3a and labeled as rGO-Cr_{tric}).

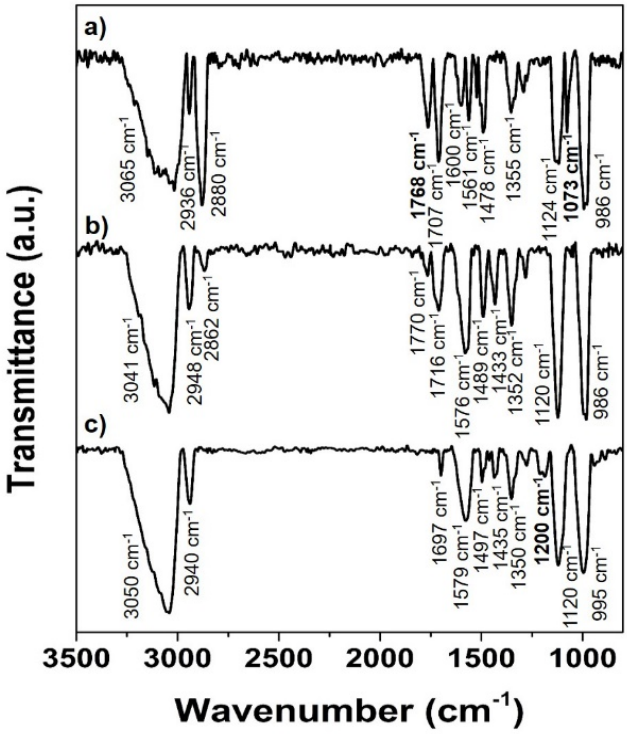

Figure 8.2 FTIR spectra of the functionalized rGO supports: a) rGO-Cr_{tric}, b) rGO_2Cr and c) rGO-Cr_{bz}.

The FTIR spectrum of the reaction of rGO with 0.04 mmol of Cr-hexac is presented in Figure 8.2b. The weak peak at 1770 cm^{-1} can be attributed to C≡O vibrations. Nevertheless, the M-C≡O are not identified (as can be seen at RGO-Cr_{tric}). According to this finding, it can be suggested that chromium atoms preferentially bond covalently with two benzene rings of the interlayered rGO surface forming a bis-hexahapto complex assigned as $[(\eta^6\text{-rGO})_2Cr]$ (schematized in Figure 8.3b and labeled as rGO_2Cr). The variation of the

structure as a function of the chromium organometallic compound stoichiometry, agrees well with those reported for molecular chromium complexes.[12,13]

Figure 8.2c shows the FTIR spectrum of the reaction of rGO with the Cr-bz organometallic compound. Haddon *et. al*[12] have indicated that the aromatic -CH stretching vibrations at ~3100 cm^{-1} as the main evidence of the formation of the [(η^6-RGO)Cr(η^6-C_6H_6)] product. Nevertheless, in this experimentation is observed that since the -OH stretching signals from rGO appear in this frequency range, the -CH stretching vibrations of benzene could not observed. Despite this fact, the peak located at ~1200 cm^{-1} can be associated with the in plane –CH bending vibrations in the aromatic ring.

Also, as a result of the absence of the characteristic CO stretching vibrations in the FTIR spectrum, it can be inferred that the benzoic unit and the metallic atom coordinates with the rGO surface given the [(η^6-RGO)Cr(η^6-C_6H_6)] complex (from now on referenced as rGO-Cr$_{bz}$ and schematized in Figure 8.3c). It is worth mentioning that in all complexation reactions, the functionalized rGO supports are electronically stable since the zerovalent chromium atom possesses six valence shell electrons and, by complexation with one or two n^6-benzoid ligands, achieves an 18-electron configuration.[14]

Furthermore, the infrared vibrations of rGO are also identified: the aromatic stretching vibrations of hybridized sp^2 C=C bonds in the region of 1570-1430 cm^{-1} and the absorption peaks localized in the 2950-2860 cm^{-1} region associated to the symmetric/anti-symmetric vibrations of -CH_2 groups. The O-H stretching vibrations peaks are observed at 3065, 3041 and 3050 cm^{-1} on rGO-Cr$_{tric}$, rGO$_2$Cr and rGO-Cr$_{bz}$, respectively. Meanwhile, the peaks at 1355, 1352 and 1350 cm^{-1} correspond to the O-H bending vibrations. Carboxy (C=O), epoxy and alcoxy (C-O) functional groups are observed by the absorption

peaks in the 1697-1716, 1120-1124 and 995-986 cm^{-1} regions in rGO-Cr$_{tric}$, rGO$_2$Cr and rGO-Cr$_{bz}$, respectively.[15-18]

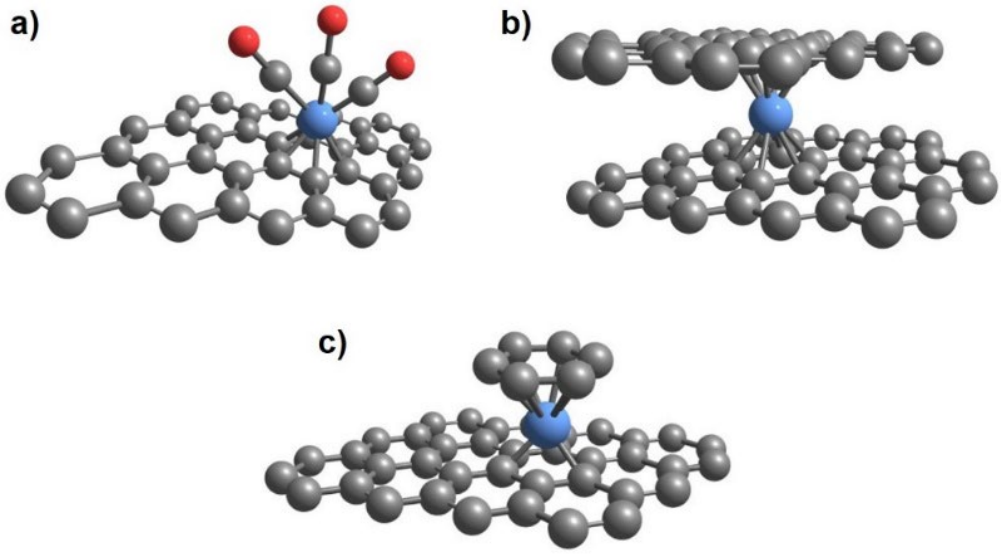

Figure 8.3 Schematic representation of the rGO functionalized products: a) rGO-Cr$_{tric}$, b) rGO$_2$Cr and c) rGO-Cr$_{bz}$.

8.1.2 Raman spectroscopy characterization.

The Raman spectra of rGO-Cr$_{tric}$, rGO$_2$Cr and rGO-Cr$_{bz}$ are shown in Figure 8.4. The functionalized supports have the characteristic structure of graphitic materials having two prominent peaks attributed to the D and G bands (sp^3 and sp^2 domains, respectively). The spectra also show other signals such as I, D´´, D´, D+D´´, 2D, D+D´ (D+G) and 2D´.

The I_D/I_G ratios of rGO-Cr$_{tric}$ and rGO$_2$Cr are 0.74 and 0.84, respectively (Figures 8.4a and 6.4b), lower compared to non-functionalized RGO (1.2, Figure 7.1 in Chapter VII). Such decrease is attributed to a change in the electronic structure of rGO associated to chromium complexation, which results in an increase in the G band (sp^2-domains). Thus, the graphitic band structure of rGO-Cr$_{tric}$ and rGO$_2$Cr become more intense compared to rGO (i. e., the

more structural order). Meanwhile, the I_D/I_G ratio of rGO-Cr$_{bz}$ is 1.2, the same as non-functionalized rGO. This outcome shows that functionalization with Cr-bz has no effect on the graphitized lattice of the rGO, an indication that the hybridization and structure of the rGO is preserved (Figure 8.4c).

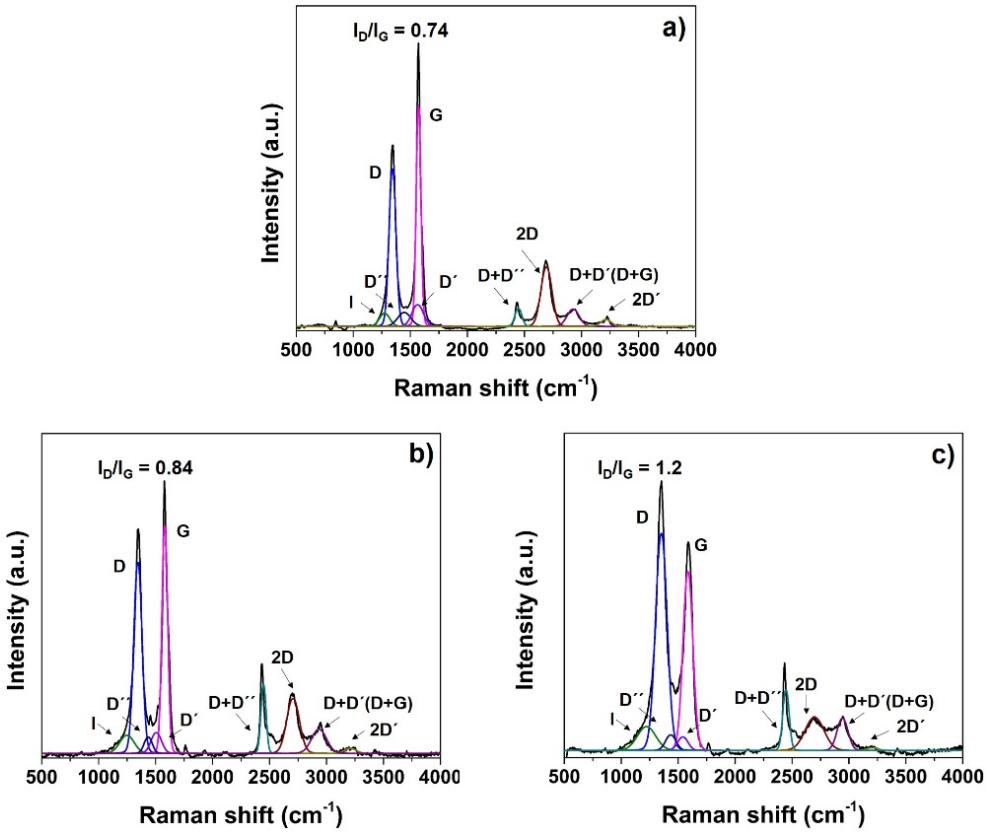

Figure 8.4 Raman spectra of: a) rGO-Cr$_{tric}$, b) rGO$_2$Cr and c) rGO-Cr$_{bz}$.

8.1.3 X-Ray diffraction analysis (XRD).

Figure 8.5 shows the XRD patterns of non-functionalized rGO, and those of rGO-Cr$_{tric}$, rGO$_2$Cr and rGO-Cr$_{bz}$. The broad peaks around 26.2 and 43° (2θ) correspond to the (002) and (100) planes, respectively, of graphene structures, as previously reported.[19-22] The position of the (002) crystallographic orientation can be correlated with the distance between the stacked graphitic layers (*d*-spacing). With the aid of Bragg´s law (λ = 2dsenθ) the estimated *d*-

spacing of the rGO is 0.340 nm, in good agreement with the thickness of pristine graphene nanosheets.[22-24] The functionalized rGO supports have almost the same value of interlayer distance with values of 0.341, 0.342 and 0.342 nm for rGO-Cr_{tric}, rGO$_2$Cr and rGO-Cr_{bz}, respectively. Therefore, the incorporation of the organometallic molecules into the carbon structure has a negligible effect on the graphene layers structure.

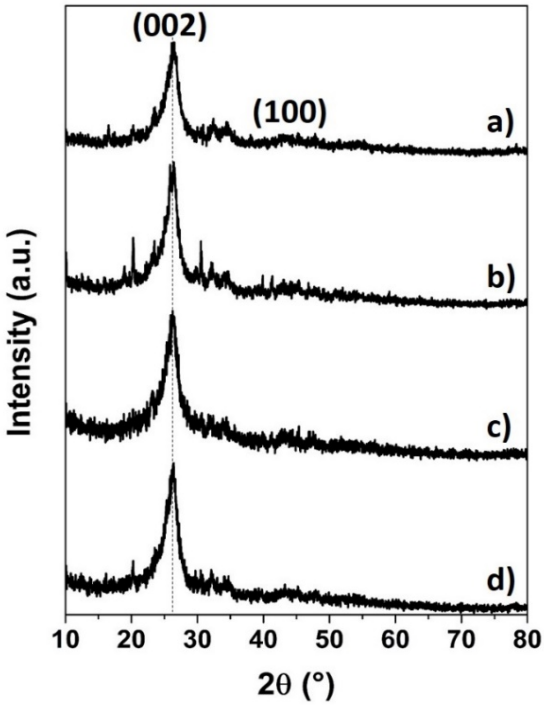

Figure 8.5 XRD patterns of: a) non-functionalized rGO, b) rGO-Cr_{tric}, c) rGO$_2$Cr and d) rGO-Cr_{bz}.

8.1.4 SEM/EDS characterization.

The morphology of the functionalized rGO-Cr_{tric}, rGO$_2$Cr and rGO-Cr_{bz} supports is shown in the SEM images of Figure 8.6. Layered surfaces characteristic of graphene-based materials can be visualized, with wrinkles in all cases. The insets are chemical mappings of the rGO. Overall, it can be observed that Cr

atoms have a uniform dispersion over the rGO sheets, confirming its functionalization with metallic Cr sites.

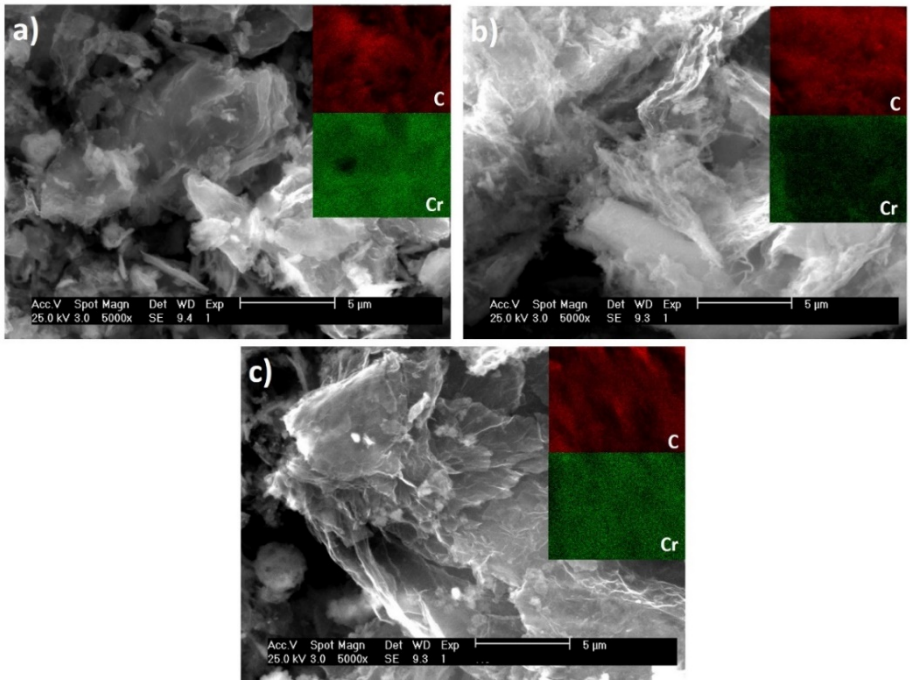

Figure 8.6 SEM images and mapping of element distribution of: a) rGO-Cr_{tric}, b) rGO_2Cr and c) rGO-Cr_{bz}.

In order to estimate the amount of Cr in the functionalized supports, EDS elemental analysis has been performed and the atomic percentages are summarized in Table 8.1. The highest Cr concentration is that of rGO-Cr_{tric} (8.4 at.%). rGO_2Cr and rGO-Cr_{bz} contain roughly 40% of that amount of Cr. Nevertheless, it should be reminded that rGO-Cr_{tric} has been functionalized with 0.22 mmol of Cr-hexac, while rGO_2Cr has been modified with 0.04 mmol of Cr-hexac. Therefore, caution must be taken when analyzing the results in Table 8.1.

Table 8.1. Chemical composition quantified by EDS of the rGO-Cr_{tric}, rGO_2Cr and rGO-Cr_{bz} supports.

	Chemical composition (at. %)	
	C	**Cr**
rGO-Cr_{tric}	91.6 ± 0.75	8.4 ± 0.75
rGO_2Cr	96.3 ± 0.58	3.7 ± 0.58
rGO-Cr_{bz}	96.7 ± 0.45	3.3 ± 0.45

8.2 Structural, morphological and surface chemistry features of the Pt-$CoTiO_3$/rGO-Cr_{tric}, Pt-$CoTiO_3$/rGO_2Cr and Pt-$CoTiO_3$/rGO-Cr_{bz} catalysts.

8.2.1 X-Ray diffraction analysis (XRD).

The diffraction patterns of the Pt-$CoTiO_3$/rGO (non-functionalized rGO), Pt-$CoTiO_3$/rGO-Cr_{tric}, Pt-$CoTiO_3$/rGO_2Cr and Pt-$CoTiO_3$/rGO-Cr_{bz} catalysts in Figure 8.7 exhibit the peaks indexed to the (111), (200), (220) and (311) crystallographic planes of the face-centered cubic structure of Pt. The peak at around 26° (2θ) is due to the carbon support and is attributed to the (002) crystalline plane of the graphite structure. Besides, some reflections of the $CoTiO_3$ phase have been identified (indicated by bullets).

It is noticed that there is no significant shift of the diffraction peaks of rGO-Cr_{tric}, rGO_2Cr and rGO-Cr_{bz} (compared to the Pt-$CoTiO_3$/rGO catalyst). Such feature suggests that the presence of Cr metallic sites from the functionalization process has no effect on the crystalline lattice of Pt (i. e., there is no evidence of formation of Pt-Cr alloyed phases).

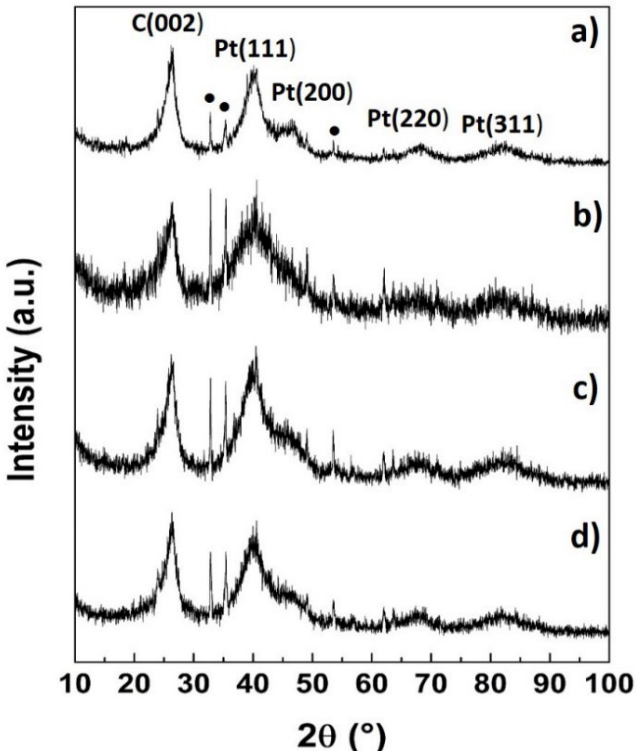

Figure 8.7 X-ray diffraction patterns of: a) Pt-$CoTiO_3$/rGO, b) Pt-$CoTiO_3$/rGO-Cr_{tric}, c) Pt-$CoTiO_3$/rGO_2Cr and d) Pt-$CoTiO_3$/rGO-Cr_{bz} catalysts. The bullets indicate the diffraction peaks corresponding to the $CoTiO_3$ phase.

8.2.2 SEM/EDS characterization.

Table 8.2 summarizes the elemental composition of the Pt-$CoTiO_3$/rGO, Pt-$CoTiO_3$/rGO-Cr_{tric}, Pt-$CoTiO_3$/rGO_2Cr and Pt-$CoTiO_3$/rGO-Cr_{bz} catalysts. In all cases, the amount of Pt-$CoTiO_3$ is higher than the 20 at. % expected. Also, the carbon content is lower. Moreover, Cr in several concentrations (the highest at Pt-$CoTiO_3$/rGO-$Cr_{tric,}$ in agreement with Table 8.1) has been determined. These features can be attributed to be functionalization of rGO with Cr organometallic compounds and the presence of the titanante (see chemical composition of Pt-$CoTiO_3$/rGO). Meanwhile, the Pt:$CoTiO_3$ ratio is in reasonable agreement with the nominal one (i.e., 1:1).

Table 8.2. Chemical composition and particle size of the Pt-CoTiO$_3$/rGO-Cr$_{tric}$, Pt-CoTiO$_3$/rGO$_2$Cr and Pt-CoTiO$_3$/rGO-Cr$_{bz}$ catalysts.

	Chemical composition (wt. %)				Pt:CoTiO$_3$ (at. %)	Particle size $_{TEM}$ (nm)
	Pt	**CoTiO$_3$**	**C**	**Cr**		
Pt-CoTiO$_3$/rGO	21.05 ± 1.34	12.17 ± 1.07	66.97 ± 1.40	-	1:0.72	2.0
Pt-CoTiO$_3$rGO-Cr$_{tric}$	18.04 ± 0.50	10.86 ± 1.19	68.01 ± 1.23	3.07 ± 1.07	1:0.75	1.9
Pt-CoTiO$_3$/rGO$_2$Cr	21.64 ± 1.90	7.33 ± 0.37	69.85 ± 1.91	1.57 ± 0.26	1:0.83	2.4
Pt-CoTiO$_3$/rGO-Cr$_{bz}$	19.01 ± 0.88	10.81 ± 0.39	67.38 ± 1.16	2.78 ± 0.06	1:0.71	2.3

8.2.3 HR-TEM analysis.

The HR-TEM analysis of Pt-CoTiO$_3$/rGO has been introduced in Chapter VII. Figure 8.8a) shows a HR-TEM image of Pt-CoTiO$_3$/rGO-Cr$_{tric}$ revealing a morphology with homogeneous dispersion of nanoparticles over the support. The average particle size is around 1.9 nm (Table 8.2). Selected Area Electron Diffraction (SAED) evaluation has been made of this catalyst. The FFT analysis performed on solid-line square give the SAED pattern shown as inset in Figure 8.8b). Then, from such pattern the reconstructed iFFT image showing the distance between fringes (Figure 8.8b) is obtained. An interplanar distance of 0.22 nm has been determined, ascribed to Pt (111) plane. Similarly, FFT analysis of the dashed-line square resulted in the SAED pattern (inset in Figure 6.8c), from which the reconstructured iFFT image (Figure 8.8c) is obtained. An interplanar distance of 0.36 nm has been determined, corresponding to the CoTiO$_3$ (211) plane.

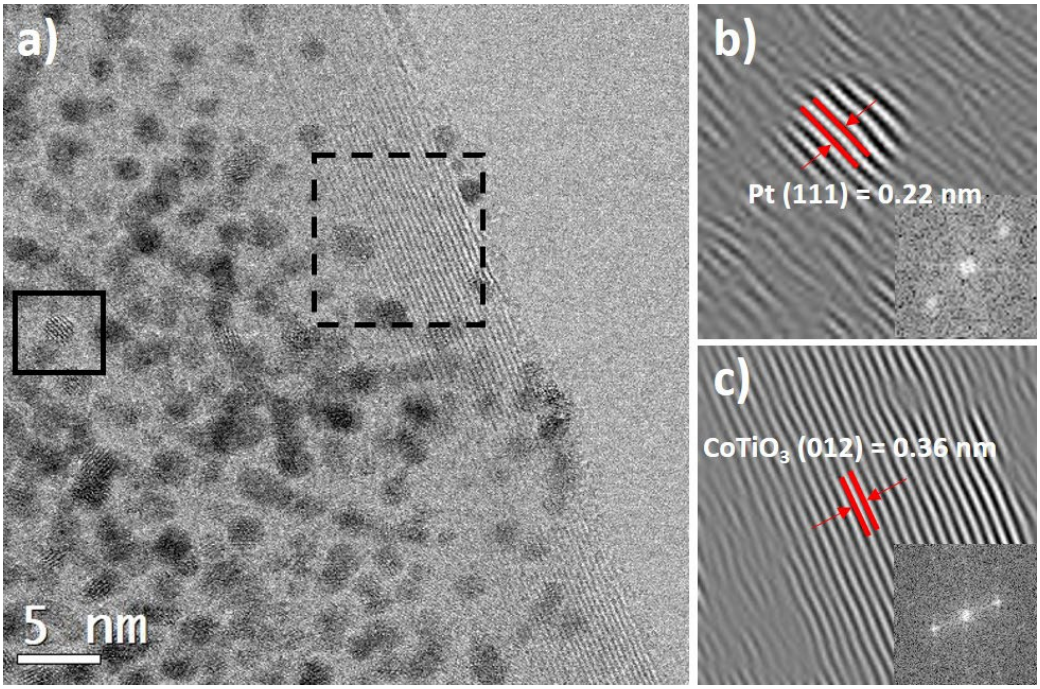

Figure 8.8 a) HR-TEM micrograph of Pt-$CoTiO_3$/rGO-Cr_{tric}, b) Reconstructured iFFT image from the SAED pattern (inset), which in turn has been obtained from the solid-line square in a). c) Reconstructured iFFT image from the SAED pattern (inset), which in turn has been obtained from the dashed line-square in a).

The HR-TEM image of the Pt-$CoTiO_3$/rGO_2Cr catalyst (Figure 8.9a) shows the nanostructured nature of the Pt nanoparticles, having an average particle size of 2.4 nm (Table 8.2). From the solid and dashed-line squares, SAED patterns are shown as insets in b) and c), respectively, leading to the reconstructured iFFT images 8.9b) and 8.9c). Lattice fringes of 0.22 and 0.35 nm have been measured, corresponding to Pt (111) and $CoTiO_3$ (211) planes, respectively.

In the HR-TEM image of the Pt-$CoTiO_3$/rGO-Cr_{bz} catalyst (in Figure 8.10a), the Pt nanoparticles have an average particle size of 2.3 nm (Table 8.2). The analysis has been performed as described in Figures 8.8 and 8.9. Interplanar distances of 0.22 and 0.36 nm have been measured at Figures 8.10b) and c), respectively, also corresponding to Pt(111) and $CoTiO_3$ (211).

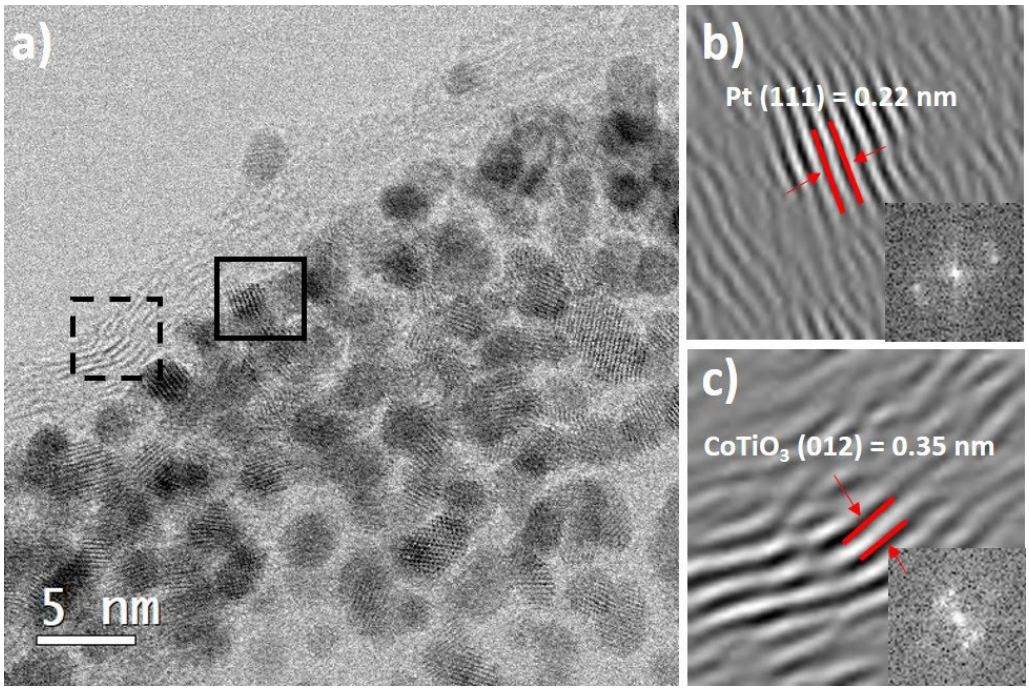

Figure 8.9 a) HR-TEM micrograph of Pt-$CoTiO_3$/rGO_2Cr, b) Reconstructured iFFT image from the SAED pattern (inset), which in turn has been obtained from the solid-line square in a). c) Reconstructured iFFT image from the SAED pattern (inset), which in turn has been obtained from the dashed line-square in a).

The HR-TEM analysis performed on the Pt-$CoTiO_3$/rGO-Cr_{tric}, Pt-$CoTiO_3$/rGO_2Cr and Pt-$CoTiO_3$/rGO-Cr_{bz} catalysts gives also evidence that some Pt nanoparticles are supported both on rGO and titanate sites, as previously proposed for the similar Pt-$NiTiO_3$ catalyst.[25]

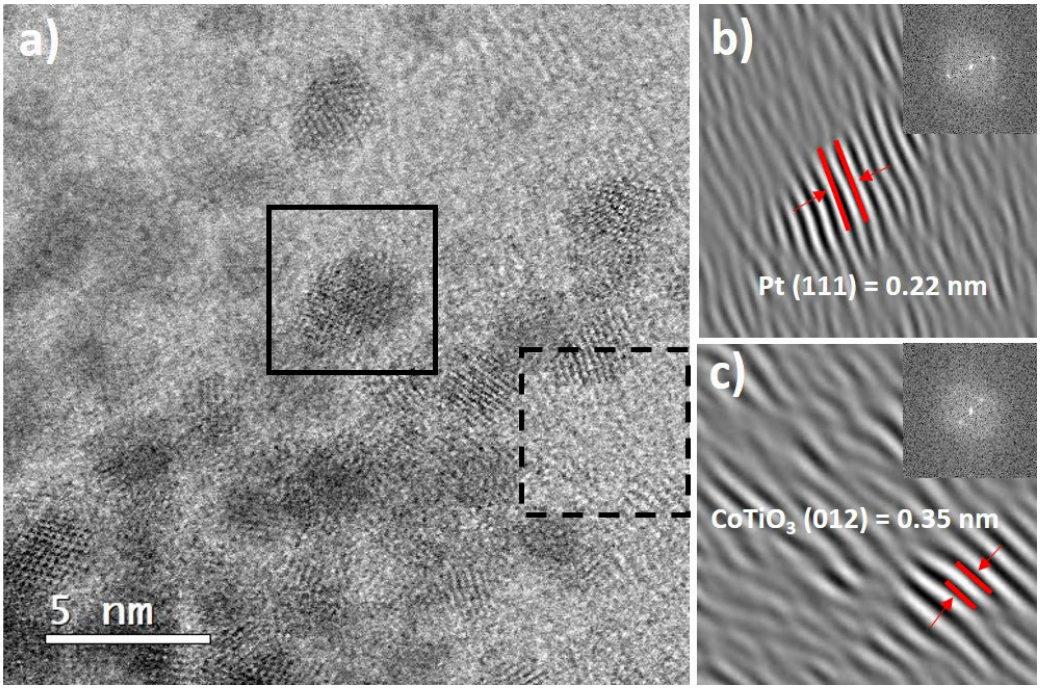

Figure 8.10 a) HR-TEM micrograph of Pt-$CoTiO_3$/rGO-Cr_{bz}, b) Reconstructured iFFT image from the SAED pattern (inset), which in turn has been obtained from the solid-line square in a). c) Reconstructured iFFT image from the SAED pattern (inset), which in turn has been obtained from the dashed line-square in a).

8.2.4 Chemical surface analysis by XPS.

The deconvoluted high resolution Pt 4f spectra of the catalysts show doublets due to the spin-orbit splitting of $Pt4f_{7/2}$ and $Pt4f_{5/2}$. The signals at binding energies (BEs) of 71.8 and 75.1 eV (Pt-$CoTiO_3$/rGO-Cr_{tric}), 71.6 and 75 eV for Pt-$CoTiO_3$/rGO_2Cr and Pt-$CoTiO_3$/rGO-Cr_{bz} are attributed to the Pt^0 oxidation state (Figure 8.11). The two other doublets are ascribed to the Pt^{2+} and Pt^{4+} species (the BEs of the different Pt species are given in Table 8.3). Compared to Pt-$CoTiO_3$/rGO (BE= 71.4 eV, Table 7.2, Chapter VII), the Pt^0 peak in the Pt $4f_{7/2}$ region shifts by 0.4 eV towards higher BEs at Pt-$CoTiO_3$/rGO-Cr_{tric}, while the displacement is of 0.2 eV at Pt-$CoTiO_3$/rGO_2Cr and Pt-$CoTiO_3$/rGO-Cr_{bz}.

The shift in BE can be attributed to a change in the electronic state of Pt (*d*-valence band) due to an electron transfer from Cr to Pt atoms.

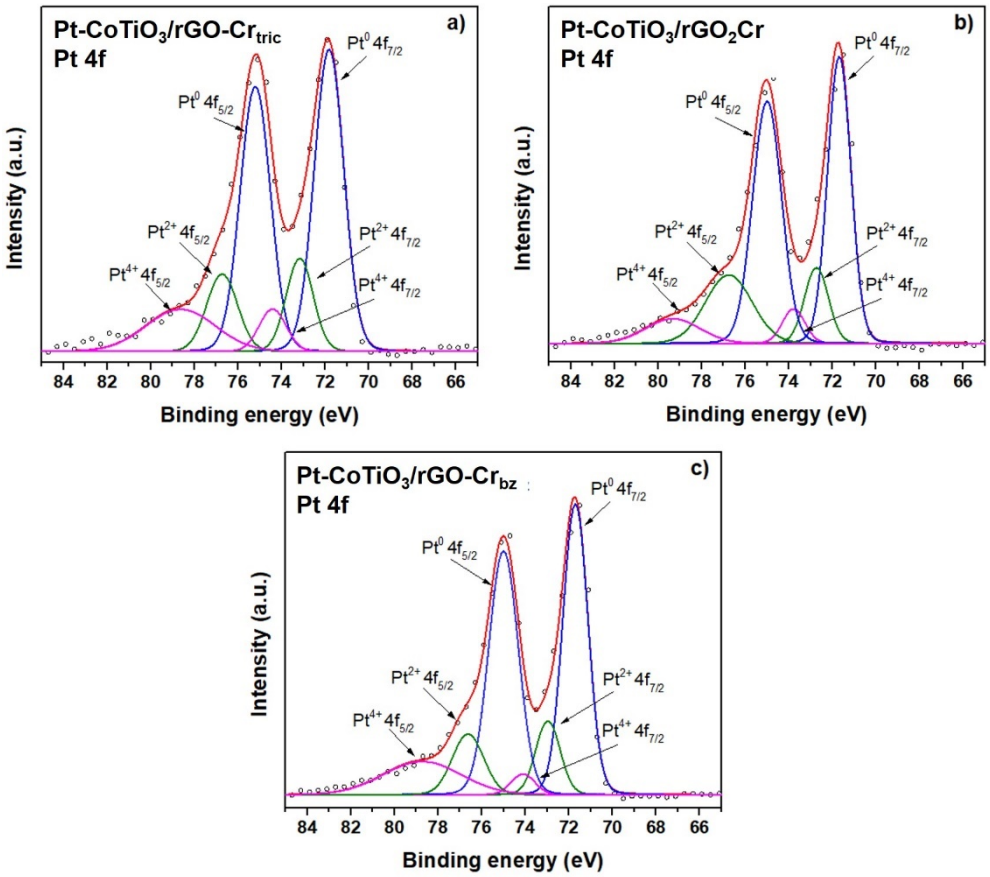

Figure 8.11 Pt 4f core level spectra of: a) Pt-$CoTiO_3$/rGO-Cr_{tric}, b) Pt-$CoTiO_3$/rGO$_2$Cr and c) Pt-$CoTiO_3$/rGO-Cr_{bz} catalysts.

A similar behavior has been observed previously at a Pt/C_{Rudim}[26] catalyst (Vulcan functionalized with a Ru organometallic compound). It has been reported also for Pt-Cr[27,28], Pt-Mo[29] and Pt-Au[30] alloys. Thus, the electronic modification of Pt at Pt-$CoTiO_3$/rGO-Cr_{tric}, Pt-$CoTiO_3$/rGO$_2$Cr and Pt-$CoTiO_3$/rGO-Cr_{bz} suggests that Pt-Cr alloyed phases have been formed after functionalization of rGO with the Cr organometallic compounds. Meanwhile, the

experimental BEs of the $Pt^{2+}$and Pt^{4+} species are in good agreement with those reported elsewhere.[31-34]

As shown in Figure 8.12, the C 1s core level of the Pt-$CoTiO_3$/rGO-Cr_{tric}, Pt-$CoTiO_3$/rGO_2Cr and Pt-$CoTiO_3$/rGO-Cr_{bz} catalysts exhibit peaks attributed to epoxy/hydroxyl (C-O), carbonyl (C=O) and carboxyl (O-C=O). However, the main contribution is that of the sp^2 hibridization (C=C bonds) at BE = 284 eV (Pt-$CoTiO_3$/rGO-Cr_{tric}) and 284.5 eV (Pt-$CoTiO_3$/rGO_2Cr and Pt-$CoTiO_3$/rGO-Cr_{bz}) with less intense signals due to sp^3 hybridization (Table 8.3). The spectra reveal carbon-metal interactions by the appearance of a signal attributed to C-Cr bonds (see Table 8.3).[35,36]

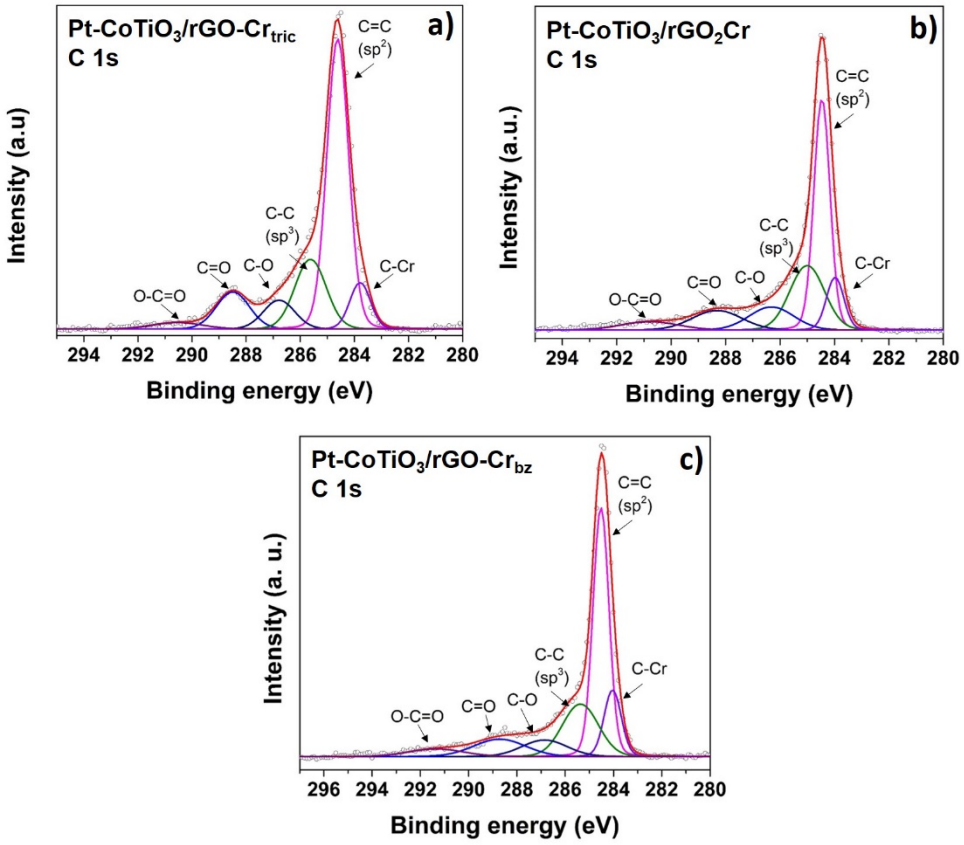

Figure 8.12 C 1s core level spectra of: a) Pt-$CoTiO_3$/rGO-Cr_{tric}, b) Pt-$CoTiO_3$/rGO_2Cr and c) Pt-$CoTiO_3$/rGO-Cr_{bz} catalysts.

Analysis of the Cr 2p core-level spectra (Figure 8.13) allows to evaluate the interactions between Cr (from the organometallics) and rGO. Haddon *et al.* have reported a BE of 576.79 eV for (SWCNT)$Cr(CO)_3$ as being consistent with Cr(0) η^6-complexes.[37] Meanwhile, a BE of 576.1 eV for $(C_6H_6)Cr(CO)_3$ has been also reported.[38] Thus, the signals at 576.2, 576.4 and 576.2 eV (Pt-$CoTiO_3$/rGO-Cr_{tric}, Pt-$CoTiO_3$/rGO_2Cr and Pt-$CoTiO_3$/rGO-Cr_{bz}, respectively, Table 8.3) clearly correspond to the C-Cr bond and emerge due to Cr complexation at the rGO structure. Therefore, the Cr^0 species is formed at the three catalysts. The Cr 2p spectra also indicates the presence of the Cr^{3+} and Cr^{6+} oxidations states (see BEs in Table 8.3), which confirms the existence of the of Cr_2O_3 and CrO_3 species, respectively.[39-41]

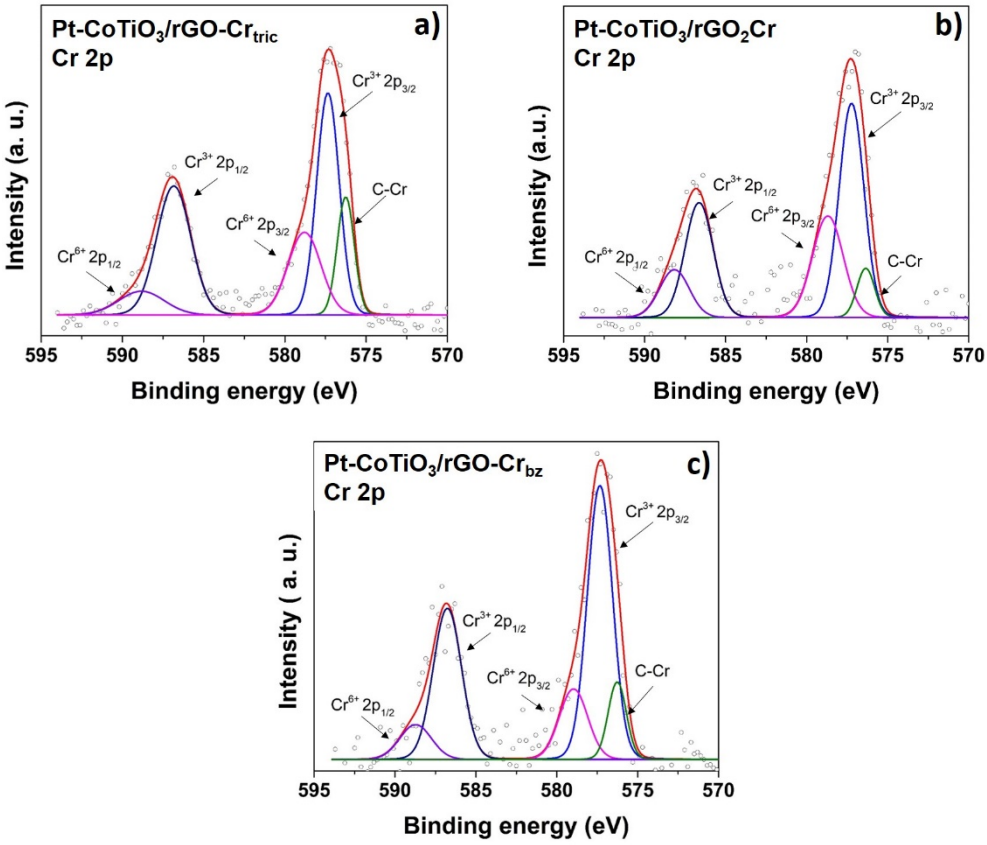

Figure 8.13 Cr 2p core level spectra of: a) Pt-$CoTiO_3$/rGO-Cr_{tric}, b) Pt-$CoTiO_3$/rGO_2Cr and c) Pt-$CoTiO_3$/rGO-Cr_{bz} catalysts.

The oxygen species in the catalysts surface are identified by analyzing the O 1s region spectra (Figure 8.14). The O signal at BEs of ~530, 530.4 and 530.2 eV (Pt-CoTiO$_3$/rGO-Cr$_{tric}$, Pt-CoTiO$_3$/rGO$_2$Cr and Pt-CoTiO$_3$/rGO-Cr$_{bz}$, respectively, Table 8.3) are characteristic of metallic oxides and it may be assigned to metal-oxygen interactions (O^{2-} species) from CoTiO$_3$, Pt-oxides and/or Cr-oxides. The most prominent peak at ~531 eV can be assigned to surface hydroxyl groups, while the signal at ca. 533 eV can be ascribed to the C=O groups from rGO.[42-44]

It is worth mentioning that low-intensity XPS signals of Ni, Co and Ti have also been detected, even though, the spectra is not shown in this work.

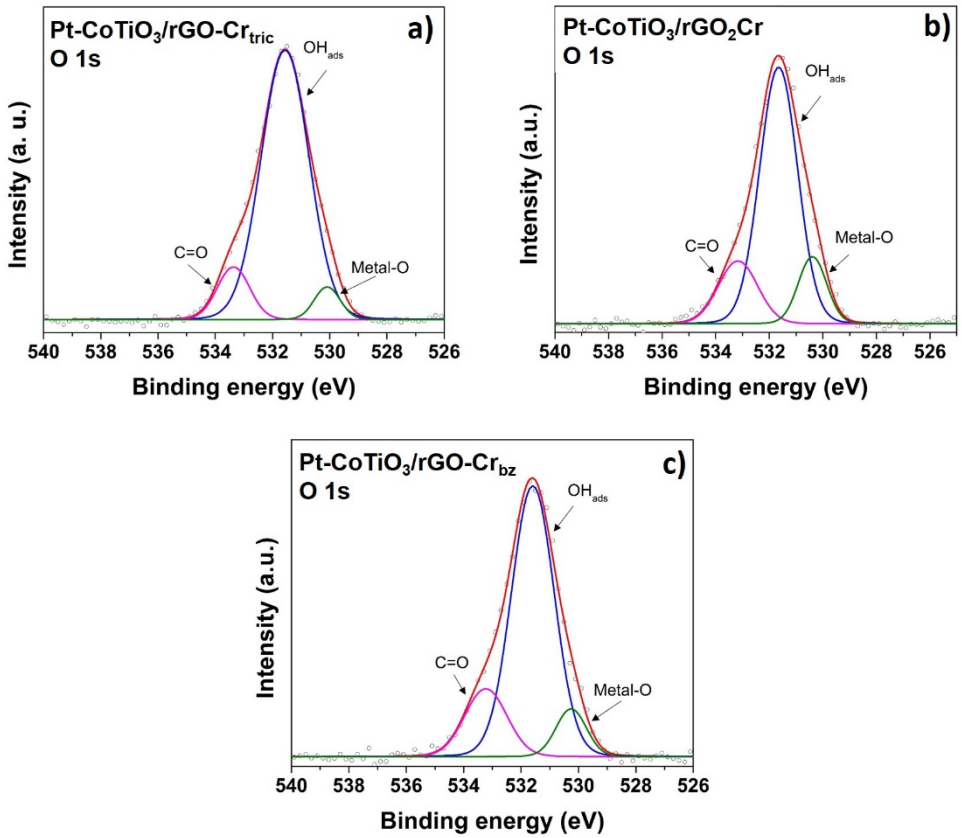

Figure 8.14 O 1s core level spectra of: a) Pt-CoTiO$_3$/rGO-Cr$_{tric}$, b) Pt-CoTiO$_3$/rGO$_2$Cr and c) Pt-CoTiO$_3$/rGO-Cr$_{bz}$ catalysts.

Table 8.3 XPS parameters of Pt-$CoTiO_3$/rGO-Cr_{tric}, Pt-$CoTiO_3$/rGO$_2$Cr and Pt-$CoTiO_3$/rGO-Cr_{bz}.

Catalyst	Species	State	BE (eV)
Pt-$CoTiO_3$/rGO-Cr_{tric}	Pt^0	Pt 4f $_{7/2}$	71.8
		Pt 4f $_{5/2}$	75.1
	PtO	Pt 4f $_{7/2}$	73.2
		Pt 4f $_{5/2}$	76.7
	PtO_2	Pt 4f $_{7/2}$	74.4
		Pt 4f $_{5/2}$	78.6
	C-O	C 1s	286.7
	C=O	C 1s	288.5
	O-C=O	C 1s	290.5
	C=C sp^2	C 1s	284.6
	C-C sp^3	C 1s	285.6
	C-Cr	C 1s	283.7
	Cr^0	C-Cr	576.2
	Cr_2O_3	$2p_{3/2}$	577.2
		$2p_{1/2}$	586.7
	CrO_3	$2p_{3/2}$	578.9
		$2p_{1/2}$	588.7
	Metal-O	O 1s	530.0
	OH_{ads}	O 1s	531.5
	C=O	O 1s	533.4
Pt-$CoTiO_3$/rGO$_2$Cr	Pt^0	Pt 4f $_{7/2}$	71.6
		Pt 4f $_{5/2}$	75.0
	PtO	Pt 4f $_{7/2}$	72.7
		Pt 4f $_{5/2}$	76.8
	PtO_2	Pt 4f $_{7/2}$	73.8
		Pt 4f $_{5/2}$	79.3

	C-O	C 1s	286.2
	C=O	C 1s	288.2
	O-C=O	C 1s	290.7
	C=C sp^2	C 1s	284.5
	C-C sp^3	C 1s	285.0
	C-Cr	C 1s	284.0
	Cr^0	C-Cr	576.4
	Cr_2O_3	$2p_{3/2}$	577.2
		$2p_{1/2}$	586.5
	CrO_3	$2p_{3/2}$	578.7
		$2p_{1/2}$	588.2
	Metal-O	O 1s	530.4
	OH_{ads}	O 1s	531.7
	C=O	O 1s	533.2
Pt-$CoTiO_3$/rGO-Cr_{bz}	Pt^0	Pt 4f $_{7/2}$	71.6
		Pt 4f $_{5/2}$	75.0
	PtO	Pt 4f $_{7/2}$	73.0
		Pt 4f $_{5/2}$	76.6
	PtO_2	Pt 4f $_{7/2}$	74.1
		Pt 4f $_{5/2}$	78.7
	C-O	C 1s	286.8
	C=O	C 1s	288.7
	O-C=O	C 1s	291.2
	C=C sp^2	C 1s	284.5
	C-C sp^3	C 1s	285.3
	C-Cr	C 1s	284.0
	Cr^0	C-Cr	576.2
	Cr_2O_3	Cr^{3+} $2p_{3/2}$	577.2
		Cr^{3+} $2p_{1/2}$	586.7

	CrO_3	Cr^{6+} $2p_{3/2}$	579.0
		Cr^{6+} $2p_{1/2}$	588.7
	Metal-O	O 1s	530.2
	OH_{ads}	O 1s	531. 5
	C=O	O 1s	533.2

8.3 Catalytic activity of the Pt-$CoTiO_3$/rGO-Cr_{tric}, Pt-$CoTiO_3$/rGO_2Cr and Pt-$CoTiO_3$/rGO-Cr_{bz} catalysts for the ORR.

8.3.1 ORR kinetics.

The CVs of the catalysts in Figure 8.15 show the characteristic regions of Pt-based catalysts (see Chapters V and VI), more clearly distinguished at Pt-$CoTiO_3$/rGO_2Cr. The Q_H values have been determined by integrating the H_{des} region from de CVs, after subtracting the double layer contribution. The Pt real surface area of the catalyst (A_{Pt}) has been obtained with the aid of equation 5.9. Moreover, the ECSA value of the catalysts has been determined with equation 5.5. The results are shown in Table 6.4.

Pt-$CoTiO_3$/rGO_2Cr has the highest values of these three parameters. Its ECSA (36.32 m^2 g^{-1}) is even higher than that of Pt-$CoTiO_3$/rGO (12.07 m^2 g^{-1}, shown also in Table 8.4). These results show that the functionalization of rGO with 0.04 mmol of Cr-hexac (i.e., $Cr(CO)_6$) influences to a lesser extent the electrochemical behavior of Pt nanoparticles at Pt-$CoTiO_3$/rGO_2Cr, by better defining the different Pt-regions than Pt-$CoTiO_3$/rGO-Cr_{tric} (rGO functionalized with 0.22 mmol of Cr-hexac). Meanwhile, the use of Cr-bz (i.e., η^6-C_6H_6)$Cr(CO)_3$) as functionalizing agent seems to inhibit the Pt-regions to a larger extent at Pt-$CoTiO_3$/rGO-Cr_{bz}.

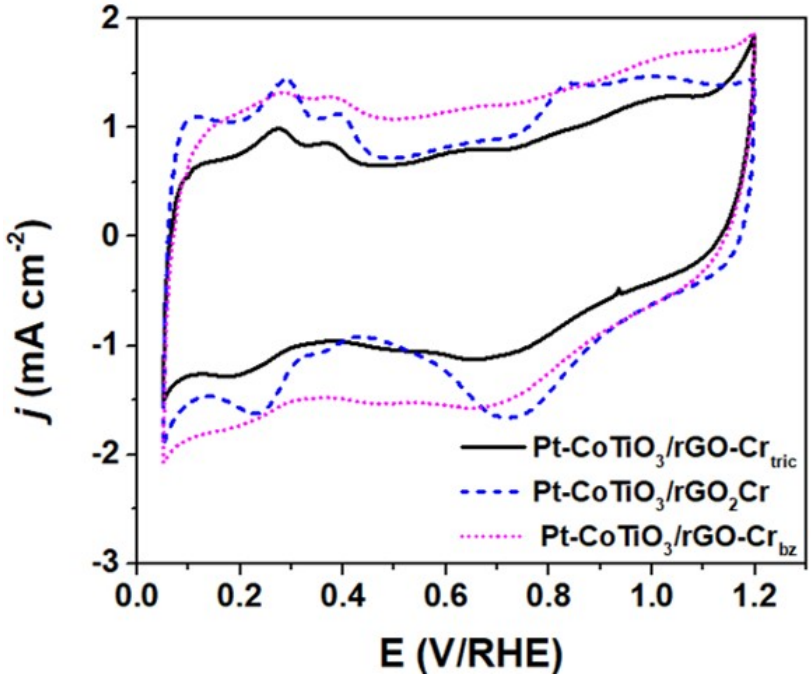

Figure 8.15 CVs of Pt-$CoTiO_3$/rGO-Cr_{tric}, Pt-$CoTiO_3$/rGO$_2$Cr and Pt-$CoTiO_3$/rGO-Cr_{bz} catalysts. Electrolyte: N_2-satured 0.5 M KOH. Scan rate of 20 mV s^{-1}.

Table 8.4 Electrochemical parameters of the Pt-$CoTiO_3$/rGO-Cr_{tric}, Pt-$CoTiO_3$/rGO$_2$Cr and Pt-$CoTiO_3$/rGO-Cr_{bz} catalysts.

Catalyst	Q_H (μC)	A_{Pt} (cm^2)	ECSA (m^2 g^{-1})	E_{onset} (V/RHE)	$j_{0.9\ V/RHE}$ (mA cm^{-2})
Pt-$CoTiO_3$/rGO	533	2.54	12.07	0.99	-0.94
Pt-$CoTiO_3$/rGO-Cr_{tric}	522	2.48	13.79	1.01	-0.59
Pt-$CoTiO_3$/rGO$_2$Cr	1450	6.90	36.32	1.03	-0.91
Pt-$CoTiO_3$/rGO-Cr_{bz}	411	1.96	10.31	1.02	-0.91

Figure 8.16 shows the polarization curves of the ORR at the Pt-$CoTiO_3$/rGO-Cr_{tric}, Pt-$CoTiO_3$/rGO$_2$Cr and Pt-$CoTiO_3$/rGO-Cr_{bz} catalysts, where the kinetic, mixed and diffusion-limiting regions are observed. The dependence of the oxygen reduction current on the rotation rate indicates that the process is in fact under mixed kinetic-diffusion control.

The onset potential (E_{onset}) and current density *j* at 0.9 V/RHE of each catalyst are summarized in Table 8.4. Pt-$CoTiO_3$/rGO-Cr_{tric}, Pt-$CoTiO_3$/rGO$_2$Cr and Pt-$CoTiO_3$/rGO-Cr_{bz} catalyst exhibit E_{onset} values of 1.01, 1.03 and 1.02 V/RHE, more positive than Pt-$CoTiO_3$/rGO (0.99 V/RHE). On the other hand, Pt-$CoTiO_3$/rGO$_2$Cr and Pt-$CoTiO_3$/rGO-Cr_{bz} generate $j_{0.9\ V/RHE}$= -0.91 mA cm^{-2}, slightly lower than the -0.94 mA cm^{-2} at Pt-$CoTiO_3$/rGO. This value is clearly lower at Pt-$CoTiO_3$/rGO-Cr_{tric} (Table 8.4).

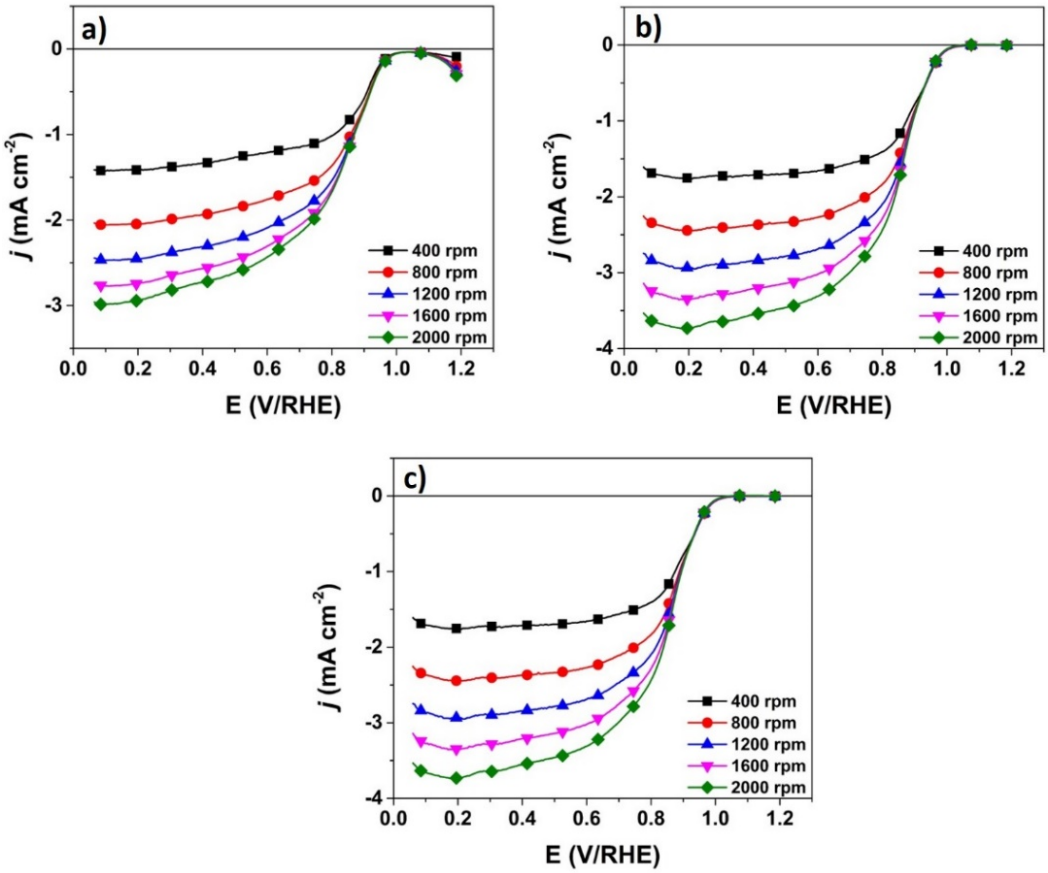

Figure 8.16 Polarization curves for the ORR on: a) Pt-$CoTiO_3$/rGO-Cr_{tric}, b) Pt-$CoTiO_3$/rGO$_2$Cr and c) Pt-$CoTiO_3$/rGO-Cr_{bz} catalysts in O_2-satured 0.5 M KOH electrolyte. Scan rate: 5 mV s^{-1}.

Koutecky-Levich plots of the Pt-$CoTiO_3$/rGO-Cr_{tric}, Pt-$CoTiO_3$/rGO_2Cr and Pt-$CoTiO_3$/rGO-Cr_{bz} catalysts obtained from mixed diffusion-kinetic limited region are shown in Figure 8.17. Straight and parallel lines are observed, suggesting that the electron transfer mechanism is constant at the different electrode potentials. The number of electrons involved in the overall ORR on Pt-$CoTiO_3$/rGO-Cr_{tric}, catalyst was calculated to be 2.3 and 2.7 for both Pt-$CoTiO_3$/rGO_2Cr and Pt-$CoTiO_3$/rGO-Cr_{bz}.

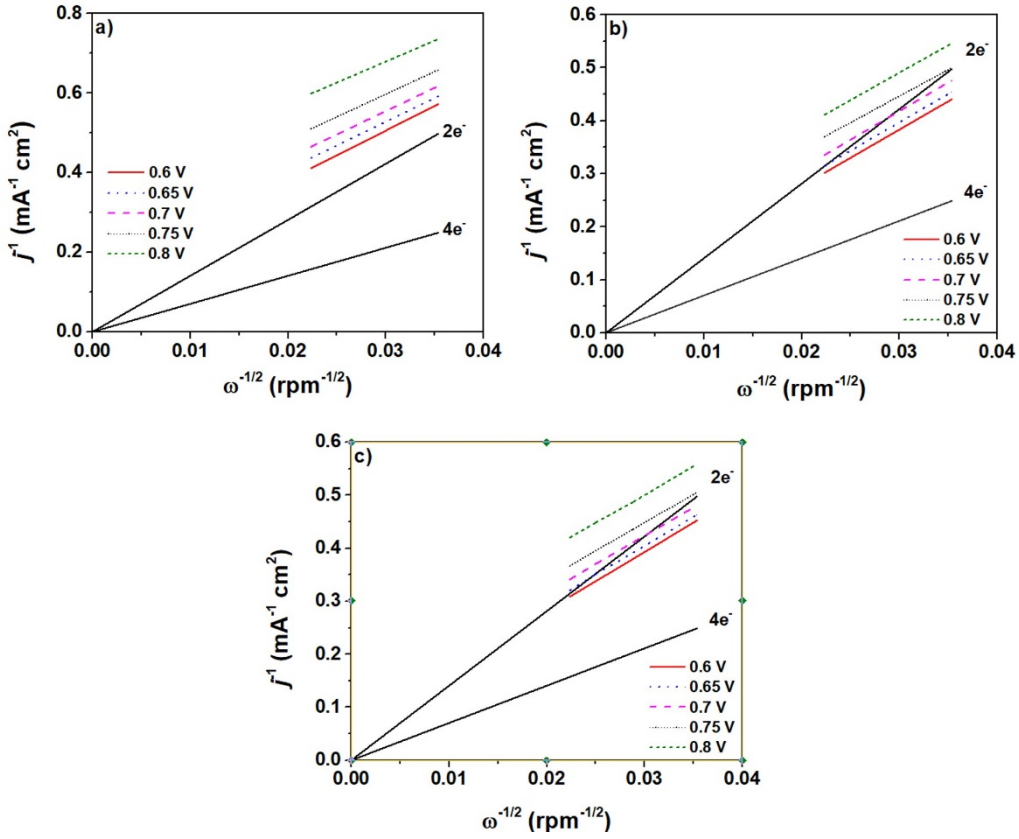

Figure 8.17 Koutecky-Levich plots of the ORR at different potentials of: a) Pt-$CoTiO_3$/rGO-Cr_{tric}, b) Pt-$CoTiO_3$/rGO_2Cr and c) Pt-$CoTiO_3$/rGO-Cr_{bz}.

For a better understanding of the catalytic activity of the catalysts for the ORR. Tafel plots have been obtained following the procedure described in Chapter V (see equation 5.8 and discussion therein) by calculating the mass and specific

current densities (i_m and i_s, respectively). The results are shown in Figure 8.18 as (a) mass and (b) specific activity.

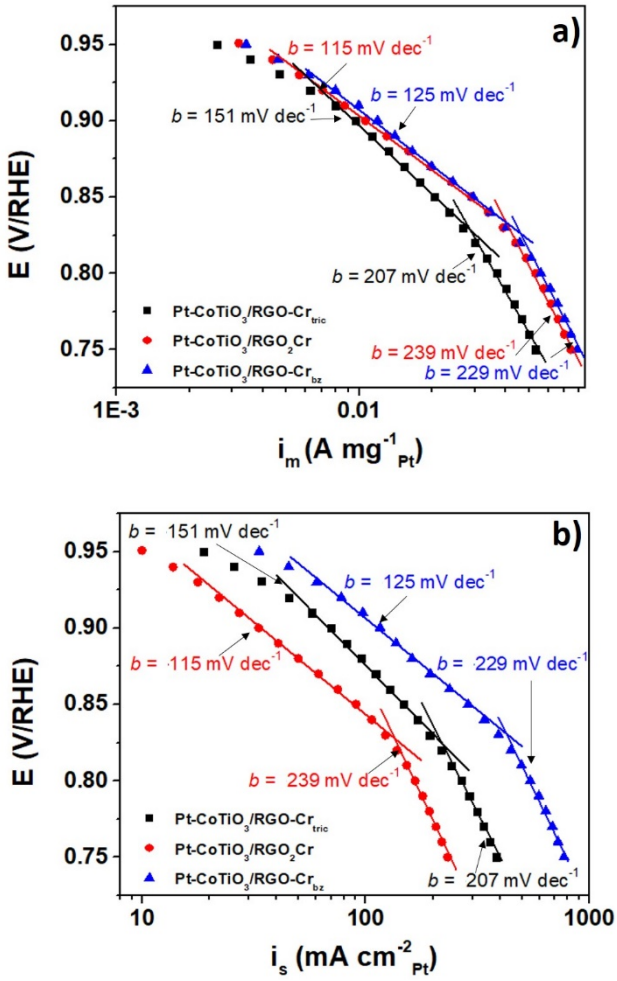

Figure 8.18 (a) Mass and (b) specific activity plots of the ORR on Pt-CoTiO$_3$/rGO-Cr$_{tric}$, Pt-CoTiO$_3$/rGO$_2$Cr and Pt-CoTiO$_3$/rGO-Cr$_{bz}$ catalysts. Electrolyte: 0.5 M KOH saturated with O_2. ω = 2000rpm.

The plots show two linear regions with well-defined Tafel slopes (*b*). Table 6.5 shows the Tafel slopes at low ang high overpotentials (*b* at lop and hop, respectively). *b* at lop of 151, 115 and 125 mV dec^{-1} have been calculated for Pt-CoTiO$_3$/rGO-Cr$_{tric}$, Pt-CoTiO$_3$/rGO$_2$Cr and Pt-CoTiO$_3$/rGO-Cr$_{bz}$,

respectively. Meanwhile, the catalysts have a *b* at hop values of 207, 239 and 229 mV dec^{-1}. These values are significantly higher than those of Pt-$CoTiO_3$/rGO and represent a significant deviation from the theoretical Tafel slopes of 60 and 120 mV dec^{-1} observed during the ORR at Pt catalysts in alkaline media.[45] As discussed earlier (Chapter VII) several factors influence in the variation in the Tafel slopes values, such as, the change in the rate determining step of the ORR (O_2 adsorption mechanism) and the participation of the carbon support on the reaction. Moreover, the presence of Cr may have also played a role on the kinetics of the ORR and therefore on the slopes.

Table 8.5 show the values of catalytic activity derived from the Figure 8.18. The mass and specific activities at 0.9 V/RHE of Pt-$CoTiO_3$/rGO-Cr_{bz} are the highest (0.001 A mg^{-1}_{Pt} and 116.13 μA cm^{-2}_{Pt}, respectively). As a comparison, these values are 3.6 and 4.1 higher that the performance shown by Pt-$CoTiO_3$/rGO. Pt-$CoTiO_3$/rGO-Cr_{tric} and Pt-$CoTiO_3$/rGO$_2$Cr also show enhanced ORR parameters. Therefore, the functionalization of rGO with Cr organometallic compounds enhances the catalytic activity for the ORR, particularly with Cr-bz. Similar improvement has been reported elsewhere with different functionalization approaches of carbon nanostructures.[46,47]

Table 8.5 Mass and specific activities data for ORR at Pt-$CoTiO_3$/rGO-Cr_{tric}, Pt-$CoTiO_3$/rGO$_2$Cr and Pt-$CoTiO_3$/rGO-Cr_{bz} catalysts.

Catalyst	*b* at lop (mV dec^{-1})	*b* at hop (mV dec^{-1})	Mass activity at 0.9 V/RHE (A mg^{-1}_{Pt})	Specific activity at 0.9 V/RHE / (μA cm^{-2}_{Pt})
Pt-$CoTiO_3$/rGO	70	176	0.003	28.2
Pt-$CoTiO_3$/rGO-Cr_{tric}	151	207	0.009	69.99
Pt-$CoTiO_3$/rGO$_2$Cr	115	239	0.010	33.23
Pt-$CoTiO_3$/rGO-Cr_{bz}	125	229	0.011	116.13

8.3.2 Tolerance tests.

The catalytic activity of the catalysts for the ORR in 0.5 M KOH with 0.1 M CH_3OH or C_2H_5OH has been also investigated. The polarization curves in the absence and presence of the alcohols at Pt-$CoTiO_3$/rGO-Cr_{tric} are shown in Figure 8.19a. The presence of both methanol and ethanol provokes peak current densities (*j*) of 0.85 and -0.54 mA cm^{-2}, respectively (Table 8.6). It also causes a shift in E_{onset} towards more negative potentials by 90 and 70 mV, respectively. It is well known that this behavior is due to the competition between the ORR and fuel oxidation reactions on the cathode surface, which leads to a mixed potential.

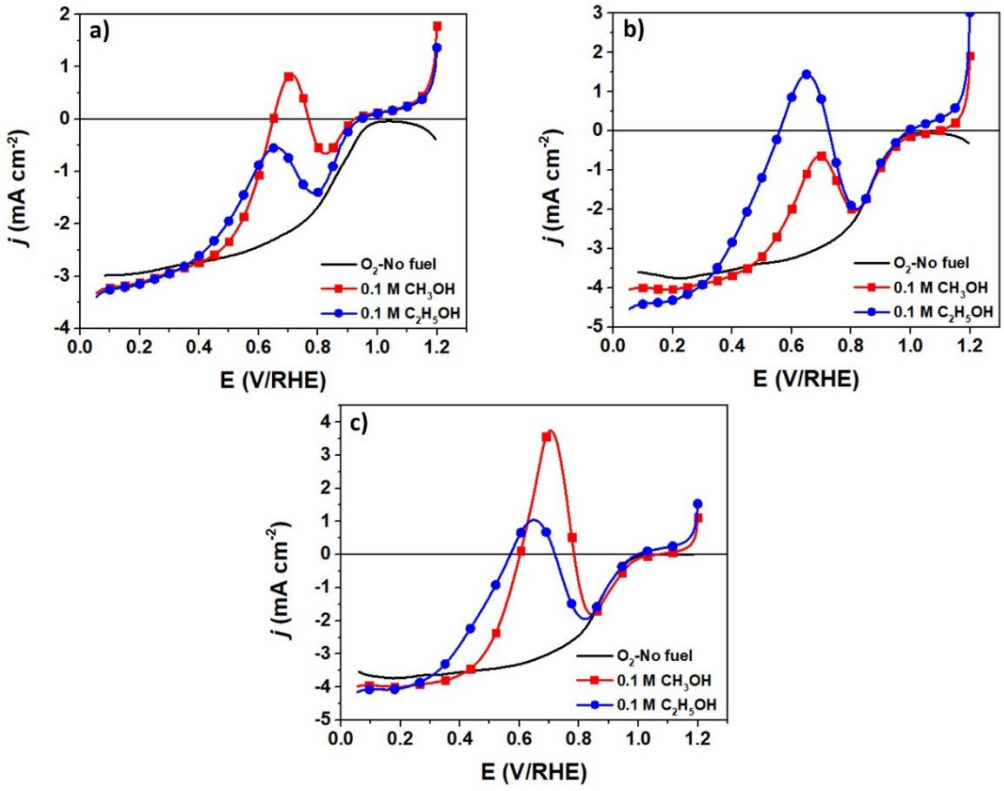

Figure 8.19 Polarization curves of the ORR at: a) Pt-$CoTiO_3$/rGO-Cr_{tric}, b) Pt-$CoTiO_3$/rGO$_2$Cr and c) Pt-$CoTiO_3$/rGO-Cr_{bz} in the absence and presence of 0.1 M CH_3OH or C_2H_5OH. Electrolyte: 0.5 M KOH. Scan rate: 5 mV s-1. ω = 2000 rpm.

Figure 8.19b shows the polarization curves at the Pt-$CoTiO_3$/rGO_2Cr catalyst at which *j* peaks associated to the methanol and ethanol oxidation are generated, while E_{onset} increases with CH_3OH (Table 8.6). On the other hand, the polarization curves at Pt-$CoTiO_3$/rGO-Cr_{bz} (Figure 8.19c) show also its low tolerance to methanol and ethanol by generating positive *j* peaks. Table 8.6 summarizes the *j* values generated by the oxidation of the fuels, as well as the E_{onset} values of the reaction in absence and presence of methanol and ethanol at the catalysts.

Table 8.6 Fuel oxidation current densities and E_{onset} of the ORR at Pt-$CoTiO_3$/rGO-Cr_{tric}, Pt-$CoTiO_3$/rGO_2Cr and Pt-$CoTiO_3$/rGO-Cr_{bz} in the presence of 0.1 M CH_3OH and C_2H_5OH.

	Fuel oxidation *j* (mA cm^{-2})		***E*$_{onset}$ (V/RHE)**		
Catalyst	**CH_3OH**	**C_2H_5OH**	**O_2-No fuel**	**CH_3OH**	**C_2H_5OH**
Pt-$CoTiO_3$/rGO-Cr_{tric}	0.85	-0.54	1.01	0.92	0.94
Pt-$CoTiO_3$/rGO_2Cr	3.75	1.04	1.03	1.06	0.99
Pt-$CoTiO_3$/rGO-Cr_{bz}	-0.62	1.44	1.02	1.09	0.99

Overall, the tolerance shown by the catalysts in Figure 8.19 is lower than that of Pt-$CoTiO_3$/rGO with 0.1 M CH_3OH (Figure 7.14c). This effect may be correlated to the Cr species which promoted the oxidation of the organic molecules.

8.4 References

[1] G. Bistoni, S. Rampino, N. Scafuri, G. Ciancaleoni, D. Zuccaccia, L. Belpassi, and F. Tarantelli. How π back-donation quantitatively controls the CO stretching response in classical and nonclassical metal carbonyl complexes. Chemical Science. 7 (2016) 1174.

[2] P. J. Dyson, and J. S. Mclndoe. Transition Metal Carbonyl Cluster Chemistry. Advanced Chemistry Texts. Gordon and Breach Science Publishers. The Netherlands, 2000.

[3] R. P. A. Sneed. Organochromium Compounds. Academic Press. New York, 1975.

[4] C. Lee, E. A. Pederick, and N. E. Leadbeater. Preparation of arene chromium Tricarbonyl complexes using continuous-flow processing: $(\eta^6\text{-}C_6H_5CH_3)Cr(CO)_3$ as an example. Journal of Flow Chemistry. 2 (2012) 115.

[5] L. M. Haines, and M. H. B. Stiddard. Vibrational spectra of transition metal carbonyl complexes. Advances in Inorganic Chemistry and Radiochemistry. 12 (1970) 53.

[6] R. J. H. Clark, and B. Crociani. Solvents effects on the infrared spectra of chromium, molybdenum and tungsten hexacarbonyls. Inorganica Chimica Acta. 1 (1967) 12.

[7] G. Hunter, C. H. Rochester, A. G. Wilkinson and J. Paton. FTIR study of chromium carbonyl complexes on silica-alumina: Active ethane polymerization catalysts. Journal of the Chemical Society, Faraday Transactions. 93 (1997) 1205.

[8] L. J. Bellamy. The Infra-red Spectra of Complex Molecules. Chapman and Hall. London, 1954.

[9] G. S. Girolami, T. B. Rauchfuss, and R. J. Anegelici. Synthesis and Technique in Inorganic Chemistry. University Science Books. United States of America, 1999.

[10] M. Wrighton. Photochemistry of metal carbonyls. Chemical Reviews. 74 (1974) 401.

[11] E. W. Abel, and F. G. A. Stone. The chemistry of transition-metal carbonyls: synthesis and reactivity. Quarterly Reviews, Chemical Society. 24 (1970) 498.

[12] S. Sarkar, S. Niyogi, E. Bekyarova, R. C. Haddon. Organometallic chemistry of extended periodic π-electron systems: hexahapto-chromium complexes of graphene and single-walled carbon nanotubes. Chemical Science. 2 (2011) 1326.

[13] W. M. Lamanna. Metal vapor synthesis of a novel triple-decker sandwich complex: $(\eta^6\text{-mesitylene})_2(\mu\text{-}\eta^6\text{-}\eta^6\text{-mesitylene})Cr_2$. Journal of the American Society. 108 (1986) 2096.

[14] J. Dai, Y. Zhao, X. Wu, X. C. Zeng, and J. Yang. Organometallic hexahapto-functionalized graphene: band gap engineering with minute distortion to the planar structure. The Journal of Physical Chemistry C. 117 (2013) 22156.

[15] L. Kashinath, K. Namratha, S. Srikantaswamy, A. Vinu, and K. Byrappa. Microwave treated sol-gel synthesis and characterization of hybrid ZnS-RGO composites for efficient photodegradation of dyes. New Journal of Chemistry. 41 (2017) 1723.

[16] M. Zhong, Y. Huang, Y. Zhao, X. Sun, C. Qu, D. Luo, and J. Zheng. Facile preparation, high microwave absorption and microwave absorbing mechanism of RGO-Fe_3O_4 composites. RSC Advances. 3 (2013) 23638.

[17] X. Huang, N. Hu, R. Gao, Y. Yu, Y. Wang, Z. Yang, E. Kong, H. Wei, and Y. Zhang. Reduced graphene oxide-polyaniline hybrid: Preparation, characterization and its applications for ammonia gas sensing. Journal of Materials Chemistry. 22 (2012) 22488.

[18] B. D. Ossonon, and D. Bèlanger. Synthesis and characterization of sulfophenyl-functionalized reduced graphene oxide sheets. RSC Advances. 7 (2017) 27224

[19] T. Maiyalagan, X. Dong, P. Chen, and X. Wang. Electrodeposited Pt on three-dimensional interconnected graphene as a free-standing electrode for fuel cell application. Journal of Materials Chemistry. 22 (2012) 5286.

[20] I. Tallo, T. Thomberg, K. Kontturi, A. Jänes, and E. Lust. Nanostructured carbide-derived carbon synthesized by chlorination of tungsten carbide. Carbon. 49 (2011) 4427.

[21] Z. Xing, Z. Ju, Y. Zhao, J. Wan, Y. Zhu, Y. Qiang, and Y. Qian. One-pot hydrothermal synthesis of nitrogen-doped graphene as high-performance anode materials for lithium ion batteries. Scientific Reports. 6 (2016) 26146.

[22] G. Wang, X. Shen, B. Wang, J. Yao, and J. Park. Synthesis and characterization of hydrophilic and organophilic graphene nanosheets. Carbon. 47 (2009) 1359.

[23] P. G. Ren, D. X. Yan, X. Ji, T. Chen, and Z. M. Li. Temperature dependence of graphene oxide reduced by hydrazine hydrate. Nanotechnology. 22 (2011) 055705.

[24] S. Stankovich, D. A. Dikin, R. D. Piner, K. A. Kohlhaas, A. Kleinhammes, Y. Jia, Y. Wu, S. T. Nguyen, and R. S. Ruoff. Synthesis of graphene.based nanosheets via chemical reduction of exfoliated graphite oxide. Carbon. 45 (2007) 1558.

[25] A. Hernández-Ramírez, M. E. Sánchez-Castro, I. Alonso-Lemus, A. Kalasapuyaril, K. Palamisamy, M. Ramasamy, and F. J. Rodríguez-Varela. Evaluation of the nickel titanate-modified Pt nanostructured catalyst for the ORR in alkaline media. Journal of the Electrochemical Society. 163 (2014) F16.

[26] A. A. Siller-Ceniceros, M. E. Sánchez-Castro, D. Morales-Acosta, J. R. Torres-Lubián, E. Martínez G., and F. J. Rodríguez-Varela. Innovative functionalization of Vulcan XC-72 with Ru organometallic complex: Significant enhancement in catalytic activity of Pt/C electrocatalyst for the methanol oxidation reaction (MOR). Applied Catalysis B: Environmental. 209 (2017) 455.

[27] K. A. Daube, M. T. Paffett, S. Gottesfeld, and C. T. Campbell. Combined electrochemical/surface science investigations of Pt/Cr alloys electrodes. Journal of Vacuum Science and Technology A. 4 (1986) 1617.

[28] S. J. Seo, H. I. Jo, H. T. Kim, and S. H. Moon. Properties of Pt/C catalyst modified by chemical vapor deposition of Cr as a cathode of phosphoric acid fuel cell. Electrochimica Acta. 52 (2006) 1676.

[29] B. N. Grgur, M. N. Markovic, and P. N. Ross. Electrooxidation of H_2, CO, and H_2/CO mixtures on a well-characterized $Pt_{70}Mo_{30}$ bulk alloy electrode. The Journal of Physical Chemistry B. 102 (1998) 2494.

[30] J. B. Xu, T. S. Zhao, W. W. Yang, and S. Y. Shen. Effect of surface composition of Pt-Au alloy cathode catalyst on the performance of direct methanol fuel cells. International Journal of Hydrogen Energy. 35 (2010) 8699.

[31] Z. Yang, C. Li, W. Chen, R. Liu, H. Wei, Y. Ma, S. Meng, S. Hu, and Y. Wei. Preparation and catalytic property of carbon nanotubes supported Pt and Ru nanoparticles for hydrogenation of aldehyde and substituted acetophenone in water. Indian Journal of Chemistry. 56A (2017) 1321.

[32] J. R. Croy, S. Mosfata, L. Hickman, H. Heinrich, and B. R. Cuenya. Bimetallic Pt-Metal catalysts for the decomposition of methanol: Effect of secondary metal on the oxidation state, activity, and selectivity of Pt. Applied Catalysis A: General. 350 (2008) 207.

[33] S. Jiang, Y. Ma, H. Tao, G. Jiang, X. Wang, Y. Fan, J. Zhu, and Z. Hu. Highly Dispersed Pt-Ni Nanoparticles on Nitrogen-Doped Carbon Nanotubes for Application in Direct Methanol Fuel Cells. Journal of Nanoscience and Nanotechnology. 10 (2010) 3895.

[34] A. Eguizabal, L. Uson, V. Sebastian, J. L Hueso, and M. P Pina. Efficient and facile tuning of Vulcan XC-72 with ultra-small Pt nanoparticles for electrocatalytic applications. RSC Advances. 5 (2015) 90691.

[35] M. Folkenant, K. Nygren, P. Malinovskis, J. PAlisaitis, P. O. A. Persson, E. Lewin, and U. Jansson. Structure and properties of Cr–C/Ag films deposited by magnetron sputtering. Surface & Coatings Technology. 281 (2015) 184.

[36] Q. Song, Q. Xu, X. Shang, Z. Ning, Y. Qi, and K. Yu. Electrochemical preparation of a carbon/Cr-O-C bilayer film on stainless steel in molten LiCl-KCl-K_2CO_3. Journal of Electrochemical Society. 162 (2015) D82.

[37] I. Kalinina, E. Bekyarova, S. Sarkar, F. Wang, M. E. Itkis, X. Tian, S. Niyogi, N. Jha, and R. C. Haddon. Hexahapto-metal complexes of single-walled carbon nanotubes. Macromolecular Chemistry and Physics. 213 (2012) 1001.

[38] S. Pignataro, A. Foffani, and G. Distefano. ESCA study of some chromium complexes: ionization energies and multi-peak structure of the spectra. Chemical Physics Letters. 20 (1973) 350.

[39] T. Hou, L. Kong, X. Guo, Y. Wu, F. Wang, Y. Wen, and H. Yang. Magnetic ferrous-doped graphene for improving Cr(VI) removal. Materials Research Express. 3 (2016) 045006.

[40] S. C. Wang, H. T. Lin, P. K. Nayak, S. Y. Chang, and J. L. Huang. Carbothermal reduction process for synthesis of nanosized chromium carbide via metal-organic vapor deposition. Thin Solid Films. 518 (2010) 7360.

[41] H. Luo, H. Su, G. Ying, C. Dong, and X. Li. Effect of cold deformation on the electrochemical behaviour of 304L stainless steel in contaminated sulfuric acid environment. Applied Surface Science. 42 (2017) 628.

[42] D. Veys, P. Weisbecker, B. Domenichini, S. Weber, V. Fournée, and J. M. Dubois. Chemical surface ageing in ambient conditions of an Al-Fe-Cr approximant phase. Journal of Physics: Condensed Matter. 19 (2007) 376207.

[43] F. Liu, J. Shen, D. Xu, W. Zhou, S. Zhang, and L. Wan. Oxygen vacancies enhanced HCHO oxidation on a novel $NaInO_2$ supported Pt catalyst at room temperature. Chemical Engineering Journal. 334 (2018) 2283.

[44] K. Y. Andrew, D. Y. Lin, Y. C. Lu, J. T. Lin, and Y. F. Lin. Electrospun nanofiber of cobalt titanate perovskite as an enhanced heterogeneous catalyst for activating peroxymonosulfate in water. Chemical Engineering Science. 168 (2017) 372.

[45] F. H. B. Lima, J. R. C. Salgado, E. R. Gonzalez, and E. A. Ticianelli. Electrocatalytic properties of PtCo/C and PtNi/C alloys for the oxygen reduction reaction in alkaline solution. Journal of the Electrochemical Society. 154 (2007) A369.

[46] D. Park, M. S. Ahmed, and S. Jeon. Covalent functionalization of graphene with 1,5-diaminonaphthalene and ultrasmall palladium nanoparticles for electrocatalytic oxygen reduction. International Journal of Hydrogen Energy. 42 (2017) 2061.

[47] Z. Y. Zhou, X. Kang, Y. Song, S. Chen. Enhancement of the electrocatlytic activity of Pt nanoparticles in oxygen reduction by chlorophenyl functionalization. Chemical Communications. 48 (2012) 3391.

Chapter IX

Conclusions

9.1 Enhanced electrocatalytic performance for the Oxygen Reduction Reaction on Pt-$MTiO_3$/C (M = Ni, Co) catalysts.

- The $NiTiO_3$ and $CoTiO_3$ have a synergetic effect on Pt, increasing the mass and specific activity of Pt-$NiTiO_3$/C and Pt-$CoTiO_3$/C at some potential range, compared to Pt/C.
- The ORR at Pt-$NiTiO_3$/C and Pt-$CoTiO_3$/C proceeds via a $4e^-$ mechanism.
- The presence of $CoTiO_3$ enhances the tolerance of Pt to 0.1 M CH_3OH and C_2H_5OH at Pt-$CoTiO_3$/C.

9.2 Electrocatalytic activity of the rGO-supported Pt-$MTiO_3$ (M = Ni, Co) catalysts for the Oxygen Reduction Reaction in alkaline media.

- From XPS analysis: Pt^0 species are predominantly formed over Pt^{2+} and Pt^{4+}.
- The ORR at Pt-$NiTiO_3$/rGO and Pt-$CoTiO_3$/rGO proceeds via a $4e^-$ mechanism.
- Due to a synergetic effect between $CoTiO_3$ and Pt, the specific activity of Pt-$CoTiO_3$/rGO is higher than those of Pt/rGO and Pt-$NiTiO_3$/rGO.
- Due to a geometric effect, the tolerance of Pt-$CoTiO_3$/RGO to 0.1 M CH_3OH is significantly higher than those of Pt/rGO and Pt-$NiTiO_3$/rGO.

9.3 rGO functionalized with chromium organometallic compounds as a novel support for highly active Pt-$CoTiO_3$ catalyst for the Oxygen Reduction Reaction.

- The proposed methodology successfully forms rGO structures functionalized with the Cr-hexac and Cr-bz organometallic compounds.
- Functionalization with different stoichiometric amounts of Cr-hexac results in mono and bis-hexahapto complexes (rGO-Cr_{tric} and rGO_2Cr) due to the displacement of the carbonyl groups.
- Functionalization with Cr-bz eliminates the three carbonyl groups, while the arene unit is retained forming the rGO-Cr_{bz} complex.
- The use of Cr-hexac as functionalizing agent increases the sp^2 nanodomains of rGO-Cr_{tric} and rGO_2Cr, compared to rGO. In contrast, Cr-bz shows no significant effect at rGO-Cr_{bz} related to the structural order of rGO.
- Cr_2O_3 and CrO_3 species are formed after functionalization with both organometallic compounds. The presence of Cr leads to the formation of Pt-Cr alloyed phases.
- The use of the Cr-bz organometallic compound enhances the mass and specific activities of Pt-$CoTiO_3$/rGO-Cr_{bz}, compared to Pt-$CoTiO_3$/rGO-Cr_{tric}, Pt-$CoTiO_3$/rGO_2Cr and Pt-$CoTiO_3$/rGO.
- The presence of Cr species reduces the tolerance of the catalysts related to Pt-$CoTiO_3$/rGO.